Weak Gravitational Lensing in the Cosmic Microwave Background: Reconstructing the Lensing Convergence

Jethro Venn Ridl

University of KwaZulu-Natal

WEAK GRAVITATIONAL LENSING IN THE COSMIC MICROWAVE BACKGROUND: RECONSTRUCTING THE LENSING CONVERGENCE

Jethro Venn Ridl

Submitted in fulfillment of the academic requirements for the degree of Master of Science in the School of Mathematical Sciences, University of KwaZulu-Natal, Westville.

As the candidate's supervisor I have approved this dissertation for submission.

Signed: Name: Date:

ABSTRACT

Many of the most significant constraints on the standard model of Cosmology describing the origins, contents and evolution of the Universe arise from the Cosmic Microwave Background (CMB). As we enter an era of precision cosmology, with more sensitive and higher angular resolution ground, balloon and space-based experiments, it is becoming increasingly important to understand the small-scale secondary anisotropies of the CMB. One of the most important of these secondary anisotropies comes from weak gravitational lensing, whereby free-streaming CMB photons are deflected by the gravitational potentials in the large-scale structure of the Universe. This has several important effects including modifications to the CMB power spectrum, the introduction of non-Gaussianities and the generation of B-mode polarization. In principle it is possible to reconstruct the the projection of the gravitational potential on the celestial sphere directly from observations of the CMB temperature anisotropies by examining the distinctive non-Gaussian signature the gravitational lensing imparts on to the CMB. This reconstructed map can be used to constrain the amplitude of the mass fluctuations in the early Universe and contains significant information regarding the dark matter distribution throughout the Universe.

After a review of the standard Big Bang cosmological model the phenomenon of gravitational lensing is introduced. Equations for the deflection angle and lensing convergence are derived, as well as their power spectra, and the effect that gravitational lensing has on the CMB is discussed. In the main part of the thesis we study two methods for reconstructing the lensing convergence, the standard harmonic space quadratic estimator and a second estimator which is defined in real space. Each of the estimators is derived and implemented to recover reconstructed lensing convergence maps. The various biases that are inherent in the estimators is discussed, including details of how these biases can be removed. The performance of each of the estimators in reconstructing the lensing convergence is evaluated and contrasted.

The final part of this thesis involves an analysis of a non-linear bias which affects both the har-

monic space and real space estimators, resulting from a break down of the linear approximation, which arises if the lensing field has a sufficiently large magnitude. The effect of the non-linear bias on the reconstructed lensing field is evaluated, and comparison of these results with the reconstructed lensing amplitude from the Atacama Cosmology Telescope (ACT) and the South Pole Telescope (SPT) lensing measurement provides an estimate for the level of importance of the non-linear bias.

PREFACE

The study described in this thesis was carried out in the School of Mathematical Sciences, University of KwaZulu-Natal during the period January 2010 to October 2012. This dissertation was completed under the supervision of Prof. K Moodley.

This study represents original work by the author and has not been submitted in any form for any degree or diploma to another tertiary institution. Where use was made of the work of others it has been duly acknowledged in the text.

Signed: Name: Date:

DECLARATION 1 - PLAGIARISM

I, Jethro Ridl, declare that

1. The research reported in this thesis, except where otherwise indicated, is my original research.
2. This thesis has not been submitted for any degree or examination at any other university.
3. This thesis does not contain other persons' data, pictures, graphs or other information, unless specifically acknowledged as being sourced from other persons.
4. This thesis does not contain other persons' writing, unless specifically acknowledged as being sourced from other researchers. Where other written sources have been quoted, then:
    - Their words have been re-written but the general information attributed to them has been referenced.
    - Where their exact words have been used, then their writing has been placed in italics and inside quotation marks, and referenced.
5. This thesis does not contain text, graphics or tables copied and pasted from the Internet, unless specifically acknowledged, and the source being detailed in the thesis and in the References sections.

Signed: Name: Date:

For my grandfather, George Venn Quicke, a role model and inspiration who was one of the greatest influences on the man that I have become.

I love deadlines. I love the whooshing noise they make as they go by.

- Douglas Adams

ACKNOWLEDGMENTS

I am greatly indebted to my supervisor for this project, Prof Kavilan Moodley, without whom this work would never have been possible. I am immensely thankful for having had the privilege of working with Kavi and he has been a constant source of wisdom, motivation and inspiration. I am also grateful for the continued financial support he has provided through the National Research Foundation (NRF) Multi-wavelength Astronomy grant and for supporting visits to the USA, India and numerous conferences around South Africa.

Additional funding for this research came from a National Research Foundation Scarce-Skills scholarship.

Other people who have contributed important ideas to this work are Prof Martin Bucher at the University of Paris and Dr Carla Carvalho, who continued to help me in the early stages of the project even after the conclusion of her postdoc here in South Africa.

I also wish to thank my home institution, the University of KwaZulu-Natal and particularly the Astrophysics and Cosmology Research Unit, for providing me with a space to do my research. I am also thankful for the opportunities that I have had to spend time overseas and acknowledge the support of Princeton University in the USA and the Inter-University Centre for Astronomy and Astrophysics (IUCAA) and the Jamia Mellia Islamia University in India.

The amount of administrative paperwork required over the last three years would have easily overwhelmed me were it not for the continued support of Ms Prashina Kallideen who not only provided administrative support but has also been a great friend.

Life might have become incredible dull at times were it not for the wonderful people who make up the ACRU and the School of Mathematics that has been my home since my undergraduate

studies. I am fortunate to have made great friends in during my Masters and am thankful for the friendship that has been so freely given. In particular I thank Dr Mathilde Jauzac and Darell Moodley who have helped to keep me sane down the final stretch and support and motivation they have provided has been crucial to the production of this thesis. I should also mention Prof Sunil Maharaj who so fantastically leads ACRU and my cousin Dr Caroline Zunckel who continues to inspire me.

Finally, I am eternally grateful to my family, most importantly my parents, who have made many sacrifices so that I could continue my studies without having to worry about very much other than my work and whose supply of motivation, support and inspiration has been incredible.

Contents

List of Figures

CHAPTER 1

Introduction

The prevailing model describing the origins and evolution of the Universe is the Big Bang Theory which predicts, according to current observations, that the Universe originated some 13.7 billion years ago [6] when an initial singularity underwent an extremely rapid expansion. This notion is supported by extrapolating back the observed expansion of the Universe through supernovae experiments and observations of the Cosmic Microwave Background (CMB). Initially, the Universe was extremely hot and dense and was rapidly expanding and cooling down. It is theorised that after a brief period of exponential expansion, known as cosmic inflation [7], the Universe consisted of a quark-gluon plasma alongside other elementary particles. Temperatures at this point were high enough that the particles were moving randomly at relativistic speeds and particle-antiparticle pairs were being constantly created and annihilated.The Universe continued to grow and fall in temperature and symmetry breaking phase transitions left the fundamental forces of physics and the parameters of elementary particles into their present form, known as the standard model of particle physics.

The energy levels involved in the previous discussion lie beyond current observational possibilities but when the Universe was a few picoseconds in age the particle energies dropped to a level that can be reached in modern particle accelerators. The quarks were able to combine to

form protons and neutrons. For reasons yet unknown, baryon and lepton number conservation was violated and slightly more matter particles than antimatter particles were created. The small excess in quarks over antiquarks led to a small excess in baryons over antibaryons and the energy was low enough that baryon-antibaryon creation ceased and all antibaryons were annihilated. A similar effect took place for leptons and antileptons after about a second and the energy density of the Universe was dominated by photons.

After a few minutes, protons and neutrons combined to form deuterium, helium and trace amounts of lithium nuclei in a process called Big Bang Nucleosynthesis. At this point the Universe was opaque, due to photons bring scattered by the ionized nuclei and electrons. When the Universe was approximately 350000 years old the electrons and nuclei combined in a process known as recombination to form the first atoms and the radiation was decoupled from the matter. The photons were then free to stream across the Universe and are observed today as the CMB. The Universe then went through a period known as the dark ages, since there were no sources of light apart from the cooling CMB. No longer suppressed by radiation, the primordial perturbations started to grow and matter began to cluster together under the effect of gravity to form gas clouds, stars, galaxies and galaxy clusters. After about 150 million years the radiation given off from the first stars then ionized the surrounding gas clouds in a process known as reionization that lasted until about a billion years after the Big Bang. At present however, the matter in the Universe is diluted enough that the scattering interactions are far less frequent than those prior to recombination and the Universe remains transparent. After billions of year of decelerating expansion, the Universe began to accelerate, first observed through observations of Type Ia supernovae [8, 9] the exact cause of which is unknown. The most widely excepted explanation for this is the existence of the mysterious dark energy.

The contents of the Universe is described by the concordance Λ cold dark matter (ΛCDM) cosmological model in which the Universe is dominated by a cosmological constant Λ and cold dark matter. This is generally regarded as the standard model of cosmology. ΛCDM has a strong observational foundation and assumes the correctness of Einstein's general relativity as the description of gravity. Ordinary matter such as baryons make up only a small fraction of the

Universe. The Universe is dominated by two exotic and mysterious components namely, dark matter and dark energy. The possibility of the existence of dark matter was first put forward by Zwicky when he noticed that there was a mass deficiency in galaxy clusters that would make them gravitationally unstable causing them to tear apart and thus some form of invisible matter was necessary to hold the clusters together [10]. Other studies such as gravitational lensing [11, 12, 13], galaxy rotation curves [14] and the distribution of intracluster gas [15] have lent great support to dark matter's existence. In the late 1990's two independent teams attempting to record the expansion history of the Universe from Type 1a supernovae observations reported that the Universe was in fact undergoing an accelerated expansion. The cosmological constant Λ is generally associated with dark energy and is the best model for this acceleration. In the current ΛCDM concordance model, the Universe comprises of 4% visible baryonic matter, 23% cold dark matter and 73% dark energy [6].

Some of the most important constraints on ΛCDM come from observations of the CMB, serendipitously discovered by Penzias and Wilson in 1964 [16], and its discovery was hailed as conclusive evidence of the Big Bang cosmological model. In order to understand the origins of the CMB one must understand that a hydrogen atom has a minimum ionization energy. An electron finding itself in the ground state requires 13.6 eV of energy in order for it to be released by the atom. As long as the Universe is hot enough, photons are easily energetic enough to keep the hydrogen fully ionised. When the Universe had a sufficiently high temperature, any electron attempting to bind to a proton would be almost immediately blasted away by a collision with a photon of light. The Universe at this time was thus a sea of free nuclei and electrons and the photons interacted strongly with the electrons via Thomson scattering. Due to the frequent nature of these interactions the mean free path of the photons was incredibly short and no light could permeate through space. As the Universe expanded and cooled, the photons lost energy and their power to ionize any atoms that formed diminished. Ultimately, all of the electrons made there way into the ground state of the atoms and the photons were no longer able to interact with the electrical neutral atoms. Over a short period of time, the Universe change from being opaque to being completely transparent. The photons were thus able to travel freely through space throughout the

remainder of the Universe's evolution.

The photons that we observe originate on the surface of a sphere centered on our location known as the surface of last scattering and has a radius of approximately 14 000 Mpc. When the photons started their journey, when the Universe was about 350 000 years old their temperature was about 3000 K and their frequencies much higher. As the Universe expanded they cool until they are detected on the Earth at a temperature just below 3 K and redshifted into the microwave region of the electromagnetic spectrum. The Universe was in thermal equilibrium at the time of recombination and thus the CMB should have the characteristics of a perfect blackbody spectrum. This was precisely confirmed by the Cosmic Background Explorer (COBE) the results of which were a perfect fit with a theoretical spectrum blackbody with a temperature of 2.7 K [17]. In addition to the detection of the blackbody spectrum of the CMB, COBE also made the first detection of faint anisotropies of 1 part in 100000 [18]. The fluctuations in the CMB temperature are the imprint of the primordial density perturbations in the early Universe and are believed to be responsible for seeding the structures that are observed in the Universe today. CMB anisotropies have the promise to revolutionize the field of cosmology and have begun to do so already with ground, balloon and space based experiments mapping the microwave sky with increasing sensitivity and resolution [19, 20, 21, 22].

The anisotropy of the CMB consists of two main parts: primary anisotropies, which originated at the surface of last scattering, and secondary anisotropies which are due to processes occurring between the last scattering surface and the observer such as interactions with hot gas or gravitational potentials. The structure of the primary anisotropy is dominated by acoustic oscillations on large scales and Silk damping on small angular scales. The acoustic oscillations arise from the interplay between the baryons, whose gravitational attraction cause the anisotropies to grow, and photons, which tend to erase the anisotropies. This gives the CMB its characteristic acoustic peaks. The acoustic peaks contain a great deal of information about the Universe in both their amplitude and angular scale. The location of the first peak determines the curvature of the Universe. The ratio of the odd peaks to even peaks determines the reduced baryon density and the third peak can be used to constrain dark matter density. Silk damping has the effect of suppress-

ing the anisotropies on very small angular scales [23] and this is seen in the exponential damping tail of the CMB power spectrum.

The most important secondary effect on large scales is the integrated Sachs-Wolfe effect (ISW) due to the propagation of photons through evolving gravitational potentials which causes the CMB photons to be either gravitationally redshifted or blue shifted [24]. Another important effect is that of reionization during which time the CMB photons are Thomson scattered by the free electrons. This causes a damping effect on the small scale anisotropy. The Sunyaev-Zel'dovich effect, whereby the CMB radiation is scattered by clouds of high energy electrons which transfer some of their energy to the photons [25, 26, 27] is an important contaminant of the signal on small scales and can be used to detect galaxy clusters. Weak gravitational lensing also has a number of important effects on the CMB and this is the focus of this work. The CMB temperature and polarization anisotropies are constantly being measured with increasing sensitivity and angular resolution. As we enter an era of precision cosmological measurements with high signal-to-noise observations on the smallest scales it is increasingly important to understand these secondary effects.

As the CMB photons free stream through space they are acted upon by the gravitational potentials of large-scale structures in the Universe. This has several important effects including modifications to the CMB power spectra, the introduction of non-Gaussianities and the generation of a B-mode polarization signal which is a source of confusion for the signal from primordial gravitational waves. The effect on the CMB temperature power spectrum is two-fold. Firstly, it causes a smoothing of the acoustic peaks and secondly creates additional power on small scales [28]. The lensing signal is thus very important on small angular scales and it dominates the CMB power spectrum. One can also make use of the lensing signal to help constrain cosmological parameters and the distribution of mass throughout the Universe up to very high redshifts. Much of the information about the lensing effect can be encapsulated in a single lensing potential that is related to the matter power spectrum. Lensing introduces a characteristic non-Gaussian signal in the CMB and this information contained in the induced non-Gaussianity can be used to study the distribution of the matter involved in the lensing.

The CMB is the most distant background image available. It thus provides a unique opportunity to map the dark matter distribution and contains information about structures on the largest scales in the high redshift Universe. Studies of this nature can complement weak lensing surveys of background galaxies, where the lensing effect due to large-scale structure produces an observable pattern of alignments in the background galaxies. This information can used to create mass distributions for the large-scale structure of the Universe, which can be compared to those obtained from CMB observations. The Gaussian structure of the CMB anisotropies provides an interesting challenge because unlike the images of background galaxies, there is no characteristic shape to the observed structures. The damping tail of the CMB anisotropies exhibits important lensing effects in both the two-point function (or power spectrum) and the four-point function (or trispectrum) due to the sharp decline in the intrinsic CMB power associated with Silk damping.

The temperature and polarization anisotropy power spectra or two-point correlation functions of the CMB are a cornucopia of cosmological information. If the underlying fluctuations are Gaussian, these spectra encapsulate all of the statistical information contained by the CMB. However, as the photons propagate through the large-scale structure of the Universe, non-Gaussainities in the CMB temperature fluctuations are induced due to non-linear processes associated with the secondary anisotropies.

In principle, the contribution made to the observed CMB from weak lensing can most likely be subtracted if sufficiently accurate high resolution observations are available. The statistical nature of the unlensed CMB fields could limit the accuracy to which the lensing field can be reconstructed although there have been strong arguments that polarization removes this limit in models where the only source of B-mode polarization on small scales comes from lensing. In this ideal case we could recover the unlensed Gaussian CMB and use it for any further analysis.

Methods have been developed for a direct reconstruction of the projected matter density from the CMB anisotropy. Zaldarriaga and Seljak derived a reconstruction by averaging over quadratic combinations of the derivatives of the CMB field [29]. This reconstruction could be used to search for clusters at high redshifts or to study density fluctuations on the largest scales that are

not otherwise observable. In addition to this, it can be correlated with other maps such as those of the SZ effect, X-ray background and weak lensing surveys. The three-point function for the unlensed CMB is zero. Gravitational lensing alone does not produce a detectable three-point signal (or bispectrum) because there are equal number of hot and cold spots [30] but it does however combine with other low redshift effects such as the SZ and ISW effects and provides a probe for the temperature-lensing potential correlation on large scales. On small scales the three point function vanishes even for the lensed sky [31]. The four-point function (or trispectrum) has an interesting signal on small angular scales on which the lensing potential is, effectively, statistically independent of the temperature field and provides an important probe of the lensing potential power spectrum itself. For observations with high sensitivity this signal should be easily distinguishable from the cosmic variance. This idea forms the basis for the reconstruction methods used in this work.

In addition to directly controlling the noise properties of power spectrum estimators, the angular trispectrum can be used for finding optimal quadratic statistics of the weak lensing effect. Zaldarriaga [32] considered the lensing trispectrum in the small-scale or flat-sky approximation and Hu [33] extended the derivation to include the full trispectrum and related it to the underlying deflection power spectrum. These estimators can also be extended for lensing reconstructions with the CMB polarization [34, 35, 36, 37, 38]. Reconstructions of the lensing potential in harmonic space require that the experiment covers the entire sky with no galactic cut or point sources. We thus go on to investigate a real space approach to lensing reconstruction developed by [39]. This estimator allows for a non-uniform sky coverage, galactic cuts and the removal of bad pixels cause by foreground objects. This real space approach is equivalent to the harmonic space estimator on large scales.

The effect of lensing on the CMB has recently been detected using a quadratic estimator in cross-correlation with radio sources and galaxies using data from the Wilkinson Microwave Anisotropy Probe (WMAP) [40, 41] and directly from the temperature anisotropy map by teams working on the Atacama Cosmology Telescope (ACT) [42] and the South Pole Telescope (SPT) [43]. The ACT and SPT teams have further made detections through the cross-correlation with other maps.

[44, 45]

This thesis is structured as follows. The theoretical and observational pillars of the Big Bang Theory are discussed in Chapter 2, with a focus on the expansion of the Universe and the CMB. Also included are discussions of the Cosmological Principle, Einstein's Theory of General Relativity, the abundance of elements from Big Bang Nucleosynthesis and the formation of large-scale structures from primordial density perturbations. In Chapter 3 we develop the weak lensing theory and derive an expression for the deflection angle. We define the effective lensing convergence and how it is related to the primordial density perturbations and discuss the effect the lensing has on the power spectrum of the CMB. The bulk of the research performed in preparation for this thesis is presented in Chapter 4 where we discuss two methods of reconstructing the lensing convergence from the observed temperature anisotropies. After a preliminary discussion on map making techniques, we investigate the harmonic space quadratic estimator, as presented in [31]. We first summarize the derivation of the estimator and proceed to discuss its implementation before presenting the results of our analysis. We then change our focus to an analysis of the real space estimator presented in [39]. We begin with the derivation of the estimator and discuss the shape of the filter used its implementation. Maps of the recovered convergence are shown along the power spectrum. These results are largely covered in previous work [39]. The estimators turn out to under-perform for large distortions, where the linear approximation of the Taylor expansion used in their derivation is no longer valid. In Chapter 5 we investigate whether this could be an important effect in reconstruction of the lensing convergence and how constraints on the lensing convergence amplitude would be affected by not taking this effect into account. Finally, we compare our results with the data from the first reported detections of the lensing convergence power spectrum made by the ACT and SPT collaborations. The work of Chapter 5 is original.

CHAPTER 2

Big Bang Cosmology

In this chapter we explore several key theoretical principles and observational pillars underlying Big Bang cosmology. We begin with a brief description of the cosmological principle and Einstein's theory of General Relativity, the two theoretical foundations of the model. We go on to discuss the observational evidence in support of the Big Bang, focusing on the expansion of the Universe and the Cosmic Microwave Background (CMB) in more detail. We also discuss the large-scale structure of the Universe and Big Bang Nucleosynthesis.

2.1 Theoretical Foundations

2.1.1 The Cosmological Principle

As observational methods have improved we have catalogued a vast number of galaxies and galaxy clusters further back in time and on larger scales there is strong evidence that the Universe becomes smooth. This supports the use of the cosmological principle, which states that on sufficiently large scales, the properties of the Universe are the same for all observers. Thus, the large-scale Universe possesses two important properties, those of homogeneity (the Universe looks the same at each point) and isotropy (the Universe looks the same in every direction). Further evidence for the cosmological principle comes from observations that the CMB has a

temperature distribution which is nearly uniform across the entire sky, a fact which strongly supports the idea that the matter which was coupled to this radiation was uniformly distributed. The cosmological principle however is not exact and the study of the departures from homogeneity and isotropy forms an important research topic in modern cosmology.

2.1.2 General Relativity

Modern cosmology is based on Einstein's theory of general relativity. In essence, the theory of general relativity, published by Albert Einstein in 1916 [46] is a geometric theory describing the force of gravity. It is the most widely accepted theory for gravitation in modern physics, astrophysics and cosmology. The theory generalizes Newton's law of universal gravitation and Einstein's own theory of special relativity, which only applies to inertial frames, to provide a unified description of gravity as a geometric property of space and time. Of crucial importance is that the theory relates the curvature of spacetime directly to the stress-energy of any matter and radiation that is present. A system of partial differential equations known as the Einstein field equations specifies this relation. Apart from its profound astrophysical implications such as the prediction of the existence of gravitational waves and black holes, general relativity is the basis for modern cosmology and provides the necessary framework for describing a consistently expanding universe.

Einstein's Theory of Gravitation

Einstein realized that the space that we inhabit is not flat, except locally and approximately, and proceeded to combine the principle of equivalence, which equates gravitational and inertial mass, with the requirement of general covariance. The fact that the inhomogeneous gravitational field near a massive object is equivalent to a curved spacetime means that the laws of physics must be described by generally covariant tensor equations. The law of gravitation is thus a covariant relation between mass density and curvature. Einstein searched for the simplest form that this relationship could possibly take.

Curved Spacetime

The description of a curved spacetime involves at least the second derivatives of the metric tensor $g_{\mu\nu}$. The curvature is best described in terms of the fourth-rank Riemann tensor

$$R^{\alpha}_{\beta\gamma\sigma} = \frac{\partial\Gamma^{\alpha}_{\beta\sigma}}{\partial x^{\gamma}} - \frac{\partial\Gamma^{\alpha}_{\beta\gamma}}{\partial x^{\sigma}} + \Gamma^{\alpha}_{\rho\gamma}\Gamma^{\rho}_{\beta\sigma} - \Gamma^{\alpha}_{\rho\sigma}\Gamma^{\rho}_{\beta\gamma}, \tag{2.1.1}$$

where the Greek indices run over the time and space dimensions of a four-dimensional spacetime. Another useful tool in the description of the curvature is the second-rank Ricci tensor $R_{\beta\gamma}$ which is obtained by contracting the Riemann tensor

$$R_{\beta\gamma} = R^{\alpha}_{\beta\gamma\alpha} = \delta^{\sigma}_{\alpha}R^{\alpha}_{\beta\gamma\sigma} = g^{\alpha\sigma}R^{\alpha}_{\beta\gamma\sigma}. \tag{2.1.2}$$

Lastly, we can contract the Ricci tensor to obtain the Ricci scalar

$$R = g^{\beta\gamma}R_{\beta\gamma}. \tag{2.1.3}$$

From here we are in a position to define the Einstein tensor $G_{\mu\nu}$ as

$$G^{\mu\nu} = R^{\mu\nu} - \frac{1}{2}g^{\mu\nu}R. \tag{2.1.4}$$

The stress-energy tensor

We now turn to the distribution of matter throughout the Universe. Suppose that non-relativistic matter was continually distributed as an ideal fluid throughout the Universe. We can then conveniently describe the energy density, pressure and shear of the fluid by the stress-energy tensor $T_{\mu\nu}$. The stress-energy tensor cast in its purely diagonal form is

$$T_{\mu\mu} = (p + \rho c^2)\frac{v_{\mu}v_{\mu}}{c^2} - pg_{\mu\mu}, \tag{2.1.5}$$

and the time-time component is ρc^2. We can then extend the laws of conservation of energy and three-momentum to give the law of conservation of four-momentum

$$\frac{DT_{\mu\nu}}{Dx_{\nu}} = 0, \tag{2.1.6}$$

where the capital D implies the total derivative. Thus we see that the stress-energy tensor is divergence free.

Einstein's Field Equations

The dynamics of the metric are governed by the Einstein field equations which relate the Einstein tensor, given in Equation (2.1.4) to the stress-energy tensor of the matter contained in spacetime. Returning to the Einstein tensor we note that this tensor has zero covariant divergence and from the law of conservation of four-momentum given in Equation (2.1.6), we see that it should be proportional to $T^{\mu\nu}$

$$G^{\mu\nu} = \frac{8\pi G}{c^4} T^{\mu\nu}. \tag{2.1.7}$$

These are known as the Einstein field equations where the correct constant of proportionality has been included. So far, all of this has been done in the weak field limit and the stress-energy tensor is the sum of the stress-energy tensors for various components of the Universe such as baryons, radiation and dark matter. Einstein's equations express the idea that the energy density, pressure and shear in $T^{\mu\nu}$ determines the geometry of the spacetime of the Universe.

2.2 The Expanding Universe

2.2.1 Hubble's Law

In the late 1920s, Hubble, using the 100-inch Hooker Telescope, measured the distances to a number of galaxies [47]. He combined these measurements with data provided by Slipher of their recessional velocity to produce a plot of speed against distance. In one of the most important pieces of observational evidence in cosmology he noticed that all galaxies, except for the closest ones, were moving away from us. Furthermore, he found that the greater the distance, the greater the apparent speed of recession:

$$\mathbf{v} = H_0 \mathbf{r}, \tag{2.2.8}$$

where $\mathbf{v}$ and $\mathbf{r}$ are the speed of recession and distance to the galaxy respectively. The linear relation between distance and recessional velocity is now known as Hubble's law and H_0 is called the Hubble parameter. Although it is true that we observe all galaxies receding from us as if we were at the centre of the Universe, the same is true for any other observer elsewhere in

the Universe. This leads us to conclude that at some point in the distant past, everything in the Universe was much closer together. Ultimately by retracing the history of the Universe we arrive at a singularity known as the Big Bang.

2.2.2 Redshift and scale factor

Radiation traveling through cooler matter in stellar atmospheres excites the atoms at well defined wavelengths which results in very clear characteristic dark absorption lines in the emission spectrum. By studying how these spectral lines are modified as a result of the expansion of the Universe it is possible to define a useful measure of the distance to an object emitting the light. Consider radiation emitted by stars and distant galaxies with wavelength $\Lambda_{rest} = c/v_{rest}$ at time t in the reference frame of the star or galaxy. The cosmological expansion of the Universe causes the wavelength to be stretched to Λ_{obs} when observed by an observer on the Earth. The shift in the spectrum is in the red direction so $\Lambda_{obs} > \Lambda_{rest}$ and we thus call this measure the redshift

$$z = \frac{\Lambda_{obs} - \Lambda_{rest}}{\Lambda_{rest}}. \tag{2.2.9}$$

The ratio of the wavelengths actually measured by the observer on Earth would then be

$$1 + z = \frac{\Lambda_{obs}}{\Lambda_{rest}} = \frac{1}{a(t)}, \tag{2.2.10}$$

where $a(t)$ is the scale factor of the Universe. It is important to note that the cosmological redshift is caused by the expansion of the Universe. It is however possible in the case of nearby stars and galaxies to observe a kinematic effect which can be more important than the cosmological expansion. This may result in a Doppler redshift or a Doppler blueshift for a receding or approaching source respectively.

The Robertson-Walker Metric

The metric which is most frequently used in describing the Universe in modern cosmology was derived by Howard Robertson and Arthur Walker [48]. The metric describes a curved four dimensional space and the spacetime line element separating two events takes the form

$$ds^2 = c^2\, dt^2 - dl^2, \tag{2.2.11}$$

where dl^2 is the three dimensional spatial distance. In spherical polar coordinates then the line element is

$$ds^2 = c^2\,dt^2 - a^2(t)\left[\frac{dr^2}{1-Kr^2} + r^2\,d\theta^2 + r^2\sin^2\theta\,d\phi^2\right], \tag{2.2.12}$$

where k is the curvature parameter and can take the values $1, 0$ or -1 and r is a dimensionless comoving coordinate. We can thus see from this metric that a Universe which is homogeneous and isotropic at a given time remains so. A galaxy situated at some position in the Universe will remain at that point because it is only the scale of spatial distances $a(t)$ which changes and all spatial displacements will remain zero. The metric equation thus reduces to

$$ds^2 = c^2\,dt^2. \tag{2.2.13}$$

Such an expanding frame is known as a comoving frame. An observer at rest in this frame is considered to be a fundamental observer and a Universe which appears to be homogeneous to such an observer must also be isotropic. Conversely, an observer moving with a relative motion will not observe isotropy. We can define as new set of extremely useful coordinates in the preferred comoving frame. One should note here that a fundamental observer may not see all objects radially receding due to the peculiar velocities in other directions. We define the new comoving coordinates χ by integrating over

$$d\chi = \frac{dr}{\sqrt{1-Kr^2}}. \tag{2.2.14}$$

Using this in the metric equation we get

$$ds^2 = c^2\,dt^2 - a^2(t)\left[d\chi^2 + f_K^2(\chi)(d\theta^2 + \sin^2\theta\,d\phi^2)\right], \tag{2.2.15}$$

where

$$f_K(\chi) \equiv \begin{cases} \sin\chi & K = 1 \\ \chi & K = 0 \\ \sinh\chi & K = -1 \end{cases} \tag{2.2.16}$$

2.2.3 Friedmann-Lemaître Cosmologies

Much of the work done in observational cosmology, including this dissertation assumes a body of material on standard homogeneous cosmological models. Here we will summarize a few of the key basic features of relativistic cosmology. The Robertson-Walker metric was derived for a model describing our homogeneous and isotropic Universe. We recall here that it can be written as a purely diagonal tensor and that it contains the curvature parameter K.

The Friedmann Equations

The stress-energy tensor $T_{\mu\nu}$ was given in its diagonal form in Equation (2.1.5). A comoving observer with velocity v=(c,0,0,0) will observe the following components for the stress energy tensor:

$$T_{00} = \rho c^2 \qquad \text{and} \qquad T_{11} = T_{22} = T_{33} = \frac{pa^2}{1 - Kr^2} \tag{2.2.17}$$

From the Einstein field equations (2.1.7) we require that G_{00} and G_{11} be equal to T_{00} and T_{11}. We can reduce the analysis to only these two components as the equality of the space-space components would make a full analysis to be redundant. After a fair amount of algebra, it can be shown that

$$G_{00} = \frac{3(\dot{a}^2 + Kc^2)}{(ca)^2} \tag{2.2.18}$$

$$G_{11} = -\frac{1}{c^2}\frac{a\ddot{a} + \dot{a}^2 + Kc^2}{1 - Kr^2}, \tag{2.2.19}$$

where the overdot and double overdot imply a first derivative and second derivative with respect to time. Making use of these two equations in the Einstein field equations we obtain two distinct relations for $a(t)$,

$$\frac{\dot{a}^2 + Kc^2}{a^2} = \frac{8\pi G}{3}\rho \tag{2.2.20}$$

$$\frac{2\ddot{a}}{a} + \frac{\dot{a} + Kc^2}{a^2} = \frac{-8\pi G}{c^2}p. \tag{2.2.21}$$

These equations are known as the Friedmann equations and quite remarkably were discovered by Friedmann in 1922 [49], a full seven years before Hubble discovered the expansion of the

Universe and at a time when Einstein himself did not believe his own equations because they did not allow for a static universe. The expansion or contraction of the Universe is inherent to the Friedmann equations. Before moving on, note the following notation: ρ denotes the mass density, ρc^2 the energy density, $\rho_m c^2$ in future shall denote the energy density of matter including baryons, leptons, dark matter, etc and $\rho_r c^2$ the energy density of radiation.

The first of the equations relates the rate of expansion $\dot{a}$ to mass density in the Universe and clearly shows that as the mass density increases so does the rate of expansion. The second of the equations importantly allows for the expansion to accelerate. Subtracting Equation (2.2.20) from Equation (2.2.21) results in

$$\frac{2\ddot{a}}{a} = -\frac{8\pi G}{3c^2}(\rho c^2 + 3p). \tag{2.2.22}$$

This shows us that the acceleration increases with decreasing pressure and energy density. We define the critical density

$$\rho_{crit}(t) \equiv \frac{3H^2(t)}{8\pi G}, \tag{2.2.23}$$

where $H(t) = \dot{a}/a$ is the Hubble parameter, and the density parameter

$$\Omega(t) \equiv \frac{\rho(t)}{\rho_{crit}(t)}. \tag{2.2.24}$$

Making use of these in the Friedman Equation (2.2.20) gives

$$\Omega(t) - 1 = \frac{Kc^2}{H^2(t)a^2(t)}. \tag{2.2.25}$$

At the present time, denoted by t_0, the mass density is ρ_0, the cosmic scale factor $a_0 = 1$, the Hubble parameter $H_0 = \dot{a_0}$ and a density parameter Ω_0. The first of the Friedmann equations (2.2.20) becomes

$$\dot{a_0}^2 = \frac{8}{3}\pi G\rho_0 - Kc^2 \tag{2.2.26}$$

$$= H_0^2\Omega_0 - Kc^2 \tag{2.2.27}$$

which can be written as

$$Kc^2 = H_0^2(\Omega_0 - 1) \tag{2.2.28}$$

This is the Newtonian relation and from Equation (2.2.28), the relationship between the Robertson-Walker curvature parameter K and the present density parameter emerges. We can see that K values $+1,\ 0$, and -1 correspond to an over-critical density $\Omega_0 > 1$, a critical density $\Omega_0 = 1$ and and under-critical density $0 < \Omega_0 < 1$ respectively.

General solution

In generalizing from H_0 to the time dependent Hubble parameter $H(t) = \dot{a}/a$, the critical density and the density parameter must also become time dependent functions

$$\rho_c(t) = \frac{3}{8\pi G} H^2(t), \tag{2.2.29}$$

$$\Omega(t) = \frac{\rho(t)}{\rho_c(t)}. \tag{2.2.30}$$

We can thus generalize Equation (2.2.28) to

$$Kc^2 = H^2 a^2 (\Omega - 1). \tag{2.2.31}$$

One can clearly see that in the case $K = 0$ we can eliminate Kc^2 and get

$$H^2 a^2 (\Omega - 1) = H_0^2 (\Omega_0 - 1). \tag{2.2.32}$$

Making use of these substitutions in Equation (2.2.20) we get an expression for the Hubble parameter as a function of the cosmic scale

$$H(a) \equiv \frac{\dot{a}}{a} = H_0 \sqrt{\frac{1 - \Omega_0}{a^2} + \Omega(a)}. \tag{2.2.33}$$

The dependence on a of $\Omega(a)$ is left unspecified and various types of energy densities with different dependencies can contribute. We can use Equation (2.2.33) to solve for what is known as the look-back time $t(z)/t_0$ or $t(a)/t_0$

$$\int_0^{t(a)} dt = \int_1^a \frac{da}{aH(a)}, \tag{2.2.34}$$

from which we see that the age of the Universe at a given redshift is $1 - t(z)/t_0$.

Einstein Universe

We now turn our attention to Einstein's static universe. This model is defined by $a(t)$ being a constant $a_0 = 1$ such that $\dot{a} = 0$ and $\ddot{a} = 0$ and the age of the universe is thus infinite. In this case the Friedmann equations reduce to

$$Kc^2 = \frac{8\pi}{3} G\rho_0 = -\frac{8\pi}{c^2} Gp_0. \tag{2.2.35}$$

In order for the mass density to be positive, as we observe it to be today, we must have $K = +1$ which implies that the pressure of the matter p_0 must be less than zero. Einstein corrected this by introducing a constant Lorentz invariant term $\Lambda g_{\mu\nu}$ where Λ, known as the cosmological constant is a tiny correction to the geometry. The Einstein tensor then becomes

$$G_{\mu\nu} = R_{\mu\nu} - \frac{1}{2} g_{\mu\nu} R - \Lambda g_{\mu\nu}, \tag{2.2.36}$$

and the Friedmann equations become

$$\frac{\dot{a}^2 + Kc^2}{a^2} - \frac{\Lambda}{3} = \frac{8\pi G}{3}\rho, \tag{2.2.37}$$

$$\frac{2\ddot{a}}{a} + \frac{\dot{a}^2 + Kc^2}{a^2} - \Lambda = -\frac{8\pi G}{c^2}. \tag{2.2.38}$$

A positive value for Λ curves the spacetime to counteract the gravitational force of matter which would otherwise cause the universe to collapse inwards on itself and the value for Λ is finely adjusted to give a static solution. The pressure of matter must be small or else galaxies would exhibit random motion much akin to molecules in a gas under pressure and so for convenience we set it to zero. Accordingly, Equation (2.2.37) becomes

$$Kc^2 - \frac{\Lambda}{3} = \frac{8\pi G}{3}\rho. \tag{2.2.39}$$

In a spatially flat universe with $K = 0$ one obtains

$$\rho_\Lambda = \frac{\Lambda}{8\pi G} = -\rho_0. \tag{2.2.40}$$

The solution is extremely unstable, a fact which Einstein seemingly failed to notice. The value of Λ has to be extraordinarily fine-tuned and even the slightest imbalance between Λ and ρ would make $\ddot{a}$ non-zero which would clearly destroy the basic premise of the model. After Hubble's

discovery of the expansion of the Universe Einstein abandoned this theory and later described as the greatest blunder of his lifetime [50].

The Friedmann-Lemaître Universe

In the Einstein tensor, Λ is a correction to the geometry. However, mathematically speaking the Friedmann equations (2.2.37 and 2.2.38) are not altered if Λ is moved to the right-hand-side of the equality. In this case, Λ then represents a correction to the stress-energy tensor. The physical representation of this is that of an ideal fluid with energy density $\rho_\Lambda = \Lambda/8\pi G$ and negative pressure $p_\Lambda = -\rho_\Lambda c^2$. In this model one can clearly see that a positive value for Λ implies a cosmic repulsion which opposes the gravitational force and a negative value for Λ acts as an additional attractive gravitational force. The cosmology so described with positive Λ is known as the Friedmann-Lemaître Universe [51, 52, 53]and it is strongly supported by observations of non-zero Λ. In this model of the universe the total density parameter Ω_0 is split into matter, radiation and Λ terms

$$\Omega_0 = \Omega_m + \Omega_r + \Omega_\Lambda, \tag{2.2.41}$$

where Ω_m, Ω_r and Ω_Λ are the matter, radiation and Λ density parameters and

$$\Omega_r \equiv \frac{\rho_r}{\rho_c}, \qquad \Omega_\Lambda \equiv \frac{\Lambda}{8\pi G\rho_c} = \frac{\Lambda}{3H_0^2}. \tag{2.2.42}$$

We can then make use of Equation (2.2.40) to determine the value for Λ

$$-\Lambda = 8\pi G\rho_0 = 3\Omega_0 H_0^2 \approx 1.3 \times 10^{-52} c^2 m^{-2} \tag{2.2.43}$$

This value is extremely small. So small in fact that it is the smallest quantity known in physics. It would be far more natural for the value of Λ to be zero and this remains one of the greatest unsolved problems of cosmology.

Energy-Momentum Conservation

If we differentiate the first of the Friedmann equations (2.2.20) with respect to time

$$\frac{d}{dt}(\dot{a}^2 + Kc^2) = \frac{8\pi G}{3}\frac{d}{dt}(\rho a^2), \tag{2.2.44}$$

we obtain an equation of second order in the time derivative

$$2\dot{a}\ddot{a} = \frac{8}{3}\pi G(\dot{\rho}a^2 + 2\rho a\dot{a}). \tag{2.2.45}$$

We can then use Equation (2.2.22) to replace the 2nd order time derivative so that

$$\frac{a}{c^2}(\rho c^2 + 3p) = \dot{\rho}\frac{a^2}{\dot{a}} + 2\rho, \tag{2.2.46}$$

and multiplying by c^2/a to obtain

$$\dot{\rho}c^2 + 3H(\rho c^2 + p) = 0. \tag{2.2.47}$$

Here, all terms have the dimension of energy density and one can quite clearly see that the change in energy per unit time is zero. Locally, this can be interpreted as the law of energy conservation. Alternatively, one can arrive at this same result by allowing the total energy content in a comoving volume a^3 to be

$$E = (\rho c^2 + p)a^3. \tag{2.2.48}$$

The expansion of the Universe is adiabatic if there is no net inflow or outflow of energy so that

$$\frac{dE}{dt} = \frac{d}{dt}\left[(\rho c^2 + p)a^3\right]. \tag{2.2.49}$$

If the pressure p does not vary with time, then changes in ρ and a will compensate for each other and Equation (2.2.47) follows from taking the derivative. Equation (2.2.47) is trivially integrated

$$\int \frac{\dot{\rho}(t)c^2}{\rho(t)c^2 + p(t)}dt = -3\int \frac{\dot{a}(t)}{a(t)}dt, \tag{2.2.50}$$

if the equation of state (the relation between the energy density and the pressure) of the Universe is known.

Entropy conservation and the Equation of State

The law of conservation of entropy S is not implied by the Friedmann equations and must be specifically assumed as shown later

$$\dot{S} = 0. \tag{2.2.51}$$

We can now make an ansatz for the equation of state of the Universe. We let the pressure be proportional to the energy density with some factor of proportionality w which remains constant in time so that

$$p = w\rho c^2. \tag{2.2.52}$$

It turns out that this is indeed the most general equation of state with a Robertson-Walker metric. By making use of this ansatz in Equation (2.2.50) we obtain the relation between the energy density and the scale factor of the Universe

$$\rho(a) \propto a^{-3(1+w)} = (1+z)^{3(1+w)}. \tag{2.2.53}$$

The value of w follows from the adiabaticity condition and we can anticipate its value in three specific cases:

Matter dominated Universe

Here we make the assumption that the Universe is filled with cold matter which takes the form of a pressureless, $p = 0$, non-radiating dust. The implication of this from Equation (2.2.52) is that $w = 0$ and the density evolves according to

$$\rho_m(a) \approx a^{-3} = (1+z)^3. \tag{2.2.54}$$

Radiation dominated universe

In this case we assume that the Universe is filled with a ultra relativistic, hot gas made up of elastically scattering particles with energy density ϵ. From statistical mechanics we have the relationship between the pressure and the energy density

$$p_r = \frac{1}{3}\epsilon = \frac{1}{3}\rho_r c^2. \tag{2.2.55}$$

This leads to the result that $w = 1/3$ and so the radiation density evolves according to

$$\rho_r(a) \propto a^{-4} = (1+z)^4. \tag{2.2.56}$$

Vacuum energy

A universe dominated by the vacuum energy corresponds to a flat, static universe ($\ddot{a} = 0,\ \dot{a} = 0$), devoid of dust and radiation but with a cosmological term Λ. Here we obtain the result

$$p_\Lambda = -\rho_\Lambda c^2, \tag{2.2.57}$$

which leads to a constant of proportionality in the equation of state $w = -1$. Thus we see that the pressure of the vacuum energy is negative which is in agreement with Equation (2.2.40). In the equation of state ρ_Λ and p_Λ are scale-independent constants.

2.3 Big Bang Nucleosynthesis

In many ways, one of the most compelling pieces of evidence in favour of the Hot Big Bang theory is the observed abundance of elements in the Universe. In the past, it was believed that elements heavier than hydrogen were created via nuclear fusion reactions within stars. While, this process most certainly does give rise to the creation of heavier elements it was ultimately recognized that all of the light elements namely, deuterium, helium-3, lithium and helium-4 could not have been created in this manner. The Universe began its life as a massive nuclear fusion reactor that produced the matter that we observe today. Big Bang Nucleosynthesis (BBN) refers to an early phase of the Universe that involved the production of nuclei other than those of H-1, the lightest isotope of Hydrogen contain only one proton. Primordial nucleosynthesis began moments after the Big Bang and is responsible for the production of the isotopes of light elements Helium (He) and Lithium (Li). The comparison between the predicted and observed primordial abundances of the light nuclides provides a unique window on the early evolution of the Universe and an important probe of the standard models of particle physics and cosmology. BBN took place throughout the entire observable universe and lasted roughly 17 minutes (during the period from 3-20 minutes after the Big Bang). After this time the density and temperature of the Universe fell below those required for nuclear fusion to take place.

Irrespective of the initial conditions of the Universe, BBN theory predicts that He-4 made up roughly 25% of the primordial nuclear soup. The He-4 abundance is of particular importance to cosmological models are there is a far greater amount of He-4 than could have been produced by

nuclear reactions in stars and it provides a useful test of the Big Bang theory. A helium abundance very much different to 25% would present an extremely serious challenge to the theory.

While He-4 is very stable and difficult to destroy, deuterium (the isotope of hydrogen containing 1 neutron) is not particularly stable and is relatively easy to destroy. Due to the high stability of He-4, there is a strong tendency for two deuterium nuclei to fuse together to form He-4. Had the temperature of the Universe remained higher for a longer period of time, all of the deuterium would have been converted in this manner. As such, the amount of deuterium left in the Universe is highly sensitive to the initial conditions. The denser and hotter the early Universe, the less deuterium remains. No known process that produce significant amounts of deuterium exist and thus observations of the deuterium abundance [54, 55, 56, 57] suggest that the Universe is not infinitely old, which is in agreement with Big Bang theory.

2.4 The Cosmic Microwave Background

The Cosmic Microwave Background (CMB), discovered in 1965 by A. Penzias and R. Wilson [16], dominates the energy content in the radiation from beyond our galaxy. The CMB shows us a picture of the universe when it was 300, 000 years old and its photons last scattered off electrons at redshift 1100. Since then they have been streaming freely through space. These photons are the oldest visible light in the universe and as such provide the most powerful probe that we have into the physics of the early universe. The spectrum of the CMB is well described by a blackbody function with a temperature $T = 2.725$ K. The specific intensity of a gas of photons with a blackbody spectrum is

$$I_\nu = \frac{4\pi\hbar\nu^3/c^2}{\exp[2\pi\hbar\nu/k_BT] - 1}. \tag{2.4.58}$$

This prediction of Big Bang cosmology is in remarkable agreement with the observations by the Far InfraRed Absolute Spectrophotometer (FIRAS) instrument on the COBE satellite [17] and the spectral form is one of the main pieces of observational evidence available in support of the

hot Big Bang model. The lack of any observed deviations from a blackbody spectrum provides important constraints for physical processes over cosmic history at redshifts $\lesssim 10^{-7}$ although all current viable models predict a very nearly Planckian spectrum and are thus not strictly limited.

Another important property the CMB, is the temperature anisotropies: that is, the variation in temperature, or intensity from one part of the CMB to another. These were first detected by the COBE satellite [18] and since then the quest to map the sky at increasing levels of sensitivity and angular resolution has been pursued relentlessly. A series of ground and balloon based experiments such as Balloon Observations Of Millimetric Extragalactic Radiation And Geophysics (BOOMERanG) [58, 59] and the Millimeter Anisotropy Experiment Imaging Array (MAXIMA) [60, 61, 62] was joined by the first results from NASA's Wilkinson Microwave Anisotropy Probe (WMAP) in 2003 [63]. These studies have led us to a spectacular confirmation of the Standard Model of Cosmology. When combined with other astrophysical data, the CMB anisotropy measurements place precise constraints on a number of cosmological parameters and have launched us into a new era of precision cosmology.

2.4.1 Description of Anisotropies

According to observations, the CMB contains anisotropies at the 10^{-5} level, over a wide range of angular scales. It is normal to express these anisotropies by means of a spherical harmonic expansion of the CMB sky

$$T(\theta, \phi) = \sum_{lm} Y_{lm}(\theta, , \phi). \tag{2.4.59}$$

Most of the information is contained in the temperature two-point correlation function, which is the variance as a function of the separation θ.

The Monopole

The mean temperature of the CMB is $T_\gamma = 2.725 \pm 0.001$ K, which is considered to be the monopole component (a_{00}) of the CMB maps. All mapping experiments involve difference measurements and are insensitive to this average level. Measurements of the monopole can be made

only by instruments with absolute temperature devices such as FIRAS [64]. The observations of the spectrum thus far are consistent with a blackbody distribution over more than three decades in frequency.

The Dipole

The largest anisotropy is the dipole (l=1) spherical harmonic and has an amplitude 3.346 ± 0.017 mK [63]. We interpret this dipole to be the result of a Doppler shift caused by the motion of the solar system relative to the nearly isotropic blackbody field and this has been confirmed by measurements of the radial velocities of local galaxies [65]. An observer with velocity $\beta = v/c$ relative to an isotropic Planckian radiation field with temperature T_0 will observe a Doppler-shifted temperature pattern

$$\begin{aligned} T(\theta) &= T_0(1-\beta^2)^{1/2}/(1-\beta\cos\theta), \\ &\approx T_0\left(1+\beta\theta+\frac{\beta^2}{2}\cos 2\theta+\mathcal{O}(\beta^3)\right). \end{aligned} \tag{2.4.60}$$

At every point in the sky one observes a blackbody spectrum with temperature $T(\theta)$ and the spectrum of the dipole is the differential of a blackbody spectrum [66]. The dipole is a frame dependent quantity and as such, we can define the absolute rest frame of the Universe to be that in which the CMB dipole vanishes. Our velocity relative to the local group, the velocity of the Earth around the Sun and any velocity of the receiver relative to the Earth are normally removed for studies of the CMB anisotropy.

Higher order multipoles

The excess variance at multipoles greater than $l = 1$ is resultant from the perturbations in the density of the early Universe that were manifest at the epoch of the last scattering of the CMB photons. At this time, the hydrogen and helium nuclei could hold onto electrons thus becoming electrically neutral and the photons can stream freely through space. Prior to this, the photons were tightly coupled to the baryons. In hot Big Bang models, this takes place at $z \simeq 1100$ and depends very little on the details of the model.

Theoretical models generally predict that the a_{lm} modes are Gaussian random fields. This has been tested and it has been found that this is an extremely good approximation [67], with only relatively weak indications of non-Gaussianity or large scale statistical anisotropy. Although some early Universe models allow for a primordial non-Gaussianity [68], the signatures found in the WMAP data are generally taken to be subtle foreground or instrumental artifacts [69, 70]. With the assumption of Gaussian statistics, and if there is no preferred axis, then it is the variance of the temperature field instead of the individual a_{lm} which carries the cosmological information. This means that the anisotropies are fully described by the power spectrum in l. The power at each l is $(2l+1)C_l/(4\pi)$ where $C_l \equiv \langle |a_{lm}|^2 \rangle$, and a statistically isotropic sky means that all m's are equivalent. For an idealized full-sky observation, the variance of each measured C_l is $[2/(2l+1)]C_l^2$. This is known as the cosmic variance and arises due to the fact that each C_l is χ^2 distributed with $(2l+1)$ degrees of freedom for our observable volume of the Universe. For observations with only partial sky coverage, the cosmic variance is increased by a factor $1/f_{sky}$, where f_{sky} is the fraction of the sky covered, and the modes become partially correlated. It is important to note that theories only predict the expectation value of the power spectrum while our sky is only a single realisation of the CMB. Thus, the cosmic variance is an unavoidable source of uncertainty when constraining models. The cosmic variance dominates the scatter at lower ls, while the effects of instrumental resolution and noise dominate at higher l's [71].

2.4.2 Physics of Anisotropies

The anisotropies are affected by cosmological parameters though the well understood physics of the evolution of linear perturbations within the framework of a background FRW cosmology. There are very effective and publicly-available software codes for computing the CMB anisotropy, polarization and matter power spectra such as `CMBFAST` [72] and the Code for Anisotropies in the Microwave Background (`CAMB`) [73]. A description of the physics underlying the CMB power spectrum can be separated into 3 main regions as seen in Figure (2.1).

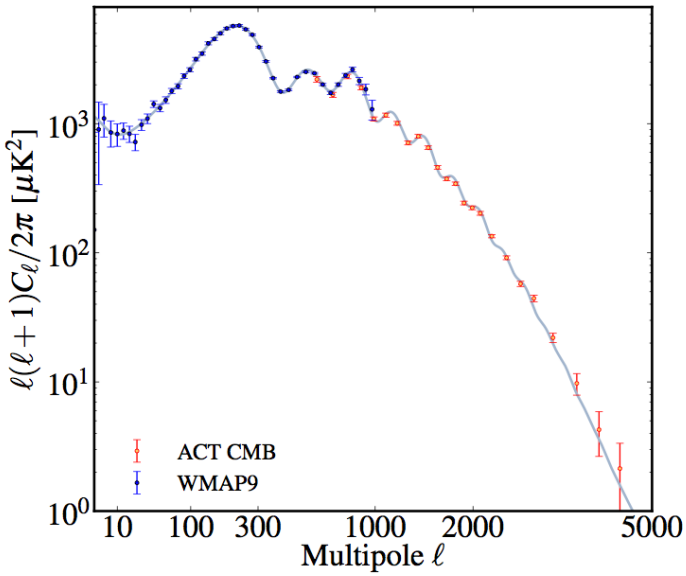

Figure 2.1: **CMB temperature power spectrum:** CMB temperature power spectrum measurements from WMAP 9-year data [1, 2], SPT [3] and ACT [4]. The solid line is the best-fit model from the ACT 148 GHz data combined with WMAP-7 data [5]. The dashed line represents the primordial CMB component for the same best-fit model.

The Sachs-Wolfe Plateau ($l \lesssim 100$):

At last scattering, the angle subtended by the Hubble radius (the horizon scale) corresponds to $l \simeq 100$. Anisotropies at large scales have not evolved significantly and hence give a good representation of the initial conditions.The combination of gravitational redshift and intrinsic temperature fluctuations leads to the Sachs-Wolfe effect [24]. Making the assumption that a nearly scale invariant spectrum of density perturbations was laid down at early times the power spectrum is approximately constant at low l. Time variation of the potentials leads to increase in the several lowest multipoles. Any deviation from the total equation of state $w = 0$ has such an effect. Thus the dominance of Dark Energy at low redshifts causes the spectrum to rise above the plateau at low l. This is called the integrated Sachs-Wolfe effect (ISW).

The Acoustic Peaks ($100 \lesssim l \lesssim 1000$):

On angular scales smaller than approximately a degree, the rich structure in the anisotropy spectrum is the consequence of gravity-driven acoustic oscillations which occurred before the atoms in the Universe became neutral. Prior to the Universe becoming neutral, the proton-electron plasma was very tightly coupled to the photons, so much so that the components acted as a single 'photon-baryon fluid'. After recombination, the baryons and radiation decoupled and radiation was free to stream through space towards us. At this point the phases in the oscillations were frozen in and projected onto the sky as a series of harmonic peaks. The main peak is the mode that went through one quarter of a period, reaching maximal compression. These peaks have been a clear theoretical prediction going back about 40 years [74] and one can think of them as a snapshot of stochastic standing waves. The physics governing them is fairly simple and thus one can see how they encode extractable information about the cosmological parameters. The empirical emergence of a coherent series of acoustic peaks and troughs is one of the great triumphs of modern cosmology. This picture has received additional experimental confirmation with the detection by the Sloan Digital Sky Survey (SDSS) in the power spectrum of the galaxy distribution at low redshifts of an imprint of the acoustic oscillations [75] as seen in Figure2.2. The Sloan team analyzed the clustering of galaxies in the survey by calculating the two-point correlation function of the data. This correlation function is a function of the comoving galaxy separation distance and describes the probability that one galaxy will be found within a given distance of another. The baryonic acoustic oscillation signal would show up as a bump in the correlation function at a comoving separation equal to the sound horizon.

The Damping Tail ($l \gtrsim 1000$):

Recombination was not an instantaneous process and as such there is a thickness to the last scattering surface. Thus on scales smaller than that subtended by this thickness, corresponding to the highest ls, the anisotropies are damped. We can also think of the photon-baryon fluid as having an imperfect coupling which results in a diffusion between the two components. This

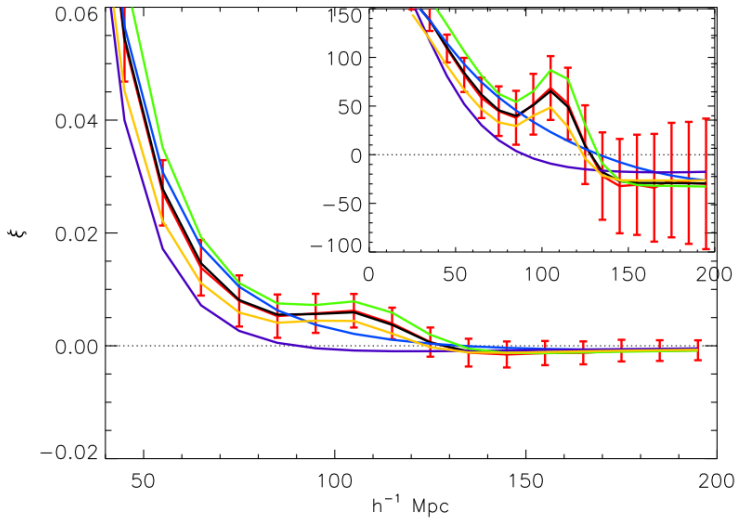

Figure 2.2: **Large-scale correlation function of the SDSS LRG sample:** The solid lines represent models with different values of $\Omega_m h^2 = 0$ (magenta) 0.12 (green), 0.13 (red), and 0.14 (blue).

leads to a decrease in the amplitudes of the oscillations with time. These effects lead to a damping of the C_l's, sometimes called Silk damping [23], which cuts off the anisotropies at multipoles above about 2000. Gravitational lensing, caused mainly by non-linear structures at low redshift have an extra effect for high l's. The C_l's are convolved with a smoothing function, partially flattening the peaks, generating a power-law tail at the highest multipoles and complicating the polarization signal [76]. This is an example of a secondary effect, which is the processing of anisotropies due to relatively nearby structures. Galaxies and galaxy clusters give several of these effects but all are expected to be of low amplitude and are typically only important for high multipoles.

2.5 Large Scale Structure

The final observational pillar lending to support to the Big Bang model is that of the observed large scale structure of the universe. It is generally accepted from observations and theoretical predictions that the first quasars and galaxies formed roughly a billion years after the Big Bang

and larger structures such as galaxy clusters and superclusters have been forming and evolving since. The stark differences between early galaxies and those which have formed more recently provide a very strong argument against the steady state model of the Universe. Furthermore, Big Bang simulations have made extremely successful predictions about the large scale structure formation [77] that tie in with observations of star formation and galaxy and quasar distributions. Another important note to make is the correlation between the large scale structure and the gravitation lensing potential which we shall see later on. Here we will skip over most of the mathematical detail and discuss only a few key ideas.

In the previous section, we discussed the fate of the radiation left over from the decoupling of matter and radiation in the Cosmic Microwave Background. We now turn our attention to the fate of the matter. Perturbations to the density of the baryons can only begin to grow once the matter has decoupled from radiation at recombination, which takes place after the matter-radiation equality. However, dark matter particles are collisionless and thus perturbations to their density can start growing immediately after equipartition. After recombination, the perturbations to the baryons start to grow, driven by the gravitational potential of the dark matter.

2.5.1 Density Perturbations

The Universe appears to be homogeneous only on extremely large scales. On smaller scales, the universe that we observe is actually rather lumpy and the homogeneity is broken down by structures such as stars, galaxies, galaxy clusters and voids. In cosmology, inhomogeneities grow due to the strictly attractive nature of gravity, an implication of which is that at early times they were much smaller than they are today and any structure that we see today must have developed from a primordial seed. As a result, it is possible to treat the inhomogeneities as linear perturbations for much of their evolution. This linear treatment is quite adequate to describe the fluctuations in the CMB at the time of last scattering. For this reason, the CMB is currently the best tool we have to probe the primordial inhomogeneities, providing further motivation for its study and improving observations. The angular scale subtended by the primordial seeds corresponding to the largest cosmic structure known is of the order of 3 degrees, corresponding to CMB multipoles of $l \approx 20$.

Much of the interesting physics of density fluctuations can be found by a Newtonian linear perturbation analysis in which small perturbations grow slowly over time, following the expansion of the background in which they exist until they become large enough to decouple from it and collapse into systems which are gravitationally bound. If the perturbations are small enough, the can be decomposed into Fourier components that evolve independently of one another and can be treated separately.

Generally, the approach taken when dealing with density perturbations is to make use of a non-relativistic and linear treatment of perturbation theory. By doing this, we can extract much of the relevant physics without having to solving the full equations of general relativity. For more details see [78].

2.5.2 Structure formation

In order for tiny density fluctuations to grow to galactic size, there must be enough time or the expansion must be brief and exponential. In the Friedmann-Lemaître-Robertson-Walker (FLRW) universe, the expansion is too slow to produce the observed universe in the available time. This problem is solved by cosmic inflation, a different mechanism which gives the necessary exponential growth [7]. Only after inflation ends does the Universe enter the regime of Friedmann expansion. During this time, Hubble radius gradually overtakes the inflated regions and the inflationary perturbations cross back into vision with a wavelength corresponding to the size of the Hubble radius at that time.

During the period of radiation domination, any growth of perturbations is suppressed. Once the matter domination era begins, the perturbations can start to grow. Dark matter plays a hugely important role in the formation of structure in the Universe, due to the fact that it interacts only by the force of gravity. This allows perturbations to the dark matter distribution to grow and become halos while the ordinary baryonic matter perturbations are suppressed by the radiation pressure. The dark matter halos create potential wells into which the baryons can fall after recombination. A Universe containing no dark matter would require a significantly longer time frame in which to form the structures in the Universe that we observe today. When the perturbations have grown

significantly, small regions may have become substantially more dense that the surrounding Universe. Once this happens the physics becomes considerably more complicated and we shall not enter into the details here. The results from N-body simulations predict that the Universe is made up largely of extremely underdense voids with the matter collecting along filaments and halos, having a web-like structure [77]. The galaxies, clusters and super clusters form in these regions. The simulations agree to a large extent with current observations with a few, as yet, completely unresolved problems such as the galaxy bias. Attempts to solve this problem have suggested that it can be accounted for in the complicated physics of galaxy formation or that there is a problem with the current model of cold dark matter and that a hot dark matter model would prevent the growth of the smallest halos. The large-scale structure of the Universe has been mapped by SDSS out to a redshift $z = 0.14$ shown in Figure (2.3).

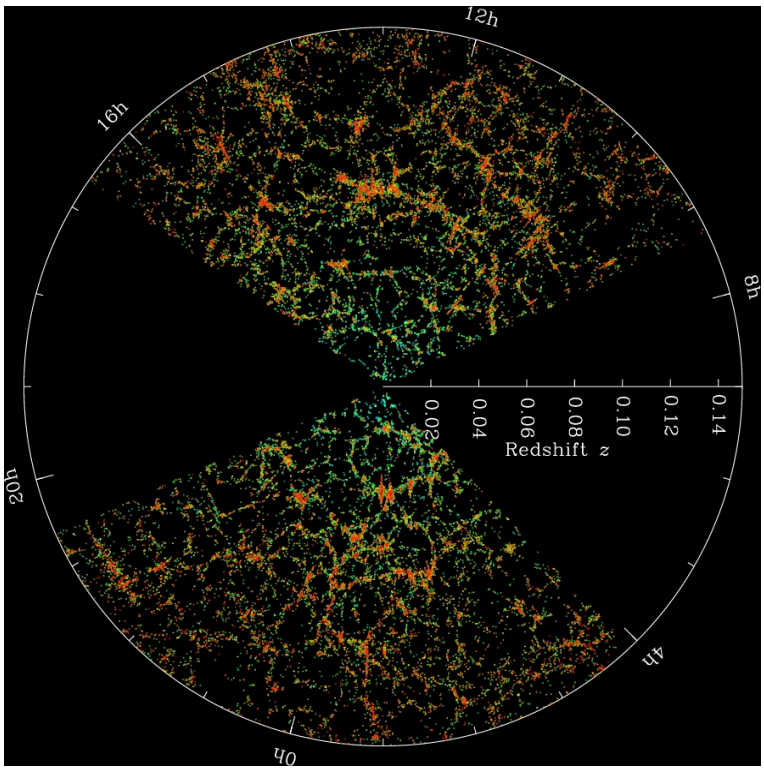

Figure 2.3: **Large-scale structure of the Universe:** The map obtained by SDSS shows the large-scale structure of the Universe and agrees well with simulations that predict that the Universe is made up of underdense voids with matter collecting along filaments and halos.

CHAPTER 3

Gravitational Lensing

Before proceeding further, we briefly summarize the development of the gravitational lensing theory. The idea that a ray of light can be bent due to gravitational attraction as it passes by a massive object is not new and was even considered by Newton as far back as 1704 in his book, Opticks [79], where in what is widely regarded as one of the greatest works in science history, he dealt with amongst other subjects, the refraction of light. About a century after Newton's publication, Soldner investigated the change in the angular position of stars due to the deflection of light. He computed the hyperbolic orbit of a body moving with constant velocity passing by a spherical mass. By making use of the assumption that light behaves as a stream of particles and employing the Newtonian theory he concluded that a light ray grazing the surface of the sun would be deflected by 0.87 arcseconds [80]. A further century later Einstein arrived at the same result as Soldner independently, calculating the deflection angle from the principle of equivalence and using a Euclidean spatial metric that was unaffected by gravity [81]. Finally, after the formulation of General Relativty, a metric theory of gravity, providing a unified description of space and time as a four-dimensional manifold called spacetime, Einstein obtained a deflection angle of 1.75 arcseconds; twice the Newtonian value [82]. This result was spectacularly confirmed by Dyson, Eddington and Davidson [83] during a total solar eclipse. Along with the observed precession of

Mercury, this confirmed Einstein's theory of general relativity and was hailed as conclusive proof of its superiority over the Newtonian model. Eddington made a further contribution by pointing out that very massive or compact objects could bend light rays sufficiently strongly that multiple light rays reach an observer, which, if the background object and the lens are well aligned, would produce multiple images [84]. In the case where the alignment is perfect, Chowlson predicted that a ring-shaped image would be formed centered around around the foreground object [85]. Einstein arrived at this result independently some years later and these rings are now known as Einstein rings. Einstein also realized that the apparent luminosities of the images are changed by gravitational lensing and thus an image may be magnified although he thought it unlikely that such phenomena would be observed around stars due to the low resolving power of telescopes at the time [86].

In 1933, Zwicky discovered the apparent contradiction between the visible mass of the Coma cluster and its virial mass, which could only be explained by the presence of an unseen mass, which we now call dark matter [10]. We thus needed a new independent probe of the total mass without having to make use of the light distribution and Zwicky suggested that extragalactic nebulae could be efficient gravitational lenses and provide a valuable tool for obtaining the mass of systems in the Universe. He also predicted that not only should multiple images be observable but that they should also be discovered and suggested that one could use galaxies as a giant cosmic telescope to observe objects that would otherwise be to faint or distant [87]. The following quarter of a century saw little work in the field but it was revived in the early 1960's, with work on galaxy-galaxy lensing [88], star-star lensing [89] and the first possible cosmological applications for gravitational lensing, where it was predicted that the time delays in multiple images could be used to measure the Hubble constant today [90]. In addition to this, the first calculations of light propagation though an inhomogeneous universe and the deformation of ray bundles were performed [91, 92]. Some of the applications presented in the work were particularly promising due to the recent discovery of quasars [93].

The first detection of a gravitational lensing candidate was made serendipitously in 1979 [94] when a doubly imaged quasi-stellar object (0957+561) was detected at a redshift of $z = 1.4$

and an angular separation of 6 arcseconds. The detection was confirmed by the similarity of the spectra, the ratio of optical and radio fluxes and the subsequent detection of a lensing galaxy at $z = 0.36$. Following this discovery, activity in the field of gravitational lensing both theoretically and observationally increased dramatically propelling the field to the forefront of extragalactic astronomy. In 1986, the first luminous arcs, which are identified as being highly distorted images of high-redshift galaxies, were observed in galaxy clusters[95]. A third type of gravitational lensing systems was discovered with radio telescopes in 1987 with the detection of nearly full rings [96, 97]. An example of a lensing cluster is shown in Figure (3.1). The long arcs in the image are highly deformed galaxies that have been gravitationally lensed by the cluster in the foreground.

The previous discussion deals mainly with manifestations of strong lensing which are fairly easy

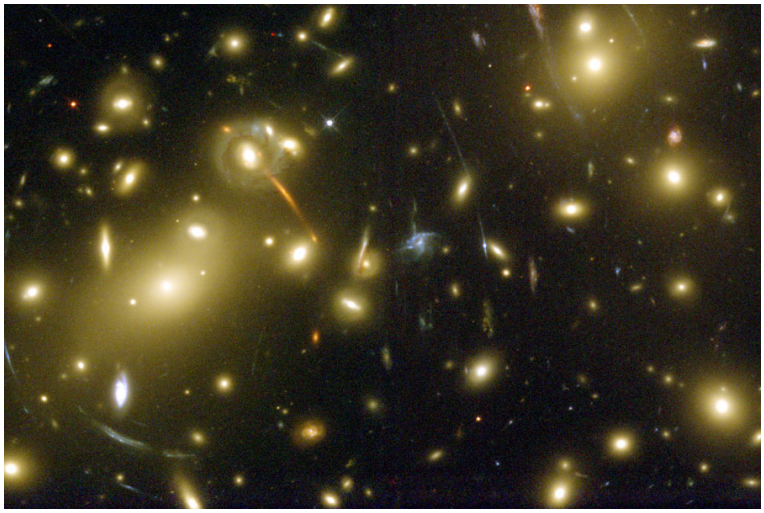

Figure 3.1: **The lensing cluster Abell 2218. Credit: Andrew Fruchter (STScI) et al., WFPC2, HST, NASA** Almost all of the bright objects in this image are galaxies in the cluster Abell 2218. The light from background galaxies is bent and focused. As a result, multiple images of these background galaxies are distorted into long faint arcs.

detect and provides a useful tool for detailed analysis of the surface mass density of the deflection object being probed. In most cases however, the light rays are only slightly deflected by gravity and the astronomical sources are only weakly distorted. Consequently, it is very difficult to de-

tect this effect in individual objects and to obtain any results one much average the net distortion over an ensemble of images. It can be assumed that the orientation of distant galaxies is random and thus any coherent alignment of the images is a sign that there is a tidal gravitational field between the source and the observer. The first such weak lensing analysis was conducted in 1990 and a coherent alignment of the ellipticities of galaxies behind Abell 1689 and CL 1409+52 was detected [98]. This provides an extremely valuable tool for the estimation of cluster masses and can accurately probe clusters containing significantly amounts of dark matter compared to baryonic matter. One can also compare the dark matter distribution with the distribution of baryons from optical and X-ray data to reveal the relation between the dark matter and stellar and gas components of the cluster, an example of which is the Bullet cluster [99]. Another manifestation of weak gravitational lensing is cosmic shear. The large-scale structure lenses background galaxies to produce an observable pattern of alignments. This distortion is very small compared to the lensing effect cause by clusters. The ability to probe the matter density distribution of the large-scale structure makes weak lensing a powerful probe of cosmological parameters especially when combined with other observations such as the cosmic microwave background, supernovae and galaxy surveys. The first detection of lensing by the large-scale structure was made in 2000 and the observations have place competitive constraints on cosmological parameters such as the dark matter density and power spectrum amplitude [100, 101, 102]. More recently, weak lensing has been used in the detection of a large-scale filament funneling matter onto the core of the massive galaxy cluster MACSJ0717.5+3745 [103].

The propagation of light in an arbitrary spacetime is generally a rather difficult problem to solve. In most astrophysically relevant situations, where the dimension of the objects causing the lensing is very small compared to the distance between the observer and the source, it is possible to make use of approximate descriptions for light deflections known as the gravitational lens theory the details of which are explained in detail in [104]. This theory assumes that the size of the lens along the line of sight is small compared to the distance between the observer and the lens, and the lens and the source. However, this approach fails when one considers a mass distribution that extends to cosmic scales along the line of sight. We must thus take a more general and rigorous

approach in our description of light propagation.

3.1 Weak Cosmological Lensing

In this thesis, the interest lies in developing tools to analyze the effects that the large-scale structure of the Universe has on the temperature anisotropy of the CMB. We must therefore study the impact of small density perturbations on the propagation of light in an isotropic and homogeneous Friedmann-Lemaître (FL) universe. We assume that the perturbations have small and slowly varying Newtonian potentials, which is valid for cosmological situations where typical velocities in galaxy clusters are $\sim 10^3$ km/s $\ll c$ and typical Newtonian potentials are $\sim 10^{-5}c^2$.

3.1.1 Propagation of Light in a Perturbed Minkowski Space

We begin our discussion of gravitational lensing by examining the effect of gravity on a photon passing nearby a source of lensing in the Newtonian approximation and in a homogenous and flat Minkowski universe to build up an intuitive idea of the processes involved in gravitational lensing. We then proceed to a more relevant discussion relating to the work presented in this thesis and present the theory for gravitational lensing for the more general case of a perturbed FL universe.

Lensing by an Individual Perturbation

For most of the relevant applications for gravitational lensing we can assume that the geometry is described to a good approximation by the Friedmann-Lemaître-Robertson-Walker (FLRW) metric where the inhomogeneities are considered to be local perturbations to the metric. We can this split the trajectory of a ray of light into three distinct parts:

1. The light propagates through a flat, unperturbed spacetime from the source to the lens,
2. The trajectory is modified near the lens due to the gravitational potential,
3. The light ray again travels though unperturbed spacetime from the lens to the observer.

We assume that the region around the lens can be described by a flat Minkowski spacetime with small perturbations induced by the gravitational potential of the lens. This is valid so long as the Newtonian potential is small ($\Psi << c^2$) and the peculiar velocity of the lens is negligible compared to the speed of light c. Fortunately, these conditions are met in most astrophysically relevant situations, an exception being for light passing near a black hole. Using these simplifications one can describe light propagation near a lens in a flat spacetime, with a perturbation due to the gravitational potential of the lens described in a first order, post Newtonian approximation.

In addition to the assumption of weak gravitational fields, we assume that the perturbations to the density are localized. Linearizing the gravitational field equations and taking non-relativistic sources allows us to obtain the post-Minkowskian metric to first order,

$$ds^2 = \left(1 + \frac{2\Psi}{c^2}\right) c^2 dt^2 - \left(1 - \frac{2\Psi}{c^2}\right) d\mathbf{r}^2, \tag{3.1.1}$$

where $\mathbf{r}$ is the spatial part of the Minkowski metric. We can make use of the fact that light travels along null geodesics, $ds^2 = 0$, to obtain the effective velocity of light v when it passes through a weak gravitational field. The time that a light ray would need to travel from point A to B in the gravitational field is given by

$$T = \int_A^B dt = \frac{1}{c}\int_A^B \frac{c}{v}\frac{dl}{dt} = \frac{1}{c}\int_A^B n\, dl, \tag{3.1.2}$$

where the effect of spacetime curvature on the light trajectory can be described as an effective refraction index given by

$$n = 1 - \frac{2}{c^2}\Psi = 1 + \frac{2}{c^2}|\Psi|, \tag{3.1.3}$$

and the Newtonian potential is negative and vanishes asymptotically. The refraction index $n > 1$ means that light travels with a speed lower than c and the effective speed of light in a gravitational field is given by

$$v = \frac{c}{n} \simeq c - \frac{2}{c}|\Psi|. \tag{3.1.4}$$

The optical path length of a light ray from A to B is defined by

$$L = \int_A^B n\, dl. \tag{3.1.5}$$

In the context of variational calculus, Fermat's principle can be expressed as

$$\delta \int_A^B n \, dl = \delta \int_A^B n(\mathbf{r}) \sqrt{|\dot{\mathbf{r}}|} d\lambda = 0, \tag{3.1.6}$$

where the different curves are parametrized by the affine parameter λ and the overdot denotes a derivative with respect to λ. We choose λ such that it passes through an observer O, having a four-velocity u_O^μ, satisfying $u_O^\mu u_{O\mu} = 1$. The physical wavevector k^μ of a photon depends on the frequency of the light and so we define a dimensionless wave vector, independent of the frequency ω_0 of the light measured by the observer, as $\tilde{k}^\mu \equiv -c\omega^{-1}k^\mu$. Furthermore, $\lambda = 0$ at O, it increases backward along the light cone and satisfies $u_O^\mu \tilde{k}_\mu = -1$ at O. Following from the properties of λ we note that $\tilde{k} = dx^\mu/d\lambda$ and that λ measures the proper distance along the light ray. Making use of the Euler-Lagrange equations this can be written as

$$\ddot{\mathbf{r}} = -\frac{2}{c^2} \boldsymbol{\nabla}_\perp \Psi(\mathbf{r}), \tag{3.1.7}$$

where $\boldsymbol{\nabla}_\perp \Psi(\mathbf{r})$ is the gradient of the potential in the plane perpendicular to the perturbed light ray. The total deflection caused by the potential is defined by the integral of the differential displacements along the path taken by the light ray,

$$\boldsymbol{\alpha}(\mathbf{r}) = -\int \boldsymbol{\nabla}_\perp n(\mathbf{r}) = \frac{2}{c^2} \int \boldsymbol{\nabla}_\perp \Psi(\mathbf{r}) \, dl. \tag{3.1.8}$$

The deflection angle in nearly all astrophysically relevant situations is small and as such we usually make use of the Born approximation and evaluate the integral along the unperturbed ray. From Equation (3.1.7) is is easy to show that the physical separation transverse to the direction of the light $\boldsymbol{\xi}$ is given by

$$\frac{d^2\boldsymbol{\xi}}{d\lambda^2} = -\frac{2}{c^2} \boldsymbol{\nabla}_\perp \Psi(\boldsymbol{\xi}, \lambda) \tag{3.1.9}$$

3.1.2 Propagation of Light in a Friedmann-Lemaitre Universe

Light propagation though an unperturbed FL universe

We now consider the propagation of light through and unperturbed background FL universe. We wish to calculate the separation between two neighbouring light rays in a direction transverse to

the line of sight, which is described by the two-dimensional vector $\boldsymbol{\xi}$.

In a non-flat spacetime, one cannot represent the reference light ray by a straight line. We rather choose an arbitrary fiducial light ray as a reference. We define $\boldsymbol{\theta}$ to be the angle between a ray and the fiducial ray, whose propagation is determined by the geodesic equation [104]. Assuming a sufficiently small $|\boldsymbol{\theta}|$ so that we can work in the linear regime it can be shown that

$$\boldsymbol{\xi}(\lambda) = \mathcal{D}(\lambda)\boldsymbol{\theta}. \tag{3.1.10}$$

The choice of λ ensures that at $\lambda = 0$ we have $d\boldsymbol{\xi}/d\lambda = \boldsymbol{\theta}$. The 2×2 matrix $\mathcal{D}$ satisfies the Jacobi equation

$$\frac{d^2\mathcal{D}(\lambda)}{d\lambda^2} = \mathcal{T}\mathcal{D}(\lambda), \tag{3.1.11}$$

with the initial conditions

$$\mathcal{D}(0) = \mathcal{O} \qquad \text{and} \qquad \left.\frac{d\mathcal{D}}{d\lambda}\right|_{\lambda=0} = \mathcal{I}. \tag{3.1.12}$$

The optical tidal matrix $\mathcal{T}$ is related to the curvature of the metric and is the source of the convergence, resulting in an isotropic focusing of a light bundle maintaining the original shape, and shear, which causes and anisotropic focusing effect thus changing the shape of the light bundle.

Equation (3.1.11) implies that $\boldsymbol{\xi}$ is given by

$$\frac{d^2\boldsymbol{\xi}}{d\lambda^2} = \mathcal{T}\boldsymbol{\xi} \tag{3.1.13}$$

It becomes convenient here to rather continue this discussion in terms of comoving distances. To do this, we need a relation between the affine parameter λ and the radial coordinate χ. Since λ gives the proper distance of the photon path, $d\lambda = -acdt$. Making use of the fact that photons travel along null geodesics we have $cdt = -ad\chi$, yielding

$$d\lambda = a^2 d\chi. \tag{3.1.14}$$

We can thus introduce the comoving separation $\mathbf{x} = a^{-1}\boldsymbol{\xi}$ which leaves the propagation equation in the simple form

$$\frac{d^2\mathbf{x}}{d\chi^2} + K\mathbf{x} = 0, \tag{3.1.15}$$

where K is the spatial curvature. This equation can be solved fairly easily by making use of the boundary conditions

$$\mathbf{x} = \mathbf{0} \qquad \text{and} \qquad \frac{d\mathbf{x}}{d\chi} = \boldsymbol{\theta}, \tag{3.1.16}$$

at $\chi = 0$. The solution is the given by

$$\mathbf{x}(\boldsymbol{\theta}, \chi) = f_K(\chi)\boldsymbol{\theta}, \tag{3.1.17}$$

where $f_K(\chi)$ is given in Equation (2.2.16). Equation (3.1.15) has the form of an oscillator equation hence the solutions are trigonometric or hyperbolic if K is positive or negative. Should $K = 0$, implying spatial flatness, the comoving separation between the light rays is a linear function of distance.

Light propagation through Large-Scale Structure Inhomogeneities

We now generalize the description of light propagation to an expanding, non-flat FL universe with large-scale mass fluctuations included. We interpret $\mathbf{x}$ as the comoving separation between an arbitrarily chosen fiducial ray and a nearby neighbouring ray. A modified version of Equation (3.1.9) should thus rather contain the difference of the perpendicular potential gradients $\nabla^2(\boldsymbol{\nabla}_\perp \Psi)$ between the two light rays to account for the deflection relative to one another. Taking this into account and including the cosmological contribution from Equation (3.1.15) leads to the propagation equation

$$\frac{d^2\mathbf{x}}{d\chi^2} + K\mathbf{x} = \frac{2}{c^2}\nabla^2 \left\{\boldsymbol{\nabla}_\perp \Psi[\mathbf{x}(\boldsymbol{\theta}, \chi), \chi]\right\}. \tag{3.1.18}$$

In reality, the comoving distance is changed in the presence of density perturbations but here we assume that the global properties of the weakly perturbed FL models remain the same as in the homogenous and isotropic case. With this assumption, χ remains the same as in the unperturbed model. We can solve this equation with the boundary conditions given in Equation (3.1.16). The first of these conditions implies that the two light rays start at the same point and the second that they head off in directions differing by $\boldsymbol{\theta}$. The comoving separation between two light rays is then the sum of the homogeneous solution given in Equation (3.1.17) and its convolution with

the inhomogeneous source term

$$\mathbf{x}(\boldsymbol{\theta},\chi) = f_K(\chi)\boldsymbol{\theta} - \frac{2}{c^2}\int_0^\chi d\chi'\, f_K(\chi-\chi')\nabla^2\left\{\boldsymbol{\nabla}_\perp\Psi[\mathbf{x}(\boldsymbol{\theta},\chi'),\chi']\right\}, \tag{3.1.19}$$

where the integral is along the actual photon paths of the two light rays. The exact form of the solution is thus very complicated. We can simplify the solution by making the assumption that the change of $\mathbf{x}$ for perturbed rays is small compared with that of unperturbed rays. This allows us to make use of an equivalent of the Born approximation for small-angle scattering. So if

$$\frac{|\mathbf{x}(\boldsymbol{\theta},\chi') - f_K(\chi')\boldsymbol{\theta}|}{|f_K(\chi')\boldsymbol{\theta}|} \ll 1, \tag{3.1.20}$$

we can replace $\mathbf{x}(\boldsymbol{\theta},\chi')$ by $f_K(\chi')\boldsymbol{\theta}$ which simplifies the integrand. We can now calculate the deflection angle $\boldsymbol{\alpha}$ at a comoving distance χ as the difference between the comoving separation of two rays of light propagating through an unperturbed spacetime, given by Equation (3.1.17) as $f_K(\chi)\boldsymbol{\theta}$, and the comoving separation between two lights rays propagating though perturbed space, divided by the angular diameter distance to χ,

$$\boldsymbol{\alpha}(\boldsymbol{\theta},\chi) = \frac{f_K(\chi)\boldsymbol{\theta} - \mathbf{x}(\boldsymbol{\theta},\chi)}{f_K(\chi)} = \frac{2}{c^2}\int_0^\chi d\chi'\,\frac{f_K(\chi-\chi')}{f_K(\chi)}\boldsymbol{\nabla}_\perp\Psi[f_K(\chi')\boldsymbol{\theta},\chi']. \tag{3.1.21}$$

It is important to realize that this is the deflection angle relative to a nearby fiducial ray. It is not possible to measure absolute deflection angles. The only measurable effects of light deflection depend on the derivatives of the deflection angle.

3.2 The Lensing Potential and Convergence

As seen in Equation (3.1.21) the total deflection angle is given in terms of the integrated gradient of a potential. We can change the order of operations and make the substitution $\boldsymbol{\nabla}_{\boldsymbol{\theta}} = f_K(\chi)\boldsymbol{\nabla}_\perp$ to define the lensing potential, an effective integrated potential which can be used in the calculation of the effects of weak lensing on the CMB anisotropies. We see that the deflection angle can be written as a gradient

$$\boldsymbol{\alpha}(\boldsymbol{\theta}) = \boldsymbol{\nabla}_{\boldsymbol{\theta}}\psi(\boldsymbol{\theta}), \tag{3.2.22}$$

of the projected potential

$$\psi(\boldsymbol{\theta}) \equiv \int_0^{\chi} d\chi' W_{\psi}(\chi') \Psi(f_K(\chi')\boldsymbol{\theta}, \chi'). \tag{3.2.23}$$

This projected potential is know as the lensing potential and the weight function

$$W_{\psi}(\chi') = \frac{f_K(\chi - \chi')}{f_K(\chi) f_K(\chi')}, \tag{3.2.24}$$

is sometimes referred to as the lensing efficiency.

We can approximate recombination as having been instantaneous and so we can describe the CMB by a single source plane. We tend to neglect the effects of sources only appearing later, including reionization and thus a single two-dimensional map of the lensing potential on the sphere contains all the information required. The lensing potential will remain Gaussian on scales where the potential Ψ is Gaussian. On smaller scales non-linear evolution could introduce non-Gaussianities even if the primordial fields are Gaussian but this is only a small correction and we will not discuss it further.

Moving on, we discuss the relation between the the potential and the matter distribution of the Universe through the Einstein equations. The gravitational potential of localized perturbations to the density which are very much smaller than the horizon size and have peculiar velocities $v \ll c$ obeys the Poisson equation

$$\nabla_r^2 \Psi' = 4\pi G \rho, \tag{3.2.25}$$

where ρ gives the total matter density and Ψ' is the sum of the smooth background $\bar{\Psi}$ and the potential of the perturbation Ψ. The total matter density is given by $\rho = (1 + \delta)\bar{\rho}$, where $\bar{\rho}$ is the background density and $\delta = \delta\rho/\bar{\rho}$ is the density contrast. The Laplacian ∇^2 acts on the physical coordinates. We can subtract the contribution of the smooth background since the Poisson equation is linear and rewrite the Laplacian in comoving coordinates, $\nabla_x^2 = a^2 \nabla_r^2$ which leaves the Poisson equation as

$$\nabla_x^2 \Psi(\mathbf{x}) = 4\pi G a^2 \bar{\rho} \delta = \frac{3H_0^2}{2a} \Omega_m \delta. \tag{3.2.26}$$

Here we have used the fact that in the matter dominated epoch $\bar{\rho} = a^{-3}\rho_0$.

So we see that the density of the perturbations is closely related to the second derivative of the potential. Thus we define the convergence as such,

$$\kappa(\boldsymbol{\theta},\chi) \equiv \frac{1}{2}\boldsymbol{\nabla}_{\boldsymbol{\theta}}\cdot\boldsymbol{\alpha}(\boldsymbol{\theta},\chi) \tag{3.2.27}$$

$$= \frac{1}{c^2}\int_0^{\chi} d\chi' \, \frac{f_K(\chi-\chi')f_K(\chi')}{f_K(\chi)}\nabla_x^{2,(2)}\Psi(f_K(\chi')\boldsymbol{\theta},\chi') \tag{3.2.28}$$

$$= \frac{1}{2}\nabla_x^2\psi \tag{3.2.29}$$

The convergence defined above contains the two-dimensional Laplacian of the lensing potential and causes an isotropic focusing of light rays and an isotropic magnification of the source. Convergence alone does not change the shape of the object or patch on the sky being lensed. We can extend it to include $\partial^2\Psi/\partial\chi$ which only involves derivatives along the actual light path because these average to zero in the limit we are working. We can thus replace the Laplacian of the potential with the density contrast via the Poisson equation (3.2.25) and find for the convergence

$$\kappa(\boldsymbol{\theta},\chi) = \frac{3H_0^2\Omega_0}{2c^2}\int_0^{\chi} d\chi' \, \frac{f_K(\chi-\chi')f_K(\chi')}{f_K(\chi)}\frac{\delta(f_K(\chi')\boldsymbol{\theta},\chi')}{a(\chi')} \tag{3.2.30}$$

So we see that the lensing convergence is directly related to the density contrast. Although a full reconstruction of the lensing convergence would be an extremely powerful tool for probing the large-scale structure of the Universe, for some purposes an estimation of the lensing convergence power spectrum is sufficient.

3.2.1 Power Spectrum of the Lensing Convergence

The statistical properties of the convergence, most importantly the power spectrum $C^{\kappa}(l)$ contain a great deal of information about the lensing field. Before continuing however, it will be useful to discuss the definitions of correlation functions and power spectra in a general sense before applying the equations to the convergence.

Statistical Preliminaries

If we consider a random n-dimensional field $g(\mathbf{x})$ with a vanishing expectation value everywhere in space, $\langle g(\mathbf{x})\rangle = 0$, and statistically invariant under arbitrary rotations and translations in space,

the auto-correlation function is given by

$$\langle g(\mathbf{x})g^*(\mathbf{y})\rangle = \xi_{gg}(|\mathbf{x}-\mathbf{y}|), \tag{3.2.31}$$

which depends only on the absolute value of the difference between $\mathbf{x}$ and $\mathbf{y}$. The Fourier transform is defined by

$$g(\mathbf{x}) = \int \frac{d^n k}{(2\pi)^n} g(\mathbf{k}) e^{-i\mathbf{x}\cdot\mathbf{k}} \qquad \text{and} \qquad g(\mathbf{k}) = \int d^n x g(\mathbf{x}) e^{i\mathbf{x}\cdot\mathbf{k}}, \tag{3.2.32}$$

and using this definition in the auto-correlation function leads to

$$\langle g(\mathbf{k})g^*(\mathbf{k}')\rangle = \int d^n x\; e^{i\mathbf{x}\cdot\mathbf{k}} \int d^n x'\; e^{i\mathbf{x}'\cdot\mathbf{k}'} \langle g(\mathbf{x})g^*(\mathbf{x}')\rangle \tag{3.2.33}$$

which reduces to

$$\langle g(\mathbf{k})g^*(\mathbf{k}')\rangle = (2\pi)^n \delta_D(\mathbf{k}-\mathbf{k}') P_g(k), \tag{3.2.34}$$

where we have introduced the Dirac delta distibution

$$\delta_D(\mathbf{k}-\mathbf{k}') = \frac{1}{(2\pi)^n} \int d^n x\; e^{i\mathbf{x}\cdot(\mathbf{k}-\mathbf{k}')}. \tag{3.2.35}$$

So we see that the power spectrum of an isotropic and homogeneous random field is just the Fourier transform of the auto-correlation function

$$P_g(k) \equiv \int d^n x\; e^{-i\mathbf{x}\cdot\mathbf{k}} \xi_{gg}(\mathbf{x}). \tag{3.2.36}$$

Power spectrum of the Convergence from the Limber Approximation

The convergence however is constrained to two dimensions on the sphere whereas the density perturbations occupy space in three dimensions. Thus, we derive a relation between the power spectrum of the density contrast $\delta(f_K(\chi)\boldsymbol{\theta}, \chi)$ and its projection onto two dimensions. We are able to define a local comoving Cartesian coordinate system by χ and $f_K(\chi)\boldsymbol{\theta}$. Now, δ can be projected along the past light cone of the observer at $\chi = 0$ to the source at χ_s by

$$\kappa(\boldsymbol{\theta}) = \int_0^{\chi_s} d\chi\; q(\chi)\delta(f_K(\chi)\boldsymbol{\theta}, \chi), \tag{3.2.37}$$

where

$$q(\chi) = \frac{3H_0^2\Omega_m}{2c^2}\frac{f_K(\chi_s-\chi)f_K(\chi)}{f_K(\chi_s)a(\chi)}, \tag{3.2.38}$$

and so the auto-correlation function is

$$\begin{aligned}\xi_{\kappa\kappa}(|\boldsymbol{\theta}-\boldsymbol{\theta}'|) &= \langle\kappa(\boldsymbol{\theta})\kappa^*(\boldsymbol{\theta})\rangle, \\ &= \int d\chi q(\chi)\int d\chi' q(\chi')\langle\delta[f_K(\chi)\boldsymbol{\theta},\chi]\delta[f_K(\chi')\boldsymbol{\theta}',\chi']\rangle. \end{aligned}\tag{3.2.39}$$

We can replace δ by its Fourier transform which on decomposing the wavevector k into a two-dimensional part perpendicular to the line of sight $\mathbf{k}_\perp$ and one component parallel to the line of sight k_3 gives

$$\begin{aligned}\xi_{\kappa\kappa}(|\boldsymbol{\theta}-\boldsymbol{\theta}'|) &= \int d\chi q(\chi)\int d\chi' q(\chi')\int\frac{d^3k}{(2\pi)^3}\int\frac{d^3k'}{(2\pi)^3} \\ &\times \langle\delta[\mathbf{k},\chi]\delta[\mathbf{k}',\chi']\rangle e^{-if_K(\chi)\mathbf{k}_\perp\cdot\boldsymbol{\theta}}e^{if_K(\chi')\mathbf{k}'_\perp\cdot\boldsymbol{\theta}'}e^{-ik_3\chi}e^{ik'_3\chi'}. \end{aligned}\tag{3.2.40}$$

We generally make the assumption that on scales larger than the coherence scale L_{coh} there is no power in the density perturbations, an implication of which is that the auto-correlation function in the previous equation vanishes for $\chi_H \gg |\chi-\chi'| \sim L_{coh}$, where χ_H is the horizon. The density contrast can be considered constant over the time taken for light to cross the comoving distance corresponding to the coherence scale and so we have that $\delta(\mathbf{k},\chi) \approx \delta(\mathbf{k},\chi')$. The density contrast is still free to evolve cosmologically. In addition to this, we must make the assumption that the weight function $q(\chi)$ has a negligible variation on the scale $|\chi-\chi'| \lesssim L_{coh}$ where the auto-correlation function does not vanish and thus we have $q(\chi) \approx q(\chi')$ and $f_K(\chi) \approx f_K(\chi')$. We can use these approximations in Equation (3.2.40) and replace the correlator with the power spectrum from Equation (3.2.34) which introduces $\delta_D(\mathbf{k}-\mathbf{k}')$ allowing for the integration over $\mathbf{k}'$ which results in

$$\xi_{\kappa\kappa}(|\boldsymbol{\theta}-\boldsymbol{\theta}'|) = \int d\chi\, q^2(\chi)\int\frac{d^3k}{(2\pi)^3}P_\delta(k,\chi)e^{-if_K(\chi)\mathbf{k}_\perp\cdot(\boldsymbol{\theta}-\boldsymbol{\theta}')}e^{-ik_3\chi}\int d\chi' e^{ik_3\chi'}. \tag{3.2.41}$$

Integrating over χ' gives $2\pi\delta_D(k_3)$ which carries the implication that only modes perpendicular to the line of sight contribute to the projected power spectrum. We can write $d^3k = d^2k_\perp dk_3$ and

make use the transformation $\Delta\boldsymbol{\theta} \equiv \boldsymbol{\theta} - \boldsymbol{\theta}' \rightarrow \boldsymbol{\theta}$ and performing the trivial integration over k_3 gives

$$\xi_{\kappa\kappa}(|\Delta\boldsymbol{\theta}|) = \int d\chi\, q^2(\chi) \int \frac{d^2k_\perp}{(2\pi)^2} P_\delta(|\mathbf{k}_\perp|, \chi) e^{-if_K(\chi)\mathbf{k}_\perp \cdot \boldsymbol{\theta}}. \tag{3.2.42}$$

Now, in order to obtain the projected power spectrum we apply Equation (3.2.36) to the above equation to get

$$\begin{aligned} C_{\kappa\kappa}(l) &= \int d^2\boldsymbol{\theta}\, \xi_{\kappa\kappa}(\boldsymbol{\theta}) e^{i\mathbf{l}\cdot\boldsymbol{\theta}}, \\ &= \int d\chi\, q^2(\chi) \int \frac{d^2k_\perp}{(2\pi)^2} P_\delta(|\mathbf{k}_\perp, \chi) e^{-i\boldsymbol{\theta}\cdot(\mathbf{l} - f_K(\chi)\mathbf{k}_\perp}, \\ &= \int d\chi q^2(\chi) \int \frac{d^2k_\perp}{(2\pi)^2} P_\delta(|\mathbf{k}_\perp, \chi) e^{-i\boldsymbol{\theta}\cdot(\mathbf{l} - f_K(\chi)\mathbf{k}_\perp}, \\ &= \int d\chi q^2(\chi) \int \frac{d^2k_\perp}{(2\pi)^2} P_\delta(|\mathbf{k}_\perp, \chi) (2\pi)^2 \delta_D\left[\mathbf{l} - f_K(\chi)\mathbf{k}_\perp\right]), \\ &= \int d\chi\, \frac{q^2(\chi)}{f_K^2(\chi)} P_\delta\left(\frac{\mathbf{l}}{f_K(\chi)}, \chi\right). \end{aligned} \tag{3.2.43}$$

This is known as the Limber approximation. Thus, on substituting back for $q(\chi)$ from Equation (3.2.38) we have the power spectrum for the convergence

$$C_{\kappa\kappa}(l) = \frac{9H_0^4\Omega_m^2}{4c^4} \int_\chi^{\chi_s} d\chi \left(\frac{f_K(\chi_s - \chi)}{f_K(\chi_s)a(\chi)}\right)^2 P_\delta\left(\frac{l}{f_K(\chi)}, \chi\right). \tag{3.2.44}$$

It is straightforward to show the relationship between statistics of the convergence κ and the effective shear γ_{eff} in Fourier space. In Fourier space, the components of the Jacobian are

$$\kappa = -\frac{1}{2}(l_1^2 + l_2^2)\Psi, \tag{3.2.45}$$

$$\gamma_1 = -\frac{1}{2}(l_1^2 - l_2^2)\Psi, \tag{3.2.46}$$

$$\gamma_2 = -l_1 l_2 \Psi. \tag{3.2.47}$$

So we see that the square of the shear equals the square of the convergence, $\gamma^2 \equiv \gamma_1^2 + \gamma_2^2 = \frac{1}{4}(l_1^2 + l_2^2)^2\Psi^2 = \kappa^2$, yielding equivalent power spectra in context of weak cosmological lensing

$$\langle \kappa(l)\kappa^*(l')\rangle = \langle \gamma(l)\gamma^*(l')\rangle, \tag{3.2.48}$$

and

$$C_\kappa(l) = C_\gamma(l). \tag{3.2.49}$$

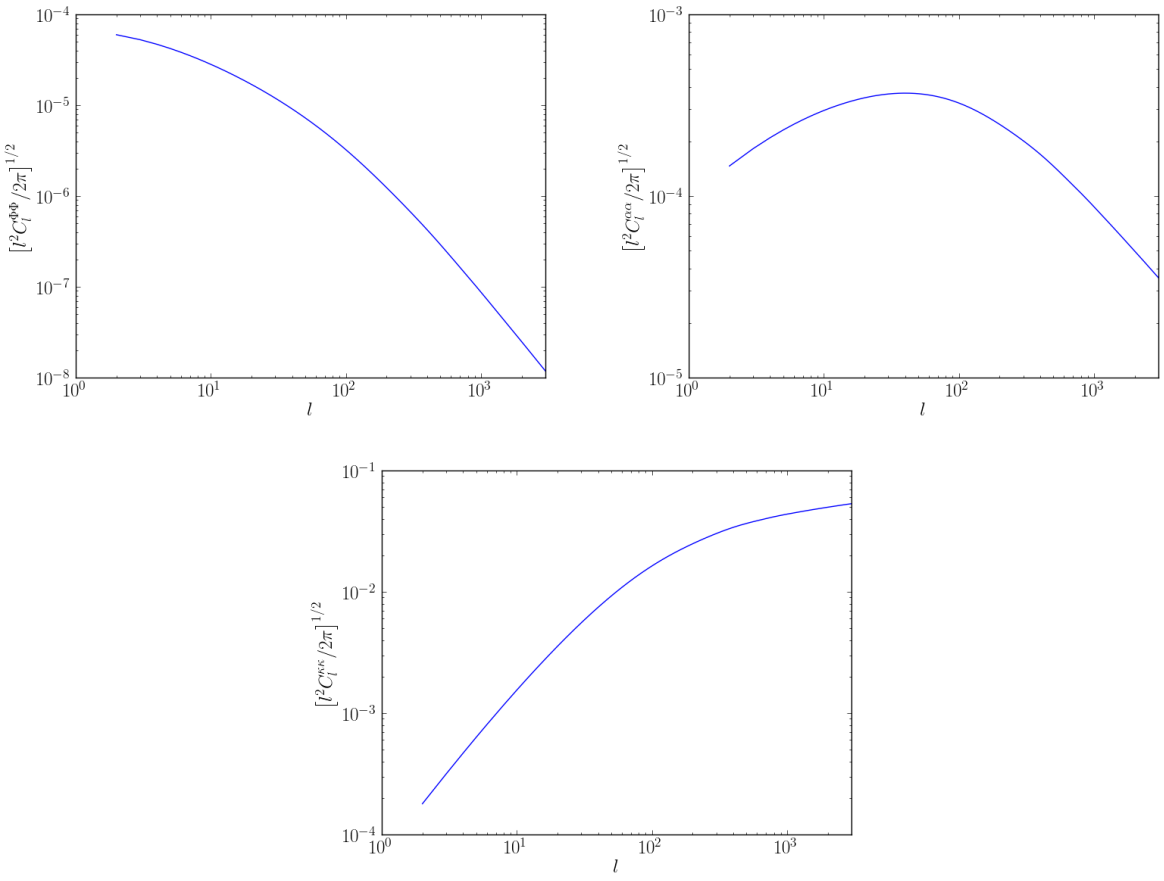

Figure 3.2: **Lensing spectrum.** The power spectrum of the lensing field expressed in three different forms as computed by `CAMB` for a typical concordance ΛCDM model. The upper left panel is the lensing potential Φ, the upper right panel is the deflection angle $\boldsymbol{\xi}$ and the lower panel is the convergence κ. The plots are related by $C_l^{\boldsymbol{\alpha}\boldsymbol{\alpha}} = l(l+1)C_l^{\Phi\Phi}$ and $C_l^{\kappa\kappa} = l^2(l+1)^2C_l^{\Phi\Phi}/4$.

Earlier we defined the convergence to be half of the divergence of the deflection angle. We can thus write the deflection angle in harmonic space as

$$\boldsymbol{\alpha}(\mathbf{l}) = \frac{2i\kappa(l)}{l^2}\mathbf{l}, \tag{3.2.50}$$

and the deflection angle power spectrum is

$$C_{\boldsymbol{\alpha}}(l) = \frac{4}{l^2}C_\kappa(l), \tag{3.2.51}$$

and similarly the power spectrum for the lensing potential is

$$C_\psi(l) = \frac{4}{l^4} C_\kappa(l). \tag{3.2.52}$$

The power spectra for the lensing potential, deflection angle and convergence are plotted in Figure (3.2).

3.2.2 Magnification and Distortion

The shape of the image and source will differ due to the differential deflection of the light bundles. Generally speaking, the shape of the image must be calculated by solving the lens equation for all the points in and extended source. The absence of absorption and emission of photons and Liouville's theorem imply that gravitational lensing conserves surface brightness. Thus, if $I^{(s)}(\boldsymbol{\beta})$ is a distribution of the surface brightness in the source plane, the observed distribution of the surface brightness in the lens plane is just given by

$$I(\boldsymbol{\theta}) = I^{(s)}[\boldsymbol{\beta}(\boldsymbol{\theta})]. \tag{3.2.53}$$

The distortion of the image can be described by the derivative of the deflection angle

$$A_{ij} = \delta_{ij} - \frac{\partial}{\partial \theta_i}\alpha_j = \begin{pmatrix} 1-\kappa-\gamma_1 & -\gamma_2 + w \\ -\gamma_2 - w & 1-\kappa+\gamma_1 \end{pmatrix}. \tag{3.2.54}$$

The shear $\gamma \equiv \gamma_1 + i\gamma_2$ determines the area preserving distortion and the antisymmetric piece w determines the rotation. If the source is much smaller than the angular scale on which the lens properties change, the lens mapping can locally be linearised. Since the deflection angle is purely a derivative of the lensing potential, the antisymmetric rotation vanishes at the lowest order. Thus, the images are distorted in shape and size. The distortion in the shape arises due to the tidal gravitational field, described by the shear γ, while the magnification arises from both isotropic focusing caused by the local matter density κ and anisotropic focusing caused by the shear.

Shear is the most important effect for galaxy lensing as it causes the galaxy ellipticities to be

correlated in a direction determined by the local shear. We can make use of it without actually knowing anything about the distribution of the source galaxies. For the CMB however, we know quite a lot about the statistical distribution of the unlensed CMB, so shearing is not the only relevant effect and we can also learn information from perturbation-scale magnifications [31]. The most simple description including shear and convergence effects on finite scales is as the remapping of points by the deflection angle. We thus usually directly discuss the deflection angle even though the shearing effect on the CMB is real and may be observed through changes to the hot and cold spot ellipticity distribution [104]

3.3 Weak Lensing of the CMB

CMB lensing theory describes the effects of the gravitational deflections of photons free-streaming through space from the surface of last scattering. The lensing signal imprinted on the CMB has a number of detectable statistical effects on the anisotropies of the CMB. In this work, we are concerned mainly with the changes to the temperature anisotropies although important consequences of lensing also arise in the context of polarization.

One can think about the large-scale structure of the Universe as being a large ensemble of point-source potential wells. An important distinction between the theory of lensing by point sources and large-scale structure is that where lensing by point sources only has power on small scales, lensing by large-scale structure has power on all scales. On very large scales, the potentials are nearly scale-invariant, but on scales well below the peak of the matter power spectrum, the potentials become small. As such, we should consider lensing by perturbations from the very largest observable scale, roughly 14 000 Mpc, down to the smallest scales of the potentials of approximately 300 Mpc. In CMB lensing, it is the smallest scale potentials that are the most important since they are far more numerous. The number of lenses interacting with a ray of light (and vice versa) also depends on the scale and naively one would expect to find $14000/300 \sim 50$ along each line of sight. The size of the deflections are set by the Newtonian potential which has a depth of roughly 2×10^{-5}. Thus the expected deflection should be of the order of $\sim 10^{-4}$.

The total r.m.s deflection should thus be $\sim 50^{1/2} \times 10^{-4} \sim 7 \times 10^{-4}$, if the lenses are taken to independent of one another. This corresponds to an angular scale of approximately 2 arcmin. The coherence scale of the deflection field, that is the angular size over which the deflection angles will be correlated, is given by the angular extent of a typical 300 Mpc potential. For a potential situated midway to the last scattering surface ie 7000 Mpc away, this would be given by $\sim 300/7000$, corresponding to an angular size of 2°.

We have shown, somewhat crudely, that a typical CMB photon traveling from the surface of last scattering to an observer is deflected by an angle of the order ~ 2 arcminutes. This corresponds roughly to an angular scale of about $l \sim 3000$ and as a result we would expect the effect of lensing to be important on these scales. Unfortunately, many foreground sources, such as quasars and radio-loud galaxies as well as dust emission, interfere with interpretations of the detected lensing signal. We can make use of the fact that the deflection angles are correlated over the sky on angular scales $\sim 2^\circ$, which corresponds approximately to the scale of the primary acoustic peaks and we expect roughly a $\sim 3\%$ broadening of the acoustic peaks. So we see that lensing has percent level effects on the spectrum of the CMB specifically on the degree sized scale of the acoustic peaks and dominates the spectrum on arcminute scales.

3.3.1 Lensing the CMB Power Spectrum

In a new age of CMB experiments, observations of the CMB temperature power spectrum are becoming increasingly accurate. We expect the anisotropies at the last scattering surface to be closely Gaussian and we can accurately compute the power spectrum C_l in linear theory. However, we observe the lensed temperature field which has a modified power spectrum and a non-Gaussian structure. We must take into account this effect to obtain accurate cosmological parameter constraints from CMB observations.

We start this section by stating two important facts concerning the effect of lensing fluctuations in the CMB. Firstly, if the CMB was completely isotropic, gravitational lensing would have no effect whatsoever as is conserves surface brightness. In this case, lensing would only magnify certain patches in the sky and demagnify other patches but since the surface brightness is in each

of the patches is unaltered, the temperature would remain unaffected. This is analogous to an observer facing an infinitely extended, homogeneously coloured wall. The observer would see some patches enlarged and other diminished but the observer would still see the same colour everywhere and would not notice any change. Secondly, it is not the absolute value of the light deflection due to lensing which matters but rather the relative deflection of neighbouring light rays. Consider a universe is which all light rays are isotropically deflected by the same arbitrary amount. The pattern of CMB anisotropies seen by an observer would then be coherently shifted relative to the intrinsic pattern but remain otherwise unchanged. It is thus merely the dispersion of deflection angles which is relevant for the impact of lensing on the observed CMB fluctuation pattern.

In this section we calculate the effect of lensing of the CMB temperature power spectrum. To start with, we describe a simple derivation of the lensed C_l using a series expansion of the lensed temperature field in the deflection angle which provides a very good understanding of the most important effects [105]. On small scales however it is not very accurate because the deflection is on the same order as the wavelength being deflected and thus a perturbative expansion in the deflection angle is not a great approximation. One should thus include a discussion of non-perturbative calculation of the lensing effect by considering the correlation function [106, 107]. To obtain an accurate result for the lensed power spectrum one must also take into account non-linear evolution and the sky curvature.

The lensed CMB temperature $\tilde{T}(\boldsymbol{\theta})$ observed in a direction $\boldsymbol{\theta}$ is given by the unlensed CMB temperature in the deflected direction $T(\boldsymbol{\theta}) = T(\boldsymbol{\theta} + \boldsymbol{\alpha}(\boldsymbol{\theta}))$. The deflection angle is small and we can thus make a Taylor expansion for the lensed CMB temperature in the deflection angle and we see that the temperature field is re-mapped according to

$$\begin{aligned} \tilde{T}(\mathbf{x}) &= T(\mathbf{x}') = T(\mathbf{x} + \nabla\psi), \\ &\approx T(\boldsymbol{\theta}) + \nabla^a\psi(\boldsymbol{\theta}) + \frac{1}{2}\nabla^a\psi(\boldsymbol{\theta})\nabla^b\psi(\boldsymbol{\theta})\nabla_a\nabla_b T(\boldsymbol{\theta}) + \dots . \end{aligned} \tag{3.3.55}$$

This is not a good approximation on all scales but it is still useful for providing a simple derivation to aid understanding and can be used to obtain qualitatively correct results for the lensed C_l. We

now introduce the Fourier transform of the lensing potential $\psi(\mathbf{l})$ and get

$$\boldsymbol{\nabla}\psi(\boldsymbol{\theta}) = i\int \frac{d^2\mathbf{l}}{2\pi}\,\mathbf{l}\,\psi(\mathbf{l})e^{i\mathbf{l}\cdot\boldsymbol{\theta}} \qquad \text{and} \qquad \boldsymbol{\nabla}T(\boldsymbol{\theta}) = i\int \frac{d^2\mathbf{l}}{2\pi}\,\mathbf{l}\,T(\mathbf{l})e^{i\mathbf{l}\cdot\boldsymbol{\theta}}. \tag{3.3.56}$$

Taking the Fourier transform of $\tilde{T}(\boldsymbol{\theta})$ and substituting into Equation (3.3.55) we get the Fourier components of ψ to the second order

$$\begin{aligned}\tilde{T(\mathbf{l})} \;&\approx\; T(\mathbf{l}) - \int \frac{d^2\mathbf{l}'}{2\pi}\mathbf{l}'\cdot(\mathbf{l}-\mathbf{l}')\psi(\mathbf{l}-\mathbf{l}')T(\mathbf{l}') \\ &\quad -\frac{1}{2}\int\frac{d^2\mathbf{l}_1}{2\pi}\int\frac{d^2\mathbf{l}_2}{2\pi}\mathbf{l}_1\cdot[\mathbf{l}_1+\mathbf{l}_2-\mathbf{l}]\,\mathbf{l}_1\cdot\mathbf{l}_2 T(\mathbf{l}_1)\psi(\mathbf{l}_2)\psi^*(\mathbf{l}_1+\mathbf{l}_2-\mathbf{l}).\end{aligned} \tag{3.3.57}$$

We are now in a position to calculate the power spectrum of the lensed temperature field $T(\boldsymbol{\theta})$ to lowest order in C_l^ψ. We neglect the correlation between the temperature and lensing potentials $\langle T(\mathbf{l})\psi(\mathbf{l})\rangle$ because at last scattering the small scale temperature is almost wholly uncorrelated with the late-time potentials responsible for the lensing. The covariance for the lensing temperature remains diagonal due to statistical isotropy, so that

$$\langle\tilde{T}(\mathbf{l})\tilde{T}^*(\mathbf{l}')\rangle = \delta(\mathbf{l}-\mathbf{l}')\tilde{C}_l^T. \tag{3.3.58}$$

At the lowest order in C_l^ψ there are contributions from the square of the first order term in $\tilde{T}$ and a cross-term from the zeroth and second order terms. Using $\psi(\mathbf{l}) = \psi^*(-\mathbf{l})$, we obtain

$$\tilde{C}_l^T \approx C_l^T + \int\frac{d^2\mathbf{l}'}{(2\pi)^2}\left[\mathbf{l}'\cdot(\mathbf{l}-\mathbf{l}')\right]^2 C^\psi_{|\mathbf{l}-\mathbf{l}'|} - C^T_{l'} - C_l^T\int\frac{d^2\mathbf{l}'}{(2\pi)^2}(\mathbf{l}\cdot\mathbf{l}')^2 C_l^\psi. \tag{3.3.59}$$

Now making a definition for the total deflection angle power

$$\langle\boldsymbol{\alpha}^2\rangle \equiv \langle|\nabla\psi|^2\rangle = \frac{1}{2\pi}\int\frac{dl}{l}l^4 C_l^\psi, \tag{3.3.60}$$

we get the final result

$$\tilde{C}_l^T \approx (1-\frac{1}{2}l^2\langle\boldsymbol{\alpha}^2\rangle)C_l^T + \int\frac{d^2}{(2\pi)^2}\left[\mathbf{l}'\cdot(\mathbf{l}-\mathbf{l}')\right]^2 C^\psi_{|\mathbf{l}-\mathbf{l}'|}C^T_{l'}. \tag{3.3.61}$$

For a typical model $\langle\boldsymbol{\alpha}^2\rangle \sim 3\times10^{-7}$, which corresponds to an rms deflection of ~ 2.7 arcmin. The integral term has the form of a convolution of the unlensed temperature spectrum and the lensing potential power spectrum. The effect this convolution has is to smooth out the main

peaks in the unlensed spectrum which is the most important qualitative effect on large scales. The effect is several percent at $l \sim 1000$. There is little power in the unlensed CMB on small scales and the convolution transfers power from large scales to small scales thus increasing the small scale power. This effect is shown plotted in Figure (3.3).

The lowest order series-expansion result is not accurate on all scales. On scales with $l \sim 2000$ the

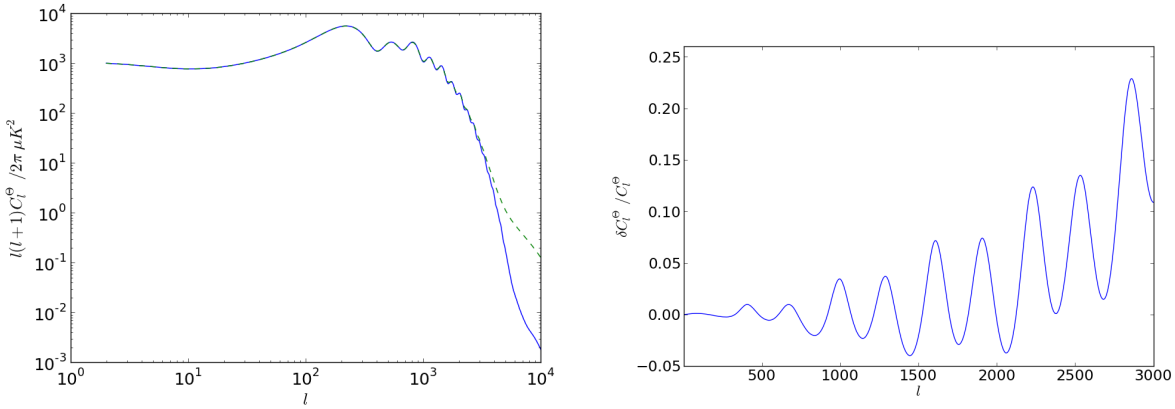

Figure 3.3: **Unlensed and lensed CMB power spectrum.** The power spectrum of the for the lensed CMB (dashed) power spectrum compared with the unlensed CMB (solid), as computed by CAMB for a typical concordance ΛCDM model. The lensing effect, which is barely noticeable on large scales smoothes out the acoustic peaks very slightly. On very small scales the lensing effect dominates the power spectrum of the observed CMB. The right panel shows the fractional change in the power spectrum induced by the lensing effect.

deflection angles are comparable to the wavelength of the unlensed fields and the Taylor series expansion is thus no longer a very good approximation. Hence we need to perform a calculation that does not rely on a series expansion. This is best done by considering the correlation function which only depends on the separation of two points and depends on neither the position nor direction and as such is invariant under displacements. The series expansion becomes accurate again on very small scales $l \gg 3000$ due to the fact that the perturbations in the unlensed spectrum are nearly wiped out by diffusion damping. The unlensed spectrum thus has very little power and can be accurately described by a single gradient term. It can be shown [31] that the lensed CMB power is thus proportional to the unlensed gradient power $R^T \equiv \frac{1}{2}\langle|\nabla T|^2\rangle$ and

to the power in the deflection angle $l^2 C_l^{\psi}$.The interpretation of this is that small scale clumps or voids in the lensing potential distort the smooth background CMB gradient by varying the deflection angle which imprint a feature on the same scale as the clump onto the observed temperature. The amplitude of this feature is proportional to both the strength of the background gradient and the size of the deflection angles. Since the imprinted feature is on the same scale as the clump, the lensed power spectrum follows the scale dependence of the deflection angle.

The series expansion result is accurate on large scales where the deflection angle is much smaller than the wavelength of the modes, and also on very small scales where the unlensed CMB has very little power and is accurately approximated by a single gradient term. In between these scales however, the series expansion result is not accurate and the non-perturbative correlation function method must be used.

CHAPTER 4

Reconstruction of the Lensing Convergence

In the previous chapter we showed that weak gravitational lensing has the effect of mapping the temperature at each point on the sky to a nearby point on the surface of last scattering. A fixed lensing potential will remap the sky to the surface of last scattering in a particular manner and one should thus be able to extract information about the lensing field by analyzing measurements of the lensing effect on a large number of CMB anisotropies. The unlensed CMB is clearly not observable and we only have access to the lensed CMB. The statistics of the unlensed CMB are, however, very well understood and statistical measurements of the lensed field should therefore provide strong constraints on the lensing potential [38, 108]. If we make the assumption that the primordial CMB is Gaussian, any non-Gaussian correlations in the CMB that we observe can in principle be used to reconstruct the lensing potential resulting from the large-scale structure of the Universe between the observer and the surface of last scattering. Further, if we assume that the deflection angle $\boldsymbol{\alpha}$, given by the gradient of the projected lensing potential $\nabla\psi$, is small we can Taylor expand the lensed temperature at any particular point on the sky in the deflection angle. In harmonic space a product of two lensed temperature maps can thus act as an estimator of the same Fourier mode of the projected lensing potential. In this way, lensing couples the temperature field at nearby points on the sky. This idea forms the basis for the reconstruction

estimators presented in this section.

In this chapter we focus on two different approaches to the reconstruction of the lensing convergence from a CMB temperature map. Firstly, we make use of the standard harmonic space quadratic estimator which was first discussed by [37] and secondly we present an alternate estimator which acts in real space and was first discussed by [39] . Throughout this analysis we assume that the primordial fields are Gaussian.

Before proceeding with the derivation and analysis of the two estimators it will be convenient to mention some potential sources of bias and variance that will have an effect on both of the estimators. The first source of variance comes from the fact that the large-scale structure in the Universe that we observe is just a single realization of a large ensemble of possible states that are allowed by theory which results in a intrinsic variance to the signal. Secondly, in the same way that the large-scale structure is just one of many possible realizations, so too is the primordial CMB. It is impossible for us to know which pattern of unlensed CMB anisotropies nature has produced. This introduces a large bias and presents us with a major hurdle to overcome in order to separate out the effects of lensing from the original anisotropies. Another source of noise is the detector noise of the instruments used in the CMB experiment.

4.1 Synthesis of the lensed CMB map

Before proceeding with the derivation and application of the reconstruction estimators, we first discuss the synthesis of the CMB temperature and lensing maps required for our simulations. The codes of M. Bucher and K. Moodley [109] were modified and extended for this purpose. The power spectra used in the creation of a realization of maps of the CMB and the lensing field are those generated by `CAMB` as shown in Figure (3.3). In all cases a square patch, 40 degrees $\times\, 40$ degrees in size, of the unlensed CMB and convergence are simulated.

To produce an unlensed CMB map, a two-dimensional random Gaussian field centered around zero and with unit variance is created and then Fourier transformed. Each point in the Fourier transformed map corresponds to a particular multipole l and is multiplied by the value of the

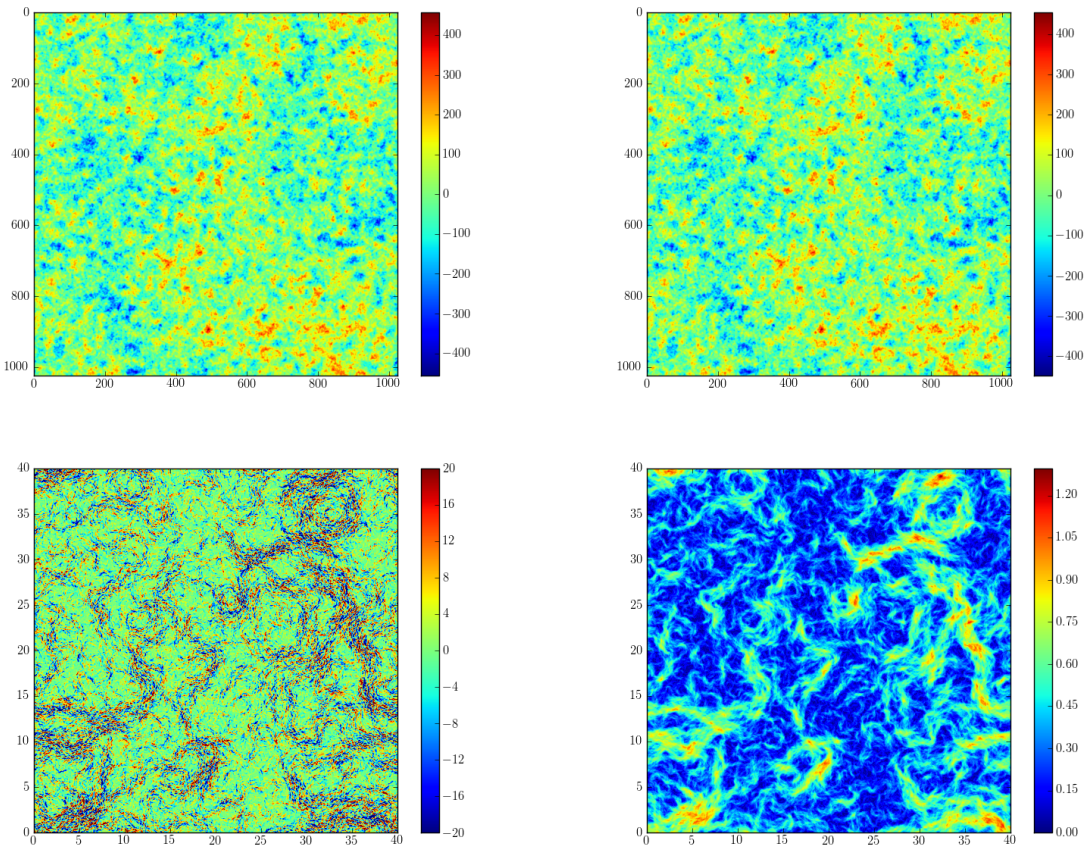

Figure 4.1: **Synthesis of unlensed and lensed CMB maps.** The top panel shows a realization of an unlensed CMB map (left) and the resultant lensed CMB (right) once a lensing field is applied. The resultant deflections are small and the distinction between the maps is not at all apparent. The bottom panel shows the difference between the lensed and unlensed fields on the left and a map of the modulus of the deflection angle on the right. It is clear that the deflection angle traces the difference between the lensed and unlensed maps.

unlensed CMB power spectrum C_l from `CAMB` for that particular l. This map is then inverse Fourier transformed back to real space and normalized by the fraction of the sky, f_{sky}, covered by the simulation and the number of pixels in the map to give the correct RMS value for the resultant unlensed temperature map $T(\boldsymbol{\theta})$. The generation of the deflection angle $\boldsymbol{\alpha}(\boldsymbol{\theta})$ field is slightly more complicated as it is a vector field requiring components $\alpha_x(\boldsymbol{\theta})$ and $\alpha_y(\boldsymbol{\theta})$ in the x and y directions such that $\boldsymbol{\alpha}(\boldsymbol{\theta}) = (\alpha_x(\boldsymbol{\theta}), \alpha_y(\boldsymbol{\theta}))$. As with the unlensed CMB temperature map,

a Fourier transformed random Gaussian field is multiplied by the value of the convergence power spectrum $\kappa(l)$ generated by CAMB for the value of l corresponding to each pixel and normalized to give the convergence map $\kappa(\boldsymbol{\theta})$. The components of the deflection angle are calculated as

$$\alpha_x(l) = \frac{l_x}{l^2}\kappa(\mathbf{l}), \tag{4.1.1}$$

$$\alpha_y(l) = \frac{l_y}{l^2}\kappa(\mathbf{l}). \tag{4.1.2}$$

The deflection angle map is returned in radians and thus in order to apply it to the unlensed CMB temperature map and to create a realization of the lensed map, one must compute an actual displacement in pixels. This is easily done by dividing the deflection angle by the angular resolution of the map. The lensed CMB map is then created by distorting the unlensed CMB so that

$$\tilde{T}(\boldsymbol{\theta}) = T(\boldsymbol{\theta} + \boldsymbol{\alpha}). \tag{4.1.3}$$

Examples of the simulated CMB maps are shown in Figure (4.1).

4.2 Harmonic space quadratic estimator

If the sky that we observe was isotropic, there would be no correlation between harmonics with different multipoles, and lensing of the CMB would not have any observable effects. Fortunately, however, the actual sky that we observe is not isotropic and we can thus make use of correlations between a number of temperature anisotropies around a particular lensing source to constrain the lensing potential of that source. We make use of the quadratic off-diagonal terms of correlation $\langle\tilde{T}(\mathbf{l})\tilde{T}(\mathbf{l}')\rangle_T$ to probe the lensing convergence of the sky that we observe.

4.2.1 Derivation of the harmonic space quadratic estimator

In deriving the harmonic space quadratic estimator, we follow the approaches of [31, 36, 110]. Note that there are several different averages that are used in this derivation and those that follow. The angle brackets $\langle\,\rangle$ denote ensemble averages over possible realizations of the primordial CMB, large-scale structure between the observer and the surface of last scattering and instrumental noise. The angle brackets $\langle\,\rangle_T$ denote an average over different realizations of the lensed CMB

where the lensing potential is kept fixed and the angle brackets $\langle\ \rangle_{LSS}$ denote an average over different realizations of the large-scale structure where the primordial CMB is kept fixed. We begin by making use of the series expansion in the deflection angle to the lowest order in the lensing potential resulting in

$$\begin{aligned}\langle\tilde{T}(\mathbf{l})\tilde{T}^*(\mathbf{l}-\mathbf{l}')\rangle_T &= \delta(\mathbf{l}')C_l^T - \int\frac{d^2\mathbf{l}''}{2\pi}[\mathbf{l}''\cdot(\mathbf{l}-\mathbf{l}'')\psi(\mathbf{l}-\mathbf{l}'')\langle T(\mathbf{l}'')T^*(\mathbf{l}-\mathbf{l}')\rangle \\ &\quad +\mathbf{l}''\cdot(\mathbf{l}-\mathbf{l}'-\mathbf{l}'')\psi^*(\mathbf{l}-\mathbf{l}'-\mathbf{l}'')\langle T(\mathbf{l})T^*(\mathbf{l}'')\rangle] + \mathcal{O}(\psi^2) \\ &= \delta(\mathbf{l}')C_l^T + \frac{1}{2\pi}\left[(\mathbf{l}'-\mathbf{l})\cdot\mathbf{l}'C^T_{|\mathbf{l}-\mathbf{l}'|} + \mathbf{l}\cdot\mathbf{l}'C_l^T\right]\psi(\mathbf{l}') + \mathcal{O}(\psi^2). \quad (4.2.4)\end{aligned}$$

We have averaged over a number of different Gaussian realizations of the unlensed temperature field T and instrument noise and it is assumed that the large-scale structure of the Universe is fixed for each realization. We only have to consider the modes greater than zero as the $l = 0$ mode of the lensing potential is not observable. It is clear that with a small amount of manipulation, taking only the linear part of the expansion the two-point correlation function takes the form

$$\langle\tilde{T}(\mathbf{l})\tilde{T}^*(\mathbf{l}-\mathbf{l}')\rangle_T = q(\mathbf{l},\mathbf{l}')\psi(\mathbf{l},\mathbf{l}'), \quad (4.2.5)$$

where

$$q(\mathbf{l},\mathbf{l}') = \mathbf{l}\cdot\mathbf{l}'C_{l'}^T + \mathbf{l}\cdot(\mathbf{l}-\mathbf{l}')C^T_{|\mathbf{l}-\mathbf{l}'|}. \quad (4.2.6)$$

Rearranging the terms in Equation (4.2.5) we see that the square of the temperature map when acted on by an appropriate filter $q(\mathbf{l},\mathbf{l}')$ can serve as an estimator for the lensing potential. We can now define the quadratic estimator as

$$\hat{\psi}(\mathbf{l}) \equiv A(\mathbf{l})\int\frac{d^2\mathbf{l}'}{(2\pi)^2}\tilde{T}(\mathbf{l}')\tilde{T}^*(\mathbf{l}'-\mathbf{l})Q(\mathbf{l},\mathbf{l}'), \quad (4.2.7)$$

where $Q(\mathbf{l},\mathbf{l}')$ are the optimal weights and the normalization is

$$A(\mathbf{l}) = \left[\int\frac{d^2\mathbf{l}'}{(2\pi)^2}q(\mathbf{l},\mathbf{l}')Q(\mathbf{l},\mathbf{l}')\right]^{-1}, \quad (4.2.8)$$

so that the estimator is unbiased at lowest order and we have

$$\langle\hat{\psi}(\mathbf{l}')\rangle_T = \psi(\mathbf{l}'). \quad (4.2.9)$$

It is preferable here to minimize the variance and so the optimal weights then become

$$Q(\mathbf{l},\mathbf{l}') = \frac{q(\mathbf{l},\mathbf{l}')}{\tilde{C}_{l'}\tilde{C}_{|\mathbf{l}-\mathbf{l}'|}}, \tag{4.2.10}$$

where $\tilde{C}_l$ is the lensed CMB power spectrum. We thus find for the optimal estimator that

$$\hat{\psi}(\mathbf{l}) = A(\mathbf{l})\int \frac{d^2\mathbf{l}'}{2\pi}\tilde{T}(\mathbf{l})\tilde{T}^*(\mathbf{l}-\mathbf{l}')\frac{1}{2}\frac{[\mathbf{l}\cdot(\mathbf{l}-\mathbf{l}')C^T_{|\mathbf{l}-\mathbf{l}'|}+\mathbf{l}\cdot\mathbf{l}'\,C^T_l]^2}{\tilde{C}_{l'}\tilde{C}_{|\mathbf{l}-\mathbf{l}'|}}, \tag{4.2.11}$$

where

$$A(\mathbf{l})^{-1} = \int \frac{d^2\mathbf{l}'}{(2\pi)^2}\frac{1}{2}\frac{[\mathbf{l}\cdot(\mathbf{l}-\mathbf{l}')C^T_{|\mathbf{l}-\mathbf{l}'|}+\mathbf{l}\cdot\mathbf{l}'\,C^T_l]^2}{\tilde{C}_{l'}.\tilde{C}_{|\mathbf{l}-\mathbf{l}'|}}. \tag{4.2.12}$$

It is straightforward to modify the optimal estimator to incorporate detector noise by replacing $\tilde{C}_{l'}$ by $\tilde{C}_{l'}+\mathcal{N}_{l'}$. The optimal estimator is then

$$\hat{\psi}(\mathbf{l}) = N(\mathbf{l})\int \frac{d^2\mathbf{l}'}{2\pi}\tilde{T}(\mathbf{l})\tilde{T}^*(\mathbf{l}-\mathbf{l}')\frac{1}{2}\frac{\mathbf{l}\cdot(\mathbf{l}-\mathbf{l}')C^T_{|\mathbf{l}-\mathbf{l}'|}+\mathbf{l}\cdot\mathbf{l}'\,C^T_l}{[\tilde{C}_{l'}+\mathcal{N}_{l'}][\tilde{C}_{|\mathbf{l}-\mathbf{l}'|}+\mathcal{N}_{|\mathbf{l}-\mathbf{l}'|}]}, \tag{4.2.13}$$

where

$$N(\mathbf{l})^{-1} = \int \frac{d^2\mathbf{l}'}{(2\pi)^2}\frac{1}{2}\frac{[\mathbf{l}\cdot(\mathbf{l}-\mathbf{l}')C^T_{|\mathbf{l}-\mathbf{l}'|}+\mathbf{l}\cdot\mathbf{l}'\,C^T_l]^2}{[\tilde{C}_{l'}+\mathcal{N}_{l'}][\tilde{C}_{|\mathbf{l}-\mathbf{l}'|}+\mathcal{N}_{|\mathbf{l}-\mathbf{l}'|}]}. \tag{4.2.14}$$

The estimator for the deflection angle $\boldsymbol{\alpha}(\boldsymbol{\theta}) = \nabla\psi(\boldsymbol{\theta})$ and the convergence $\kappa_0(\boldsymbol{\theta}) = -\nabla^2\psi(\boldsymbol{\theta})/2$ are given by the gradient and divergence in real space of $\hat{\psi}(\boldsymbol{\theta})$. In harmonic space this equates simply to $\hat{\boldsymbol{\alpha}}(\mathbf{l}) = i\mathbf{l}\hat{\psi}(\mathbf{l})$ and $\hat{\kappa}_0(\mathbf{l}) = l^2\hat{\psi}(\mathbf{l})/2$. In an ideal situation where an ensemble of realizations of the CMB are lensed by the same realization of the large-scale structure, this estimator returns an unbiased estimator for the lensing potential. In reality however, we only have access to a single realization for each lens. It is thus important for us to understand the properties of the noise inherent in lensing reconstructions.

4.2.2 Additive bias in the harmonic space estimator

For a particular realization of the lensing potential, the uncertainty in the CMB at the surface of last scattering propagates into an uncertainty in the lensing reconstruction. This uncertainty is characterized by an increase in the variance of the quadratic estimator that can contribute a bias to the lensing signal that, depending on the quality of data available from a particular experiment,

can be an order of magnitude larger than the actual lensing signal itself. We must thus determine the variance of the estimator so that this bias may be systematically removed and the lensing field accurately reconstructed.

In order to obtain the total expected variance of the quadratic estimator we must average over different realizations of the large-scale structure,

$$\begin{aligned}\langle\langle\hat{\psi}^*(\mathbf{l})\cdot\hat{\psi}(\mathbf{l}')\rangle_T - \langle\hat{\psi}^*(\mathbf{l})\rangle_T\cdot\langle\hat{\psi}(\mathbf{l}')\rangle_T\rangle_{LSS}& \\ = A(\mathbf{l})A(\mathbf{l}')\int\frac{d^2\mathbf{l}_1}{(2\pi)^2}\int\frac{d^2\mathbf{l}'_1}{(2\pi)^2}\langle T(-\mathbf{l}_1)T(-\mathbf{l}_2)T(\mathbf{l}'_1)T(\mathbf{l}'_2)\rangle Q(\mathbf{l}_1,\mathbf{l}_2)Q(\mathbf{l}'_1,\mathbf{l}'_2)& \\ -(2\pi)^2\delta_D(\mathbf{l}-\mathbf{l}')C_l^{\psi\psi},& \end{aligned} \tag{4.2.15}$$

where

$$\langle\hat{\psi}^*(\mathbf{l})\hat{\psi}(\mathbf{l}')\rangle_{LSS} = (2\pi)^2\delta_D(\mathbf{l}-\mathbf{l}')C_l^{\psi\psi}. \tag{4.2.16}$$

While averaging over the four-point correlation function, terms that are linear in the lensing field vanish. Quadratic terms in the lensing field arise as products either of two linear terms or of a zeroth- and second-order term. The average over the product produces the trispectrum, which is the connected part of the four-point correlation function. The average of the product of a zeroth- and second-order term does not have a connected part, but rather results in the total power spectrum being implicitly dependent on $C_l^{\psi\psi}$.

Thus, to zeroth-order in the lensing field,

$$\langle\langle\hat{\psi}^*(\mathbf{l})\cdot\hat{\psi}(\mathbf{l}')\rangle_T - \langle\hat{\psi}^*(\mathbf{l})\rangle_T\cdot\langle\hat{\psi}(\mathbf{l}')\rangle_T\rangle_{LSS} = (2\pi)^2\delta_D(\mathbf{l}-\mathbf{l}')N(\mathbf{l}), \tag{4.2.17}$$

where $N(\mathbf{l}) = A(\mathbf{l})$. This is the result obtained by [36] and we see that the noise properties of the harmonic space quadratic estimator are given by

$$\langle\hat{\psi}^*(\mathbf{l})\cdot\hat{\psi}(\mathbf{l}')\rangle_T = (2\pi)^2\delta_D(\mathbf{l}-\mathbf{l}')[C_l^{\psi\psi}+N(l)]. \tag{4.2.18}$$

In deriving the estimator, the filter $Q(\mathbf{l},\mathbf{l}')$ was chosen to optimize the signal-to-noise for a zeroth-order noise of this form. However, it has been shown that the first-order term in term in the lensing field that, enters through the trispectrum, can have a significant effect [34]. Including

this initial term Equation (4.2.17) becomes

$$\langle\hat{\psi}^*(\mathbf{l})\cdot\hat{\psi}(\mathbf{l}')\rangle_T = (2\pi)^2\delta_D(\mathbf{l}-\mathbf{l}')[C_l^{\psi\psi}+N(l)+N^{(1)}(l)]. \tag{4.2.19}$$

The filter $Q(\mathbf{l},\mathbf{l}')$ is then no longer optimal once this additional noise is taken into account. The noise reduction that can be obtained by re-optimizing this filter is, however, not significant and we shall not consider these higher order contributions any further. The term $N^{(1)}(l)$ involves integrals over the lensing potential power spectrum and arises from the cosmic variance in the lensing potential coupled to the unlensed CMB. Interestingly, the secondary noise $N^{(1)}(l)$ is largely unaffected by instrumental sensitivity in CMB experiments and can thus not be dramatically reduced with technological advancements. A detailed method for treating this case is discussed in [34].

A complete reconstruction of the lensing field would be an extremely useful probe of cosmology. In some cases, however, an estimation of the lensing potential power spectrum is itself a useful probe of cosmology. The lensing potential power spectrum is highly dependent on a particular model of large-scale structure formation and depends on the primordial density perturbations. It is thus a useful probe of these models and estimates of the power spectrum from real data could be extremely useful to test and distinguish between different models as well as providing constraints on cosmological parameters.

Here we follow the work of [34] because this method was used in the first detections of the weak lensing power spectrum directly from the observed CMB temperature map by ACT [42] and SPT [43]. We can construct an estimator for the lensing potential power spectrum $\hat{C}_l^{\psi\psi}$ by making use of the estimator for the lensing potential derived in the previous section and obtain

$$\hat{C}_l^{\psi\psi} = \frac{(2\pi)^2}{\mathcal{A}}\frac{1}{2\pi l\Delta l}\int_{a_l}\frac{d^2\mathbf{l}}{(2\pi)^2}\hat{\psi}(l)\cdot\hat{\psi}(-\mathbf{l}), \tag{4.2.20}$$

where $\mathcal{A}$ is the area of the sky surveyed and a_l is an annulus of radius l and width Δl. Averaging this estimator over a number of realizations of the CMB and large-scale structure gives, to zeroth-order in the lensing field,

$$\langle\hat{C}_l^{\psi\psi}\rangle = C_l^{\psi\psi}+N(l). \tag{4.2.21}$$

So we see that $\hat{C}_l^{\psi\psi}$ is indeed an estimator for the lensing potential power spectrum although it is biased. This bias is in fact exactly the same as the variance of the lensing potential quadratic estimator. This interesting point arises from the fact that there are no grounds on which to differentiate the variance with which we reconstruct $\psi(\mathbf{l})$ from the intrinsic variance $C_l^{\psi\psi}$ of the underlying distribution. We must thus subtract this bias in order to obtain an unbiased estimator.

4.2.3 Implementation of the harmonic space quadratic estimator

We begin our implementation of the quadratic estimator by noting that on small scales the unlensed temperature anisotropy is approximately a temperature gradient and that the lensed anisotropy on small scales arises from disturbances to the gradient by the deflection angle from the lensing potential. We should thus be able to write the estimator of the lensing field in terms of the small-scale filtered temperature and the temperature gradient. We thus define the following two harmonic space functions

$$F_1(\mathbf{l}) = \frac{1}{\tilde{C}_l + \mathcal{N}_l}\tilde{T}(\mathbf{l}) \tag{4.2.22}$$

$$F_2(\mathbf{l}) = \frac{C_l}{\tilde{C}_l + \mathcal{N}_l}\tilde{T}(\mathbf{l}), \tag{4.2.23}$$

where $F_1(\boldsymbol{\theta})$ is the smale-scale filtered temperature and $\nabla_{\boldsymbol{\theta}} F_2(\boldsymbol{\theta})$ encodes the temperature gradient. These functions are shown if Figure (4.2). We can now write the harmonic space estimator as a convolution of $F_1(\boldsymbol{\theta})$ and $\nabla_{\boldsymbol{\theta}} F_2(\boldsymbol{\theta})$ by substituting these two expressions into Equation (4.2.13) which gives

$$\hat{\psi}(\mathbf{l}) = -iN_l \int \frac{d^2\mathbf{l}'}{(2\pi)^2}\mathbf{l}\cdot\mathbf{l}' F_1(\mathbf{l}-\mathbf{l}')(\nabla_{\boldsymbol{\theta}} F_2)(\mathbf{l}') \tag{4.2.24}$$

$$= -iN_l\, \mathbf{l} \int d^2\boldsymbol{\theta}\ \exp[-i\mathbf{l}\cdot\boldsymbol{\theta}] F_1(\boldsymbol{\theta})\nabla_{\boldsymbol{\theta}} F_2(\boldsymbol{\theta}) \tag{4.2.25}$$

$$= -N_l \int d^2\boldsymbol{\theta}\ \exp[-i\mathbf{l}\cdot\boldsymbol{\theta}]\nabla_{\boldsymbol{\theta}}[F_1(\boldsymbol{\theta})\nabla_{\boldsymbol{\theta}} F_2(\boldsymbol{\theta})]. \tag{4.2.26}$$

It is important here to note that the quadratic estimator is valid only to the lowest order in the lensing potential.

We now create a lensed CMB map from which we are able to determine the two scalar fields $F_1(\mathbf{l})$

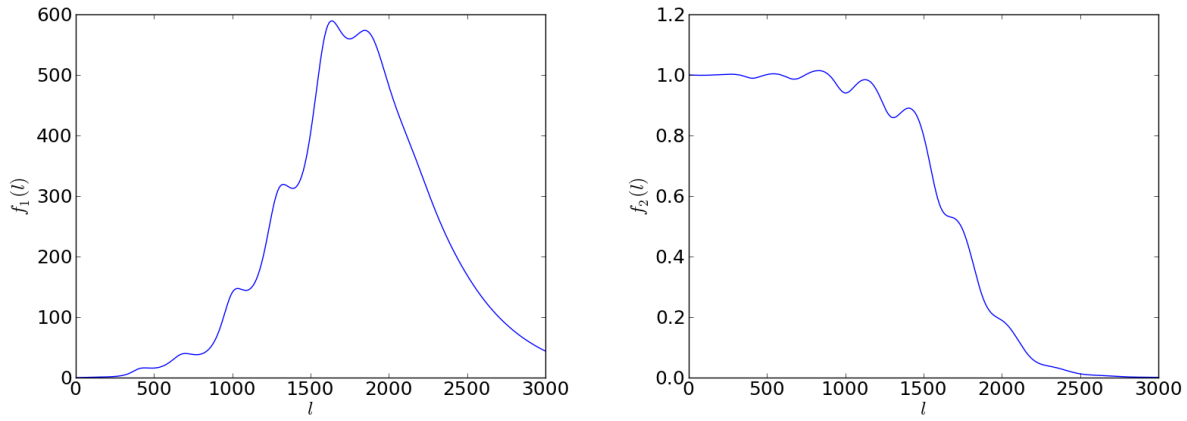

Figure 4.2: **Harmonic space quadratic estimator filters.** The filters used in the implementation of the quadratic estimator. The left panel is $f_1(l) = 1/[\tilde{C}_l + \mathcal{N}_l]$ and the right panel is $f_2(l) = C_l/[\tilde{C}_l + \mathcal{N}_l]$ where C_l, $\tilde{C}_l$ and $\mathcal{N}_l$ are the unlensed, lensed and noise spectra computed by `CAMB` for a WMAP best fit cosmology respectively and $\mathcal{N}_l$ is for the Planck experiment.

and $F_2(\mathbf{l})$. We wish to convolve these two functions to give us a vector field $\mathbf{F}_3(\mathbf{l})$. It is simpler to perform the convolution of these two fields by taking their Fourier transforms, multiplying them in the real space and then Fourier transforming back to harmonic space. Thus, we construct two filters in the real space from $F_1(\mathbf{l})$ and the gradient of $F_2(\mathbf{l})$

$$F_1(\boldsymbol{\theta}) = \int \frac{d^2\mathbf{l}}{(2\pi)^2} F_1(\mathbf{l}) \exp[i\mathbf{l}\cdot\boldsymbol{\theta}] \tag{4.2.27}$$

$$\nabla_{\boldsymbol{\theta}} F_2(\boldsymbol{\theta}) = \int \frac{d^2\mathbf{l}}{(2\pi)^2} i\mathbf{l}\, F_2(\mathbf{l}) \exp[i\mathbf{l}\cdot\boldsymbol{\theta}]. \tag{4.2.28}$$

Multiplying these gives

$$\mathbf{F}_3(\boldsymbol{\theta}) = F_1(\boldsymbol{\theta})\nabla_{\boldsymbol{\theta}} F_2(\boldsymbol{\theta}). \tag{4.2.29}$$

Now, we take the divergence of $\mathbf{F}_3(\boldsymbol{\theta})$, which is more easily done by Fourier transforming to the harmonic space and we define

$$F_4(\mathbf{l}) = i\mathbf{l}\cdot\mathbf{F}_3(\mathbf{l}). \tag{4.2.30}$$

The quantity $F_4(\mathbf{l})$ gives us the quadratic estimator of the gravitational potential up to the total variance N_l

$$\hat{\psi}(\mathbf{l}) = -N_l F_4(\mathbf{l}). \tag{4.2.31}$$

We can then make use of the relations given previously to obtain estimators for the deflection angle and lensing convergence respectively.

4.2.4 Reconstruction of the lensing field with the harmonic space quadratic estimator

In this section we illustrate how the harmonic space quadratic estimator performs in reconstructing the lensing field, showing the size of the bias and how it is reduced as one makes use of additional realizations of the CMB. We perform the estimator on a number of realizations of the lensed CMB where the lensing field has been kept constant in each case. Each realization of the CMB has a different structure, from using different seeds in their construction. By adding the reconstructions from each realization, the Gaussian bias that enters through the uncertainty in the unlensed CMB field can be eliminated and we are left with an unbiased estimator for the lensing field.

In the previous section we showed how the lensing convergence can be reconstructed from the CMB temperature map using the off-diagonal terms of the correlation $\langle \tilde{T}(\mathbf{l})\tilde{T}(\mathbf{l}')\rangle$. We can now apply the estimator that was derived to a simulated lensed CMB temperature map to reconstruct the lensing field using the method detailed in Section 4.2.3. Applying the estimator to a single realization of the CMB results in a noisy reconstruction of the lensing convergence. In principle one could subtract this bias from the reconstructed power spectrum by averaging over many realizations of the large-scale structure. Here, however, we instead perform the lensing reconstruction on an ensemble of 50 lensed CMB temperature maps where the lensing field is kept fixed in each of the realizations. Averaging over the reconstructed maps greatly reduces the variance of the reconstructed lensing field. The recovered convergence is shown in Figure (4.3) for a single realization of the lensed CMB and for 50 realizations of the lensed CMB. The reconstruction of a single realization is very noisy and the correlation between the input and recovered convergence is not entirely obvious. The correlation between the input and recovered convergence improves significantly when the estimator is applied to 50 realizations of the CMB. The contours fit the color-map very well. An additional improvement is noticed in the scale of the color-bars. There

is a significant over-estimation of the lensing convergence when just a single realization of the CMB is used, arising from the additive noise bias discussed in the previous section. By adding the reconstruction from 50 CMB temperature maps, this Gaussian bias is largely eliminated and we obtain values for the convergence more in line with those that are expected. The power spec-

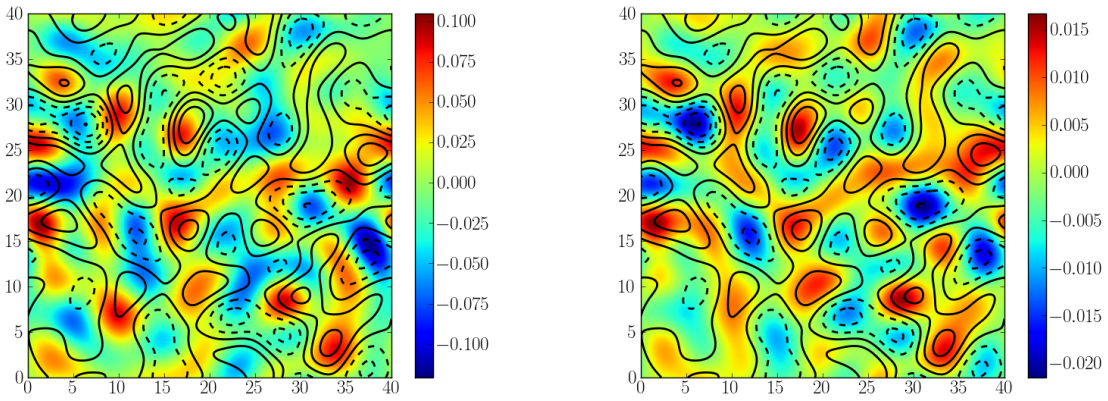

Figure 4.3: **Reconstructed lensing convergence from the harmonic space quadratic estimator.** The reconstructed lensing convergence is shown in the color map for a single realization (left) and 50 realizations (right) of the CMB where the lensing field was kept constant. The contours represent the input convergence field. A band pass filter, blocking all modes outside of $15 < l < 60$, is applied to the maps in order to more clearly show the correlation between the input and recovered convergence. The axes of the maps are in degrees and the color-bars are in units of critical surface mass density. No detector noise was added to the CMB temperature maps.

tra recovered from these maps are shown in Figure (4.4). Power spectra are plotted for 1, 5, 15 and 50 realizations of the CMB. The power spectrum from the map recovered with just a single realization is heavily biased and lies well above the theoretical curve expected for a standard concordance ΛCDM model. As the number of realizations increase, this noise bias is eliminated and the recovered power spectra converges closer to the theoretical curve. There is still a slight over estimation of the power spectrum, possibly due to the $N^{(1)}(l)$ term arising from the cosmic variance in the lensing potential coupled to the unlensed CMB, that was discussed earlier.

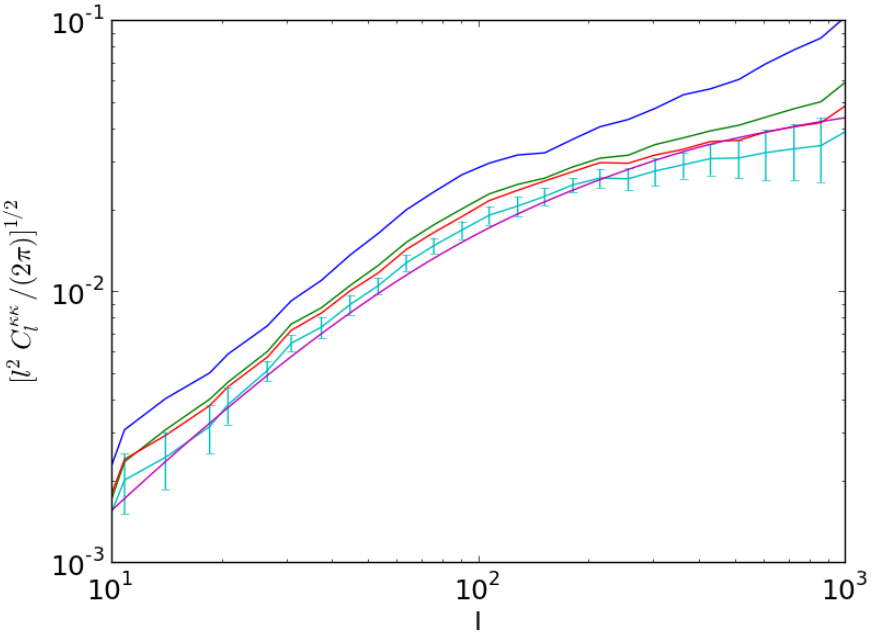

Figure 4.4: **Reconstructed convergence power spectrum for the harmonic space estimator.** The power spectrum of the recovered convergence is plotted for 1 (blue), 5 (green), 15 (red) and 50 (turquoise) realizations of the CMB. The input convergence power spectrum, generated by CAMB for a standard concordance ΛCDM model, is plotted in purple. The error bars are calculated from the variance between reconstructions using 10 realizations of the CMB each.

4.3 Real space estimator for the lensing convergence

We now investigate a real space approach to the lensing reconstruction following the method in [39]. Under the ideal conditions of full sky coverage with no galactic cut and with no bad pixels due to the removal of point sources and uniform sky coverage this approach naturally leads to the same result as that of the approach in harmonic space described previously. Here, however, we consider slightly non-optimal estimators that are modified to have a finite range so that sky cuts, removal of point sources and non-uniform sky coverage may be included easily. These more robust estimators defined in real space may prove to be superior in the analysis of real data [41, 111]. This real space approach has the additional advantage of the convergence and pure shear providing separate lensing reconstructions which may be compared with one another.

The presence of the two shear components allows one to make an estimate for the noise of the reconstruction through the recovered transverse displacement field, which is forbidden in weak lensing.

4.3.1 Derivation of the real space estimator

Consider now the effect of a constant deformation described by the deformation matrix S which relates the angular coordinates $\boldsymbol{\theta}$, which are the the actual coordinates of a point on the CMB, to the coordinates $\boldsymbol{\theta}'$, the coordinates that the same point would have on the unlensed sky. So, in the flat sky approximation and assuming small deviations, we have $\boldsymbol{\theta}' = S\boldsymbol{\theta}$ where $S = \exp[-\kappa]$ so that the temperature field is distorted as

$$\tilde{T}(\boldsymbol{\theta}') = T(\boldsymbol{\theta} = S^{-1}\boldsymbol{\theta}'). \tag{4.3.32}$$

We have previously defined the Fourier transform of the temperature field to be

$$a(\mathbf{l}) = \frac{1}{\sqrt{\mathcal{A}}} \int d^2\theta \exp[i\mathbf{l}\cdot\boldsymbol{\theta}] T(\boldsymbol{\theta}), \tag{4.3.33}$$

where $\mathcal{A}$ is the area of the CMB map. When the lensing transformation S is applied to $a(l)$ we see that

$$\begin{aligned} \tilde{a}(l) &= \frac{1}{\sqrt{\mathcal{A}}} \int d^2\theta' \exp[i\mathbf{l}\cdot\boldsymbol{\theta}'] \tilde{T}(\boldsymbol{\theta}') \\ &= \det{}^{-1/2}[S] a(S^{-1}l), \end{aligned} \tag{4.3.34}$$

where we have made use of the Jacobian to make the change of variable

$$d^2\theta' = \left[\frac{\partial(\theta_1', \theta_2')}{\partial(\theta_1, \theta_2)}\right]^{1/2} d^2\theta. \tag{4.3.35}$$

We are interested here in computing the modified power spectrum $C'(l) = \langle |a'(l)|^2 \rangle$. We see that the power spectrum is given by

$$\tilde{C}(l) = \det{}^{-1}[S] C(S^{-1}l) = \det{}^{-1}[S] C(|S^{-1}l|). \tag{4.3.36}$$

Expanding the deformation $S = \exp[\kappa]$ in its Taylor series and linearizing it such that $S = I + \kappa$ results in a modified power spectrum given by

$$\tilde{C}(l) = C(|l|)(1 - 2\kappa_0) + \frac{l \cdot \boldsymbol{\kappa} \cdot l}{|l|} \left(\frac{dC(l)}{dl} \right). \tag{4.3.37}$$

The convergence tensor, $\boldsymbol{\kappa}$, can be decomposed as a sum of an isotropic (convergence κ) and anisotropic (shear $\gamma_1,\ \gamma_2$) part as

$$\boldsymbol{\kappa} = \begin{pmatrix} \kappa - \gamma_1 & -\gamma_2 \\ -\gamma_2 & \kappa + \gamma_1 \end{pmatrix}. \tag{4.3.38}$$

Thus, to linear order, the power spectrum is modified by this distortion to become

$$C(|\mathbf{l}|) \rightarrow \tilde{C}(l) = C(l) \left[1 + \kappa_0 \left(\frac{d(\ln[C(l)])}{d(\ln[l])} + 2 \right) + \left(\frac{\kappa_+(l_1^2 - l_2^2) + \kappa_\times(2l_1 l_2)}{l^2} \right) \frac{d(\ln[C(l)])}{d(\ln[l])} \right]. \tag{4.3.39}$$

where the homogeneity is preserved but not the isotropy of the underlying statistical process.

We can now construct an estimator for the convergence, κ_0, in an analogous derivation to that used for the harmonic space estimator in the previous section. Taking only the convergence part of Equation (4.3.39) and subtracting the unlensed CMB we have

$$\tilde{C}(l) = \kappa_0 w(l), \tag{4.3.40}$$

where

$$w(l) = C(l) \left(\frac{d(\ln[C(l)])}{d(\ln[l])} + 2 \right). \tag{4.3.41}$$

We can thus construct an estimator for the convergence in a region $\mathcal{A}$ where κ_0 is spatially constant as

$$\hat{\kappa_0} = \frac{1}{N_0} \int \frac{d^2 l}{(2\pi)^2} \tilde{C}(l) W(l), \tag{4.3.42}$$

where

$$N_0^{-1} = w(l) W(l), \tag{4.3.43}$$

so that the estimator is unbiased such that

$$\langle \hat{\kappa} \rangle_T = \kappa_0. \tag{4.3.44}$$

We require that the estimator is of minimum variance and so the weights $W(l)$ become

$$W(l) = \frac{w(l)}{(C(l) + \mathcal{N}_l)^2}. \tag{4.3.45}$$

Thus the minimum variance estimator for the convergence is

$$\hat{\kappa_0} = \frac{1}{N_0} \int \frac{d^2l}{(2\pi)^2} \frac{C(l)}{[C(l) + \mathcal{N}_l]^2} \left[\frac{d(\ln[C(l)])}{d(\ln[l])} + 2 \right] \tilde{C}(l), \tag{4.3.46}$$

and

$$N_0 = \int \frac{d^2l}{(2\pi)^2} \frac{[C(l)]^2}{[C(l) + \mathcal{N}_l]^2} \left(\frac{d(\ln[C(l)])}{d(\ln[l])} + 2 \right)^2. \tag{4.3.47}$$

In terms of the actual lensed temperature map, $\tilde{T}(\boldsymbol{\theta})$, that is observed, the estimator for the convergence can be written as

$$\hat{\kappa}_0 = N_0^{-1} \mathcal{A}^{-1} \int_{\mathcal{A}} d^2\theta \int_{\mathcal{A}} d^2\theta' \, \tilde{T}(\boldsymbol{\theta}) \tilde{T}(\boldsymbol{\theta'}) K_0(\boldsymbol{\theta} - \boldsymbol{\theta'}), \tag{4.3.48}$$

where

$$K_0(\boldsymbol{\theta} - \boldsymbol{\theta'}) = N_0^{-1} \int \frac{d^2l}{(2\pi)^2} \exp[i\mathbf{l} \cdot (\boldsymbol{\theta} - \boldsymbol{\theta'})] \frac{C(l)}{[C(l) + \mathcal{N}_l]^2} \left(\frac{d(\ln[C(l)])}{d(\ln[l])} + 2 \right). \tag{4.3.49}$$

This localized estimation can be translated to different points on the map and we get

$$\hat{\kappa_0}(\boldsymbol{\theta}) = \tilde{T}(\boldsymbol{\theta})(K_0 \circ \tilde{T})(\boldsymbol{\theta}), \tag{4.3.50}$$

where the operator $\circ$ implies a convolution. So we see that the convergence estimator is simply the observed CMB temperature map multiplied by another copy of the temperature map that has been convolved with a kernel $K_0(\boldsymbol{\theta})$. The tail of the filter kernel can be cut off with very little loss in the performance of the estimator as shown in [39]. We can thus truncate the filter so that it has a restricted range and the estimator for the convergence becomes

$$\hat{\kappa}_0(\boldsymbol{\theta}) = \tilde{T}(F_{\kappa_0} T)(\boldsymbol{\theta}), \tag{4.3.51}$$

where F_{κ_0} is the truncated filter. Similar estimators can also be derived for the shear [39]. The noise $\mathcal{N}_l$ acts as a cut off at large l due to the low signal-to-noise ratio of the CMB maps on these small scales.

This estimator in real space will be similarly affected by the uncertainty in the CMB as the harmonic space quadratic estimator. This uncertainty, characterized by the variance of the estimator, given by $N_0(l)$ propagates into a large bias in the estimation of the lensing convergence. This bias is removed in the same way as previously for the harmonic space quadratic estimator.

We have shown that the lensing convergence can be reconstructed by taking a filtered lensed CMB and multiplying it by the lensed CMB field itself. In an ideal experiment with no limits on angular resolution and sensitivity, one could, in principle, reconstruct the lensing field as accurately as desired simply by improving the angular resolution and sensitivity. This of course is not possible in any real experiment and so we need have to ask the question: what is the best shape for such a filter to reconstruct the lensing convergence field? Here we follow the work of [39]. A number of factors must be taken into consideration when trying to determine this shape, the most important of which are the details of the experiment such as the angular resolution and sensitivity and also to a large degree, the cosmological model being used. The purpose of weak lensing experiments is primarily to determine the change in the shape of the power spectrum either over the whole sky e.g., for Planck, or the local power spectrum within a certain finite patch e.g., for ACT, SPT. In CMB lensing the length scales most sensitive to distortions are small and we can justifiably work in the flat-sky approximation.

We proceed by looking at the effect of small deviations where $\boldsymbol{\theta}' = S\boldsymbol{\theta}$ and $S = \exp[-\kappa]$. The resultant transformation to the temperature map under such a convergence is given by the relation

$$T(\boldsymbol{\theta}) \rightarrow T(\boldsymbol{\theta}') = T\left(\exp[-\kappa]\boldsymbol{\theta}\right). \tag{4.3.52}$$

It is useful here to consider the power spectrum in the form $\mathcal{C}(l) = l^2 C(l)$. This power spectrum then transforms as

$$\mathcal{C}(l) \rightarrow \mathcal{C}\left(\exp[+\kappa]l\right). \tag{4.3.53}$$

It is clear to see that for distortions of this type, there is no change in the amplitude of the various features in the power spectrum $\mathcal{C}(l)$, only a slight compression to the left.

The idea here is to minimize the noise in the reconstruction of the lensing convergence. In order to do this, the filter should combine the different wavenumbers weighted inversely to their

variance. The best possible filter one can construct to accomplish this goal would be one which included modes where the gradient of $\mathcal{C}(l)$, which is proportional to $\kappa\mathcal{C}'(l)$, is at an absolute maximum. This should include either a positive or negative phase factor depending on whether $\mathcal{C}(l)$ is rising or falling at that particular wavenumber. It is also necessary to exclude those modes where the power spectrum is nearly flat. Built into the derivation of this filter is the assumption that beyond a certain angular coherence there are no long range correlations and the noise in the reconstructed convergence field may be treated purely as white noise. The filter that is constructed for the real space estimator is shown in Figure (4.5). Clearly, it is also a necessary condition that the area of the experiment $\mathcal{A}$ be large enough that the white noise regime is reached.

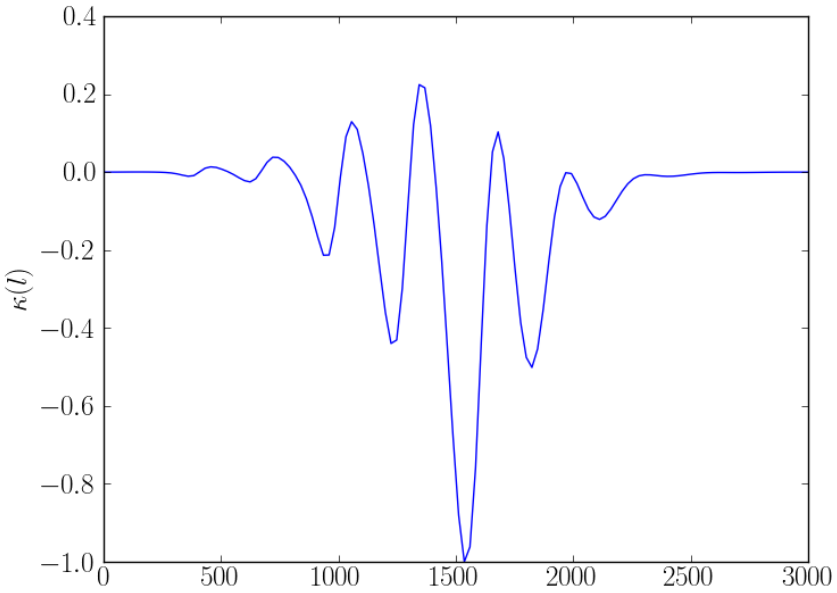

Figure 4.5: **Filter for the real space quadratic estimator.** The profiles of the convergence filter used in the implementation of the real space estimator is shown in the harmonic space.

4.3.2 Multiplicative bias of the real space estimator

We now examine the performance of the real space estimator when it is applied to a CMB temperature map that has been distorted by a lensing field which is modeled as a longitudinal plane wave. This is repeated over a range of wave numbers. The case of distortion by longitudinal plane waves is a useful pedagogical tool to illustrate how, as l increases, a reconstruction of the lensing convergence is biased by a multiplicative factor which reduces the power on smaller scales. This multiplicative bias can be removed from a reconstruction by filtering the maps appropriately. The bias arises as a result of the estimator probing the power spectrum of the convergence field over a finite width window in angular space. As a consequence, the exact underlying lensing field is smoothed out, reducing its amplitude. Once this multiplicative bias is removed, the estimator is no longer of minimum variance resulting in it being more noisy that the harmonic space estimator.

Quantitatively, if the estimator were unbiased we would expect that

$$\langle \hat{\kappa}_0 \rangle = \kappa_0(\boldsymbol{\theta}) \tag{4.3.54}$$

which we observe on very large scales where there is negligible bias. However, a form factor arises for larger wavenumbers and the expectation value of the reconstructed fields has the form

$$\langle \hat{\kappa}_0 \rangle = F(l)\kappa_0. \tag{4.3.55}$$

We illustrate the form of this multiplicative bias by computing the RMS convergence recovered from a lensed CMB map where the lensing field is modeled as a longitudinal wave. A map of the CMB temperature, created in the same manner as previously, is distorted by a lensing field in a similar way as we did for the harmonic space quadratic estimator, with the difference being the form of the lensing field as a longitudinal wave with a particular wavenumber. The real space estimator is first applied to a realization of the unlensed CMB. The RMS convergence calculated κ_{null}, characterizes the bias arising from the uncertainty in the CMB. The real space estimator is then applied to the distorted version of the same realization of the CMB and the RMS convergence κ_{rec} is calculated. We then subtract κ_{null} from κ_{rec} to obtain an unbiased estimate of

the RMS lensing convergence for the wavenumber being examined. This process is repeated over a range of wavenumbers to obtain the shape of the form factor $F(l)$. The form factor computed from simulations is shown in Figure(4.6) and the drop off in power with increasing l is clearly evident. As seen from the plot, the multiplicative bias is clearly an important effect and must be taken into account when attempting to perform a reconstruction of the lensing field using the real space estimator. Fortunately this multiplicative bias is easy to remove from the reconstructed lensing convergence simply by dividing the reconstructed power spectrum by $F(l)$.

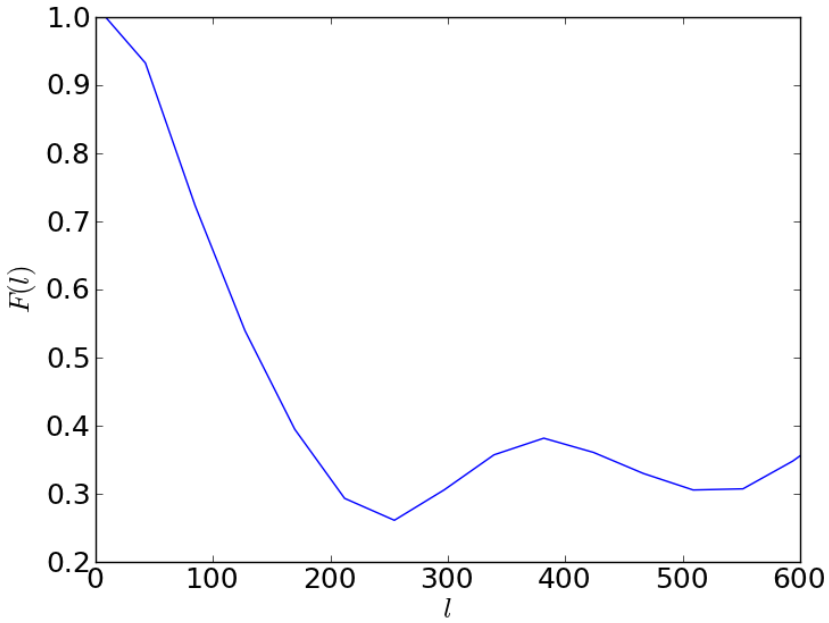

Figure 4.6: **Form factor.** The ratio of the recovered and input RMS convergence is plotted as a function of the multipole l.

4.3.3 Reconstruction of the lensing field with the real space estimator

We are now in a position to apply the real space quadratic estimator to CMB temperature maps that have been lensed by a characteristic lensing field in a standard concordance ΛCDM cosmology. The implementation of the real space estimator is fairly straightforward. We apply the filter in Figure (4.5) to a lensed CMB temperature map. The reconstructed convergence is then simply

this filtered map multiplied directly with the original lensed CMB temperature map. This reconstruction suffers from a similar additive bias to the harmonic space quadratic estimator due to the uncertainty in the primordial CMB and in the large-scale structure that nature has provided. This bias is characterized as the apparent lensing convergence that is reconstructed from an unlensed map and can, in principle be subtracted from our actual reconstructed convergence.

This is not practical however since we do not have access to the unlensed CMB temperature map. Instead, we apply the estimator to an ensemble of lensed CMB temperature maps where the lensing field has been kept fixed but a different seed is used in the generation of the primordial CMB. This dramatically reduces the variance of the estimator and greatly enhances the accuracy of the reconstructed lensing convergence. This is clearly seen in Figure (4.7) where the correlation between the input and lensing convergence recovered from a single realization of the CMB temperature is not apparent visually and can only be weakly detected by statistical methods. In contrast, when the estimator is applied on an ensemble of 100 CMB temperature maps the reconstructed convergence agrees favorably in magnitude with the input convergence. The underperformance of the estimator in the high-l range is as expected from the form factor plot shown in Figure (4.6 and is inherent in only the real space estimator and not the harmonic space estimator.

The reconstructed convergence power spectrum is plotted in Figure (4.8) for a single realization and multiple realizations of the CMB temperature. For a single realization the power spectrum is greatly affected by the variance of the estimator which is a roughly an order of magnitude larger than the expected signal. Over a number of realizations of the CMB temperature map, the variance is greatly reduced and we see a good fit between the input and recovered convergence power spectra. The noise bias is the dominates the reconstructed convergence power spectrum and is roughly an order of magnitude larger than the expected lensing signal. Fortunately, much of this noise, particularly on larger scales is Gaussian and comes from the cosmic variance. A result of this is that we can significantly reduce the noise by reconstructing the convergence over an ensemble of CMB maps, where the lensing field is kept constant. Averaging these maps removes the Gaussian part of the noise and we are left with a strong correlation between the input

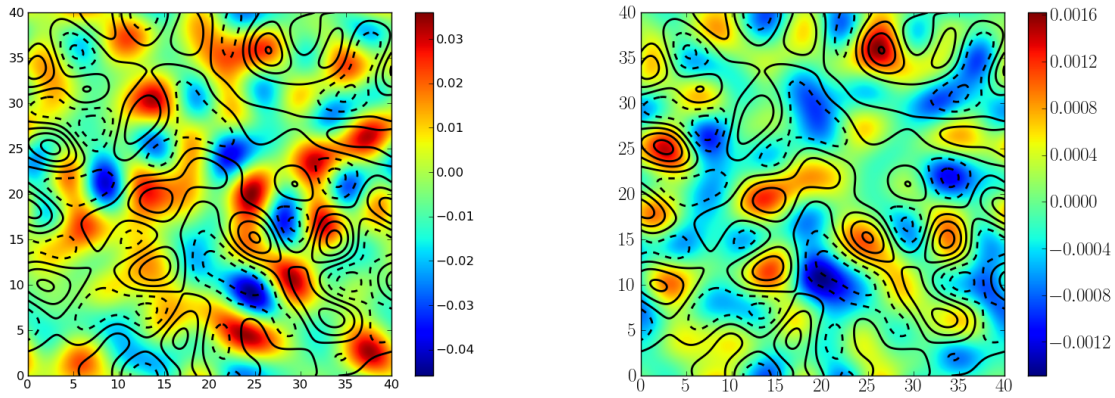

Figure 4.7: **Recovered convergence for the real space estimator.** The reconstructed lensing convergence is shown in the color map for a single realization (left) and 1000 realizations (right) of the CMB where the lensing field was kept constant. The contours represent the input convergence field. A band pass filter, blocking all modes outside of $15 < l < 60$, is applied to the maps in order to more clearly show the correlation between the input and recovered convergence. The axes of the maps are in degrees and the color-bars are in units of critical surface mass density. No detector noise was added to the CMB temperature maps.

and recovered convergence maps.

The fit between the input and recovered power spectra improves as the number of realizations of the CMB is increased. We also note that the form factor, arising from the multiplicative bias discussed in the previous section becomes apparent and manifests itself as a decrease in the convergence recovered from the real space estimator. This is illustrated in Figure (4.9) where the ratio of the recovered and input power spectra i.e. the form factor from the full lensing field is plotted against the form factor calculated from a plane-wave lensing distortion. The same features in the plane-wave form factor are evident in the full-field form factor. The full-field form factor falls off slightly faster than the plane-wave form factor calculated from plane wave distortions. The peaks and troughs are less pronounced in the full-field form factor than in the plane-wave form factor. It appears that large-scale power has been transferred onto smaller scales, smoothing out variations in the recovered power for different multipoles.

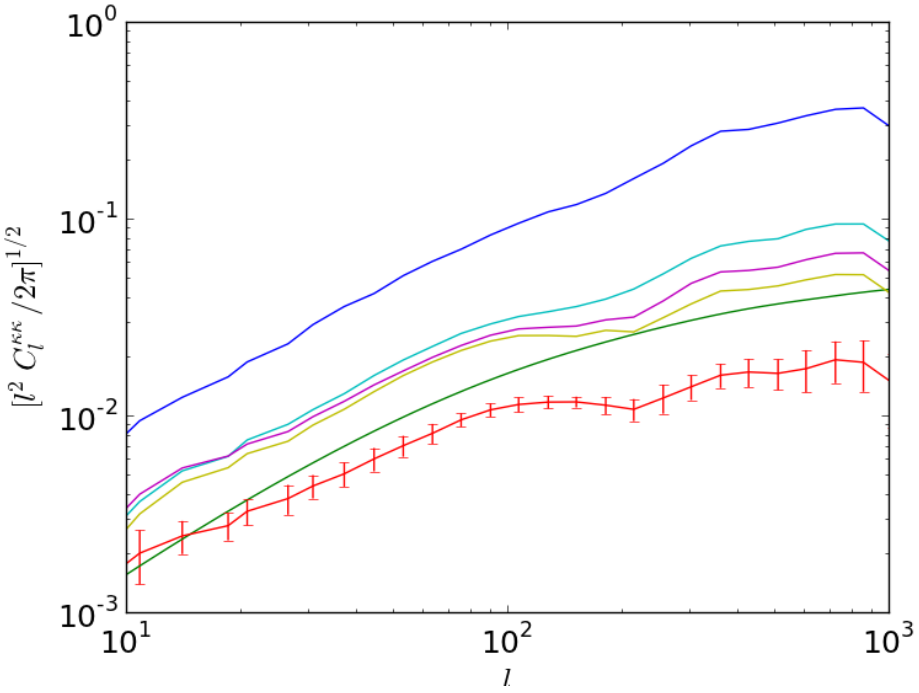

Figure 4.8: **Recovered convergence for the real space estimator.** The power spectrum of the recovered convergence is plotted for 1 (blue), 15 (turquoise), 30 (purple), 50 (gold) and 100 (red) realizations of the CMB. The input convergence power spectrum, generated by `CAMB` for a standard concordance ΛCDM model, is plotted in green. The error bars are calculated from the variance between reconstructions using 100 realizations of the CMB each.

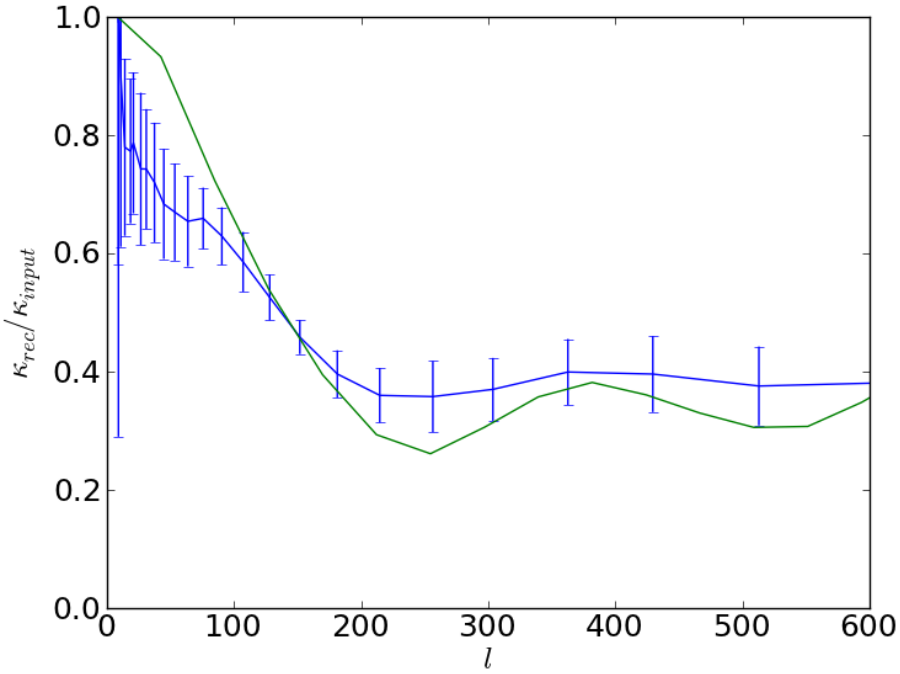

Figure 4.9: **Recovered convergence for the real space estimator.** The ratio of the recovered convergence to input convergence for 100 realizations of the CMB (blue) and the form factor (green) plotted in Figure (4.6). The error bars are calculated from the variance between reconstructions using 100 realizations of the CMB each.

CHAPTER 5

Non-linear Bias of the Convergence Estimators

The amplitude of the lensing convergence is only now beginning to be constrained directly from the CMB from ACT [42] and SPT [43]. It could be the case that the amplitude is large enough that a linear expansion in the deflection angle is not accurate enough to adequately derive estimators to recover the lensing convergence. In the previous section, the estimators used in reconstructing the lensing convergence were valid only to a linear approximation. Ignoring the higher order terms in the estimator introduces a non-linear bias which must be corrected for. Here we examine the effects of a distortion large enough that the first order approximation breaks down. We do this in two parts, first, by looking at simulations where the deflection field is a plane wave and second, by using a realization of the full lensing field expected from `CAMB`. The non-linear bias will affect both the harmonic and real space estimators as they are equivalent at low wavenumbers [39]. We also compare our results to data from the first detections of the lensing convergence from ACT and SPT to estimate if the non-linear correction is important.

5.1 Theoretical considerations

In real space and to linear order, the change in the CMB temperature map caused by lensing is given by

$$\delta T(\boldsymbol{\theta}) = \nabla\psi(\boldsymbol{\theta}) \cdot \nabla T(\boldsymbol{\theta}). \tag{5.1.1}$$

In harmonic space this equates to

$$\delta T(\mathbf{l}) = \int \frac{d^2 l'}{(2\pi)^2} (-\mathbf{l}') \cdot (\mathbf{l} - \mathbf{l}') \psi(\mathbf{l}') T(\mathbf{l} - \mathbf{l}'). \tag{5.1.2}$$

The observed CMB temperature map is $\tilde{T}(\boldsymbol{\theta}) = T(\boldsymbol{\theta}) + \delta T(\boldsymbol{\theta})$ and so we have

$$\begin{aligned} \langle \tilde{T}(\boldsymbol{\theta}) \tilde{T}(\boldsymbol{\theta}') \rangle_T &= \langle (T(\boldsymbol{\theta}) + \delta T(\boldsymbol{\theta}))(T(\boldsymbol{\theta}') + \delta T(\boldsymbol{\theta}')) \rangle_T, \\ &= \langle T(\boldsymbol{\theta}) T(\boldsymbol{\theta}') + T(\boldsymbol{\theta}) \delta T(\boldsymbol{\theta}') + T(\boldsymbol{\theta}') \delta T(\boldsymbol{\theta}) + \delta T(\boldsymbol{\theta}) \delta T(\boldsymbol{\theta}') \rangle_T, \end{aligned} \tag{5.1.3}$$

where the averages are taken over many realizations of the CMB temperature and the lensing field is kept fixed. In most studies of lensing reconstruction, the last term in Equation (5.1.3) is neglected and the two-point correlation function in harmonic space, to linear order in the lensing potential, reduces to

$$\langle \tilde{T}(\mathbf{l}) \tilde{T}(\mathbf{l}') \rangle_T = q(\mathbf{l}, \mathbf{l}') \psi(\mathbf{l} + \mathbf{l}'), \tag{5.1.4}$$

where $q(l, l')$ is given in Equation (4.2.6). This allows us to define the quadratic estimator for the lensing potential given in Equation (4.2.7). In this section, we investigate the effects of a lensing potential high enough in magnitude that the second order terms may not be neglected.

To second-order, the observed CMB temperature is

$$\begin{aligned} \tilde{T}(\boldsymbol{\theta}) &= T(\boldsymbol{\theta} + \nabla\psi(\boldsymbol{\theta})) \\ &= T(\boldsymbol{\theta}) + \nabla\psi(\boldsymbol{\theta}) \cdot \nabla T(\boldsymbol{\theta}) + \frac{1}{2} \left(\nabla\psi(\boldsymbol{\theta})\right)^2 \nabla^2 T(\boldsymbol{\theta}). \end{aligned} \tag{5.1.5}$$

A second-order lensing potential term in the two-point correlation function $\langle \tilde{T}(\boldsymbol{\theta}) \tilde{T}(\boldsymbol{\theta}') \rangle$ arises from multiplication of two first-order terms and from the multiplication of a zeroth- and second-order term. Clearly, the addition of a second-order term to Equation (5.1.4) complicates the issue of deriving an estimator for the lensing potential.

If we include the higher-order terms, we obtain

$$\langle \tilde{T}(\boldsymbol{\theta})\tilde{T}(\boldsymbol{\theta}')\rangle = \boldsymbol{\alpha}(\boldsymbol{\theta}) \cdot T(\boldsymbol{\theta})\nabla T(\boldsymbol{\theta}) + (\boldsymbol{\alpha}(\boldsymbol{\theta}) \cdot \nabla T(\boldsymbol{\theta}))^2 + (\boldsymbol{\alpha}(\boldsymbol{\theta}))^2 \nabla^2 T(\boldsymbol{\theta}), \tag{5.1.6}$$

where $\boldsymbol{\alpha}(\boldsymbol{\theta}) = \nabla\psi(\boldsymbol{\theta})$.

From Equation (5.1.6) we see that the harmonic and real space estimators described in the previous chapter will be inadequate to accurately reconstruct the lensing convergence if the deflection angle becomes significantly large, since they both neglect the last two terms. Neglecting these second order terms will result in the lensing convergence being systematically underestimated when analyzing real data from experiments. We refer to this underestimation as a non-linear bias since is comes about from a violation of the linear approximation. The study which follows has the goal of determining whether this is a significant effect and should this prove to be the case, how one could go about generalizing the estimator to address this bias. In this study, we focus on determining the effect of increasing the magnitude of the lensing field on the reconstructed lensing convergence with the original estimators defined in Chapter 4. Both the real and harmonic space estimators will be similarly affected since they have been shown to be equivalent on large scales [39]. We find that the measured non-linearity is non-negligible which provides the motivation for a follow-up study that formulates an analytical form for a new estimator which includes the second-order lensing potential terms its derivation.

In Section (4.2.2) we discussed an additional source of variance [34] arising from the coupling of the lensing potential to the unlensed CMB. The next step, to follow this work will be to study the effects of including the second-order lensing potential terms in the estimator for the lensing potential on the secondary noise source and whether it can be reduced significantly. This could become important in future experiments since, as discussed earlier, the secondary variance is unaffected by improved sensitivity of the experiment and could provide a limit on the accuracy to which the lensing field can be recovered.

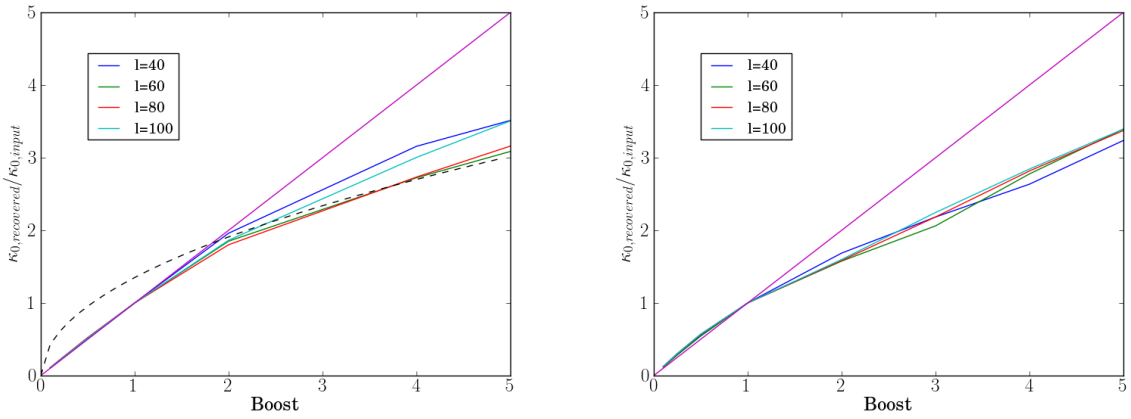

Figure 5.1: **Nonlinear response of estimators for plane wave distortion.** The non-linear response is plotted for the real (left) and harmonic (right) space estimators. The non-linear bias is determined for a range of multipoles up to $l = 100$. The x-axis represents the factor by which the input power spectrum used in the synthesis of the convergence map was multiplied. The y-axis is a ratio between the recovered convergence and the input convergence for the unboosted lensing field. In the plot for the real space estimator the dashed black curve is proportional to the square-root of the boost factor.

5.2 Non-linear bias using a plane wave distortion

The method used to determine the form of the non-linear bias of the estimators is similar to that for the determination of the multiplicative bias of the real space estimator in the previous chapter. In this case however, instead of changing the wavenumber of the plane wave, we consider a single wavenumber in isolation and vary the amplitude of the distortion. We then compute the amplitude of the recovered signal and compare it to the amplitude of the input plane wave, which allows us to determine the loss in power over a range of amplitudes. This is repeated over a range of wavenumbers. This is an extension of the work done in [39], where only the $k = 1$ mode was considered.

The recovered non-linearity from the plane wave lensing distortion approach is shown in Figure (5.1). We see that for the plane wave distortion the real space and harmonic space estimators perform similarly. In the harmonic space estimator however, we observe considerably less variation between different multipoles than with the real space estimator. The variation in the recovered

convergence for different multipoles in the real space estimator results from the multiplicative bias described by the form factor of Section (4.3.2). This is because the form factor recovered where the lensing signal has been boosted is not simply the original, unboosted form factor multiplied by a constant boost factor. It is interesting to note that the drop in the recovered power of the lensing signal as the boost factor increases takes the approximate form of the square-root of the boost factor. It may be the case that an estimator involving quadratic terms in the lensing field, that is derived from a solution of Equation (5.1.6), may be able to significantly reduce this non-linear bias.

5.3 Non-linear bias using the full lensing field

We now turn our attention to the case where the distortion is caused by a lensing field that has a power spectrum of the form expected from CAMB for a standard ΛCDM concordance model but that has been multiplied (boosted) by a constant factor. The approach is similar to that used in the previous chapter in the reconstruction of the lensing convergence but in this case each realization of the unlensed CMB is lensed by a series of lensing fields. All of the lensing fields used have the same underlying random field but the power spectrum used in the synthesis of the maps is multiplied by a range of boost factors which has the effect of either increasing or decreasing the power of the lensing distortion. Fifty realizations of the CMB are used which removes most of the random Gaussian noise which would otherwise dominate the various reconstructions of the lensing convergence. Each of the estimators is then applied to the lensed CMB maps to give a reconstruction of the lensing convergence. From these maps, the power spectra are then calculated and the amplitudes of the recovered power spectra are compared to that of the power spectrum of the input convergence map for a specific multipole.

The drop in the recovered power is plotted as a function of the boost in Figure (5.2). One would not expect there to be much variation between the results of the previous section, where a single plane wave distortion was used to lens the CMB and the results of this analysis, where the full lensing field is used. For the harmonic space estimator however, we notice a slightly larger

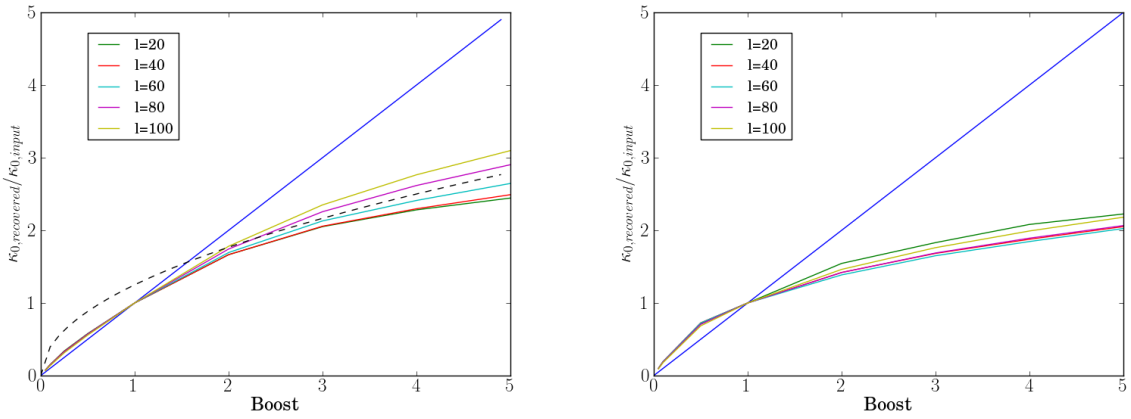

Figure 5.2: **Nonlinear response of estimators for full field distortion.** The non-linear response is plotted for the real (left) and harmonic (right) space estimators. The non-linear bias is determined for a range of multipoles up to $l = 100$. The x-axis represents the factor by which the input power spectrum used in the synthesis of the convergence map was multiplied. The y-axis is a ratio between the recovered convergence and the input convergence for the unboosted lensing field. In the plot for the real space estimator the dashed black curve is proportional to the square-root of the boost factor.

variation between the different multipoles which we did not observe earlier. Also, as l increases, we observe a smaller drop-off in power as the boost increases than in the case of the plane wave distortion. The real space estimator, however, shows more consistency between the plane wave and full-field lensing distortions. Once again, for the full-field, we observe that the loss of power in the lensing convergence becomes smaller as l increases. We return to this point later in the chapter.

We make a comparison between the efficiency of the respective estimators in real and harmonic space. We consider just the $l = 80$ mode to show this comparison and anticipate that the other modes will follow the same relationship. The recovered convergence is shown in Figure (5.3) for both the plane wave and full field analysis of each of the estimators. We see that for small distortions, the two estimators are nearly equivalent but as the distortion increases, the real space estimator becomes more biased. This happens because the harmonic space estimator is not affected by the multiplicative bias that affects the real space estimator.

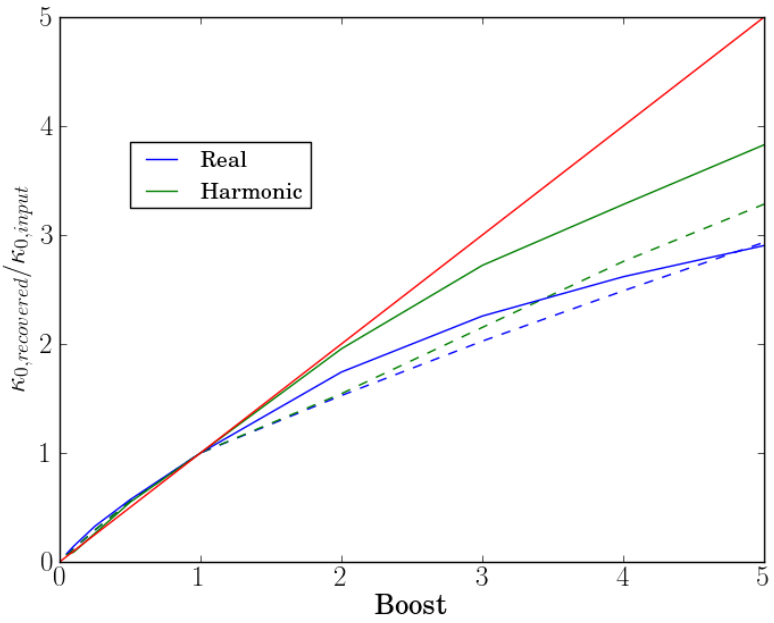

Figure 5.3: **Comparison of estimators.** The non-linear bias of the two estimators are shown for the case where $l = 80$ for both the plane wave and full field analysis. The top two lines are for the harmonic space estimator and the bottom two for the real space estimator. The solid lines and dashed lines represent the full field and plane wave analysis respectively. As expected, the estimators perform similarly in each case. We note that the harmonic space quadratic estimator is noticeably less biased that the real space estimator.

5.4 Comparison with ACT and SPT lensing detections

To conclude this study we compare our results to the data obtained by ACT [42] and SPT [43] in their respective detections of the lensing convergence. From the data we are able to constrain the amplitude of the lensing convergence which will allow us to determine the importance of the non-linear bias. This will determine whether a study of a modified estimator which eliminates the non-linear bias will allow for a significantly more accurate reconstruction of the lensing field. First we examine the lowest multipole, $l = 120$, data point from the ACT detection and this is shown in Figure (5.4). The error bar on the ACT data point is fairly large and is thus consistent with the recovered convergence over a wide range of boost factors. In the absence of the non-linear bias, this data point would rule out a lensing convergence power spectrum boosted by a

factor greater than 1.75 above the fiducial model used in this project. However, from the plot of the recovered convergence as a function of the boost factor, we see that if the non-linearity is not corrected for, the ACT data would fail to rule out models where the power in the lensing field is multiplied by a factor of up to 2.

We also plot the ratio of the recovered convergence for each boost and the input convergence

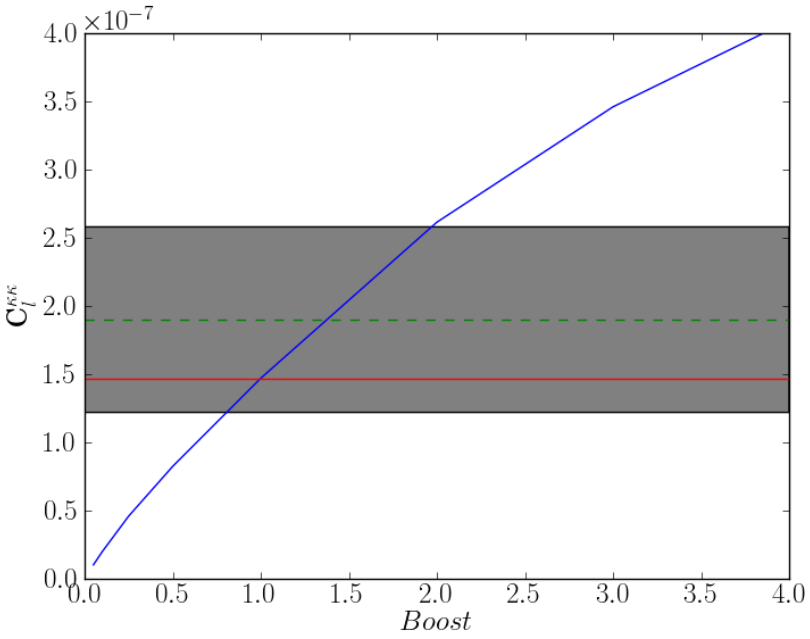

Figure 5.4: **Comparison with the ACT measurement of the convergence at $l = 120$.** The recovered power in the lensing convergence as a function of boost is shown in the blue curve at $l = 120$. The red line is the power expected from the fiducial cosmology. The green dashed line and the grey shaded region are the power and error bar at $l = 120$ from the ACT detection of the lensing convergence. We see that the ACT data is consistent with our simulations up to a boost factor of 2.

for the unboosted case against the data points from the ACT and SPT detections in Figure (5.5). We remove the multiplicative bias by dividing the spectra by the form factor for the unboosted lensing reconstruction. As mentioned earlier, this does not completely flatten the spectra. The SPT data would mostly be consistent with models where the lensing convergence is multiplied by a boost of up to nearly 1.5. The ACT data as mentioned earlier is consistent with models

where the lensing convergence is multiplied by a boost factor of approximately 2. So we see that the allowed boost factors allowed by the observations extend into the region where the harmonic space and real space estimators become somewhat non-linear. This suggests that it will be necessary to develop an improved estimator to address the non-linear bias so that the lensing signal can be more accurately reconstructed and the amplitude of the lensing convergence more tightly constrained. This will form the basis of a future study. However, the higher signal-to-noise measurements by SPT seem to suggest a slightly smaller amplitude for the lensing convergence, in which case the nonlinearity effects discussed here will not be of significant importance.

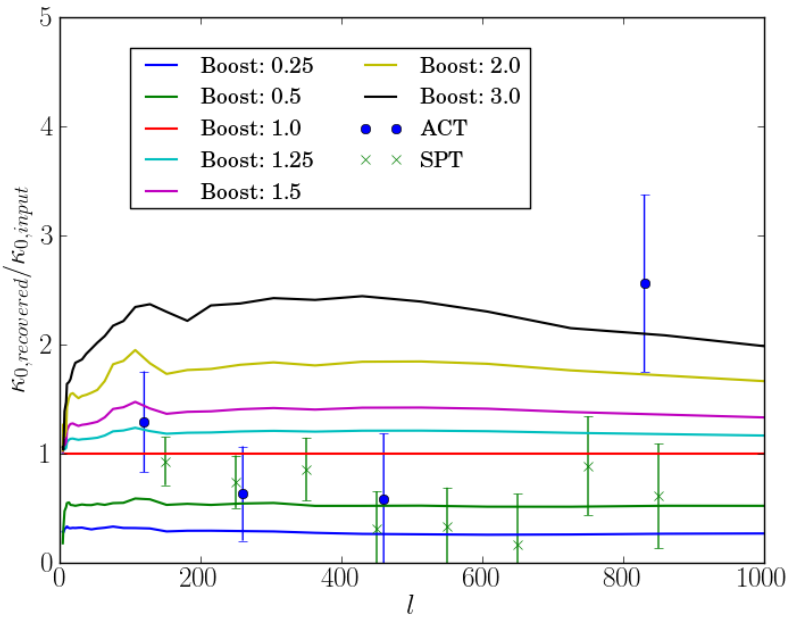

Figure 5.5: **Comparison with ACT and SPT data.** The ACT (circle) and SPT (cross) data points from their respective lensing reconstructions are plotted over the recovered power spectra for a range of boost factors normalized to the unboosted case. The line $\kappa_{0,recovered}/\kappa_{0,input}$ represents the lensing convergence expected from the fiducial cosmology.

CHAPTER 6

Conclusion

One of the most important outstanding problems in cosmology lies in understanding the nature and distribution of dark matter throughout the Universe. Although weak lensing may not provide any information about the nature of dark matter, an accurate reconstruction of the lensing convergence would go a long way to constraining the dark matter distribution. In addition to this, knowledge of the lensing field would, in principle allow for the observed CMB to be delensed and for the first time make the primordial, unlensed CMB accessible to cosmologists. This study has been focused on two estimators for reconstructing the lensing convergence. The first of these estimators is the standard quadratic estimator in harmonic space which has been used by teams from the ACT and SPT collaborations to obtain the first constraints on the lensing convergence power spectrum. The second estimator, while also quadratic, is defined in real space. This estimator has not yet been applied to actual CMB data from experiments.

In Chapter 2, we introduced the standard Big Bang model, describing the origins and evolution of the Universe. The theoretical foundations, namely the Cosmological Principle and Einstein's theory of general relativity were introduced briefly before presenting the details of the observational pillars of the Big Bang model, with a focus on the observed expansion of the Universe and the Cosmic Microwave Background. Big Bang Nucleosynthesis and the formation of structure

from primordial density perturbations were also briefly described.

The focus of third chapter was to introduce the idea of gravitational lensing and develop the theoretical tools needed for this work. We derived an expression for the deflection angle due to weak gravitational lensing by the large-scale structure of the Universe. The lensing potential and effective convergence were defined in terms of the deflection angle and the convergence was related to the power spectrum of the primordial density perturbations. We also discussed how the CMB temperature was affected by weak gravitational lensing and derived an expression for the lensed CMB temperature power spectrum.

As suggested by the title of this thesis, the main purpose of this research has been to investigate methods of reconstructing the lensing convergence from a map of the CMB temperature. The bulk of the research carried out for this project is discussed in Chapter 4. First, we gave details of the synthesis of the CMB temperature and lensing convergence maps that were required for this work. We then presented two estimators, one in harmonic space and the other in real space, for the lensing convergence. Both estimators are significantly biased by uncertainties in the primordial CMB. We found that by stacking and averaging a number of reconstructions, where the unlensed CMB temperature map was varied but the lensing field kept constant, we were able to reduce this bias and accurately reconstruct the lensing convergence map and power spectrum. In the case of the real space estimator we also discussed an additional multiplicative bias arising from the finite width in angular space with which the estimator probes the lensing field.

The estimators described in this thesis are both derived from a linear approximation of the lensed correlation function. In Chapter 5, we discuss the effects of a lensing field with a large enough amplitude that the linear approximation breaks down. We calculate the drop in the recovered convergence as a function of the factor by which the lensing field has been boosted. We compare our results to the data obtained by the ACT and SPT teams in their respective detections of the lensing convergence and find the data points allow for a lensing convergence where the non-linear bias becomes important.

This study has led to the important conclusion that, should the amplitude of the lensing con-

vergence be large enough, the standard quadratic estimators will not be adequate to accurately constrain the lensing signal. We have provided sufficient motivation for a follow up this study which will investigate a new estimator, taking into account the non-linear terms in the deflection angle of the Taylor expansion of the two-point correlation function of the lensed CMB.

Bibliography

[1] Bennett, C. L. et al., ArXiv e-prints (2012).

[2] Hinshaw, G. et al., ArXiv e-prints (2012).

[3] Story, K. T. et al., ArXiv e-prints (2012).

[4] Das, S. et al., ArXiv e-prints (2013).

[5] Larson, D. et al., Astrophys. J. Supp.**192** (2011) 16.

[6] Jarosik, N. et al., Astrophys. J. Supp.**192** (2011) 14.

[7] Guth, A. H., Phys. Rev. D **23** (1981) 347.

[8] Riess, A. G. et al., Astron. J.**116** (1998) 1009.

[9] Perlmutter, S. et al., Astrophys. J.**517** (1999) 565.

[10] Zwicky, F., Helvetica Physica Acta **6** (1933) 110.

[11] Taylor, A. N., Dye, S., Broadhurst, T. J., Benitez, N., and van Kampen, E., Astrophys. J.**501** (1998) 539.

[12] Wu, X.-P., Chiueh, T., Fang, L.-Z., and Xue, Y.-J., Mon. Not. R. Astron. Soc.**301** (1998) 861.

[13] Refregier, A., Annu. Rev. Astron. Astrophys.**41** (2003) 645.

[14] Rubin, V. C., Ford, W. K. J., and . Thonnard, N., Astrophys. J.**238** (1980) 471.

[15] Vikhlinin, A. et al., Astrophys. J.**640** (2006) 691.

[16] Penzias, A. and Wilson, R., The Astrophysical Journal **142** (1965) 419.

[17] Mather, J. et al., The Astrophysical Journal **420** (1994) 439.

[18] Smoot, G. et al., The Astrophysical Journal **396** (1992) L1.

[19] Hincks, A. D. et al., The Astrophysical Journal Supplement Series **191** (2010) 423.

[20] Fowler, J. W. et al., The Astrophysical Journal **722** (2010) 1148.

[21] Lueker, M. et al., Astrophys. J.**719** (2010) 1045.

[22] Planck Collaboration et al., Astron. Astrophys.**536** (2011) A1.

[23] Silk, J., Astrophys. J.**151** (1968) 459.

[24] Sachs, R. and Wolfe, A., Astrophys J **147** (1967) 2007.

[25] Sunyaev, R. A. and Zeldovich, Y. B., Astrophysics and Space Science **7** (1970) 3, 10.1007/BF00653471.

[26] Sunyaev, R. A. and Zeldovich, Y. B., Comments on Astrophysics and Space Physics **4** (1972) 173.

[27] Zeldovich, Y. B. and Sunyaev, R. A., Astrophys. Space Sci.**4** (1969) 301.

[28] Seljak, U., Astrophys. J.**463** (1996) 1.

[29] Zaldarriaga, M. and Seljak, U., Phys. Rev. D **59** (1999) 123507.

[30] Bernardeau, F., Astronomy and Astrophysics **338** (1998) 767.

[31] Lewis, A. and Challinor, A., Physics Reports **429** (2006) 1 .

[32] Zaldarriaga, M., Phys. Rev. D **62** (2000) 063510.

[33] Hu, W., Phys. Rev. D **64** (2001) 083005.

[34] Kesden, M., Cooray, A., and Kamionkowski, M., Phys. Rev. D **67** (2003) 123507.

[35] Hirata, C. M. and Seljak, U., Phys. Rev. D **68** (2003) 083002.

[36] Hu, W. and Okamato, T., Astrophys. J **574** (2002) 566.

[37] Okamoto, T. and Hu, W., Phys. Rev. D **67** (2003) 083002.

[38] Hu, W., The Astrophysical Journal Letters **557** (2001) L79.

[39] Bucher, M., Carvalho, C. S., Moodley, K., and Remazeilles, M., Phys. Rev. D **85** (2012) 043016.

[40] Hirata, C. M., Ho, S., Padmanabhan, N., Seljak, U., and Bahcall, N. A., Phys. Rev. D **78** (2008) 043520.

[41] Smith, K. M., Zahn, O., and Doré, O., Phys. Rev. D **76** (2007) 043510.

[42] Das, S. et al., Phys. Rev. Lett. **107** (2011) 021301.

[43] van Engelen, A. et al., The Astrophysical Journal **756** (2012) 142.

[44] Sherwin, B. D. et al., arXiv:1207.4543v1 (2012).

[45] Bleem, L. E. et al., The Astrophysical Journal Letters **753** (2012) L9.

[46] Einstein, A., Annalen der Physik **49** (1916) 769.

[47] Hubble, E., Proceedings of the National Academy of Science **15** (1929) 168.

[48] Robertson, H. P., Rev. Mod. Phys. **5** (1933) 62.

[49] Friedmann, A., Zeitschrift fur Physik **10** (1922) 377.

[50] Gamow, G., *My World Line: An Informal Autobiography*, Viking Press, 1970.

[51] Friedmann, A., Zeitschrift fur Physik **21** (1924) 326.

[52] Lemaître, G., Annales de la Societe Scietifique de Bruxelles **47** (1927) 49.

[53] Lemaître, G., Annales de la Societe Scietifique de Bruxelles **53** (1933) 51.

[54] Vogt, S. S. et al., HIRES: the high-resolution echelle spectrometer on the Keck 10-m Telescope, in *Society of Photo-Optical Instrumentation Engineers (SPIE) Conference Series*, edited by Crawford, D. L. and Craine, E. R., volume 2198 of *Society of Photo-Optical Instrumentation Engineers (SPIE) Conference Series*, page 362, 1994.

[55] Burles, S. and Tytler, D., Astrophys. J.**499** (1998) 699.

[56] Burles, S. and Tytler, D., Astrophys. J.**507** (1998) 732.

[57] Kirkman, D., Tytler, D., Burles, S., Lubin, D., and OMeara, J. M., The Astrophysical Journal **529** (2000) 655.

[58] de Bernardis, P. et al., First results from the BOOMERanG experiment, in *Cosmology and Particle Physics*, edited by Durrer, R., Garcia-Bellido, J., and Shaposhnikov, M., volume 555 of *American Institute of Physics Conference Series*, pages 85–94, 2001.

[59] MacTavish, C. J. et al., Astrophys. J.**647** (2006) 799.

[60] Abroe, M. E. et al., Mon. Not. R. Astron. Soc.**334** (2002) 11.

[61] Stompor, R. et al., Astrophys. J. Lett.**561** (2001) L7.

[62] Lee, A. T. et al., Astrophys. J. Lett.**561** (2001) L1.

[63] Bennett, C. et al., The Astrophysical Journal Supplement Series **148** (2003) 97.

[64] Mather, J., Fixsen, D., Shafer, R., Mosier, C., and Wilkinson, D., The Astrophysical Journal **512** (1999) 511.

[65] Courteau, S., Willick, J., Strauss, M., Schlegel, D., and Postman, M., The Astrophysical Journal **544** (2000) 636.

[66] Fixsen, D. J. et al., Astrophys. J.**420** (1994) 445.

[67] Komatsu, E. et al., Astrophysical Journal-Supplement Series **148** (2003) 119.

[68] Bartolo, N., Komatsu, E., Matarrese, S., and Riotto, A., Physics Reports **402** (2004) 103.

[69] de Oliveira-Costa, A., Tegmark, M., Zaldarriaga, M., and Hamilton, A., Physical Review D **69** (2004) 063516.

[70] Prunet, S., Uzan, J., Bernardeau, F., and Brunier, T., Physical Review D **71** (2005) 083508.

[71] Knox, L., Physical Review D **52** (1995) 4307.

[72] Seljak, U. and Zaldarriaga, M., Astrophys. J.**469** (1996) 437.

[73] Lewis, A., Challinor, A., and Lasenby, A., Astrophys. J. **538** (2000) 473.

[74] Peebles, P. and Yu, J., The Astrophysical Journal **162** (1970) 815.

[75] Eisenstein, D. et al., The Astrophysical Journal **633** (2005) 560.

[76] Zaldarriaga, M. and Seljak, U., Physical Review D **58** (1998) 023003.

[77] Springel, V. et al., **435** (2005) 629.

[78] Peebles, P., *Principles of Physical Cosmology*, Princeton Univ Pr, 1993.

[79] Newton, I., *Opticks*, Royal Society, London, 1704.

[80] Soldner, J., Berliner Astronomisches Jahrbuch (1801) 161.

[81] Einstein, A., Annalen der Physik **35** (1911) 898.

[82] Einstein, A., Preussische Akademie der Wissenschaften, Sitzungsberichte **part 2** (1915) 831.

[83] Dyson, F. W., Eddington, A. S., and Davidson, C., Royal Society of London Philosophical Transactions Series A **220** (1920) 291.

[84] Eddington, A., *Space, Time and Gravitation: an outline of the General Relativity theory*, Cambridge University Press, Cambridge, United Kingdom, 1920.

[85] Chwolson, ., Am. Nach **221** (1924) 329.

[86] Einstein, A., Science **84** (1936) 506.

[87] Zwicky, F., Physical Review **51** (1937) 290.

[88] Klimov, Y., Soviet Phys. Doklady **8** (1963) 119.

[89] Liebes, S., Phys. Rev. **133** (1964) B835.

[90] Refsdal, S., Mon. Not. R. Astron. Soc.**128** (1964) 295.

[91] Sachs, R., Proceedings of the Royal Society of London. Series A. Mathematical and Physical Sciences **264** (1961) 309.

[92] Zel'dovich, Y. B., Soviet Astronomy **8** (1964) 13.

[93] Schmidt, M., Nature **197** (1963) 1040.

[94] Walsh, D., Carsell, R., and Weymann, R., Nature **279** (1979) 381.

[95] Lynds, R. and Petrosian, V., in *Bulletin of the American Astronomical Society*, volume 18, page 1014, 1986.

[96] Hewitt, J. N. et al., Astrophys. J.**321** (1987) 706.

[97] Hewitt, J. N., Turner, E. L., Schneider, D. P., Burke, B. F., and Langston, G. I., Nature **333** (1988) 537.

[98] Tyson, J. A., Wenk, R. A., and Valdes, F., Astrophys. J. Lett.**349** (1990) L1.

[99] Clowe, D., Gonzalez, A., and Markevitch, M., Astrophys. J.**604** (2004) 596.

[100] Wittman, D. M., Tyson, J. A., Kirkman, D., Dell'Antonio, I., and Bernstein, G., Nature **405** (2000) 143.

[101] Bacon, D. J., Refregier, A. R., and Ellis, R. S., Mon. Not. R. Astron. Soc.**318** (2000) 625.

[102] Van Waerbeke, L. et al., Astron. Astrophys.**358** (2000) 30.

[103] Jauzac, M. et al., arXiv: 1208.4323 (2012).

[104] Bartelmann, M. and Schneider, P., Phys. Rep.**340** (2001) 291.

[105] Hu, W., Phys. Rev. D **62** (2000) 043007.

[106] Seljak, U., Astrophys. J.**463** (1996) 1.

[107] Doran, M., Journal of Cosmology and Astroparticle Physics **2005** (2005) 011.

[108] Zaldarriaga, M. and Seljak, U., Phys. Rev. D **59** (1999) 123507.

[109] Bucher, M. and Moodley, K., Private communication (2010).

[110] Carvalho, C. S. and Moodley, K., Phys. Rev. D **81** (2010) 123010.

[111] Miller, N. J., Shimon, M., and Keating, B. G., Phys. Rev. D **79** (2009) 063008.